Journal of the Atmospheric Sciences

What Forces the Rapid Vertical Acceleration and Vorticity Intensification Near Ground in Tornadoes? Diagnostic Analysis based on a Numerically Simulated Real Tornado

--Manuscript Draft--

Manuscript Number:	JAS-D-25-0033
Full Title:	What Forces the Rapid Vertical Acceleration and Vorticity Intensification Near Ground in Tornadoes? Diagnostic Analysis based on a Numerically Simulated Real Tornado
Article Type:	Article
Corresponding Author:	Ming Xue, Ph.D. University of Oklahoma Norman, OK UNITED STATES
Corresponding Author's Institution:	University of Oklahoma
First Author:	Wei Huang
Order of Authors:	Wei Huang
	Ming Xue, Ph.D.
Abstract:	A numerical simulation of a real-case supercell tornado is analyzed to understand the rapid vertical acceleration of near-surface air parcels leading to intense vertical vorticity stretching and vortex intensification. The vertical acceleration is primarily due to effective buoyancy force and dynamic vertical perturbation pressure gradient force (VPPGF), and the latter is further decomposed into the splat and spin components by solving diagnostic pressure equations. Positive dynamic VPPGF is the dominant forcing responsible for near-ground vertical acceleration, while effective buoyancy is much smaller near ground. In the initial stage of tornado vortex intensification, upward dynamic VPPGF is dominated by the spin term associated with the vorticity of lowering tornado cyclone embedded within a mesocyclone, because maximum vertical vorticity and associated perturbation pressure minimum are located off the ground. After tornadogenesis occurs, the maximum vertical vorticity and corresponding perturbation pressure minimum shift to the ground level, the dynamic VPPGF due to spin becomes negative or downward. At this stage, upward VPPGF associated with the splat term is found to be responsible for promoting and supporting continued upward vertical acceleration and vorticity stretching near the ground. The splat component is largest near the ground and close to the corner region of tornado vortex because of the strong flow deformation there. Trajectory analyses of parcels entering the tornado vortex further substantiate that the dominant term in the upward dynamic VPPGF transitions from the spin term before to the splat term after tornadogenesis. Afterwards, buoyancy becomes the primary force for continued updraft acceleration, usually shortly before reaching the lifting condensation level.

We deeply appreciate the efforts of three reviewers and our point-to-point responses are given below in blue, and quoted texts in the revised paper are given in light blue.

Reviewer #1:

This study analyzes several minutes of a WRF simulation of a tornadic supercell with a maximum spatial resolution of around 50m. The pressure perturbation field is split into the contributions from buoyancy and dynamics and the authors mainly conclude that the dynamic pressure perturbation from spin dominates the vertical acceleration before tornadogenesis while the splat term dominates after a near-ground vortex is established.

Analyzing the evolution of flow acceleration in a tornado is an interesting research project and I compliment the authors on their detailed analysis. The structure of the manuscript is clear and, some grammatical mistakes aside, the text is good to follow. The insightful illustrations help with this.
Furthermore, I agree with the physical reasoning and with the conceptual model resulting from it (Fig. 19). However, I'm not convinced the presented results fully support it. I especially don't agree that the first part of the analysis period is before tornadogenesis (major comment 3). The following comments should be addressed before publication.

Major comments:

1. Lines 63-68: I don't think any of these studies describe step 2 as formation of the low-level mesocyclone but as formation of near-ground rotation (see e.g., Davies-Jones 2015 section 3 "Stage 2 of tornadogenesis: rotation at ground") which then becomes contracted to tornadic intensity in step 3. In your lines 319-320 you yourself consider the incipient tornado separately from the mesocyclone. So I suggest you should be consistent with this in the introduction, meaning that step 2 is not formation of the low-level mesocyclone but near-ground rotation of the pre-tornadic rotation.

Thank you for your suggestion, we have modified the statements about steps 2 and 3 as follows:

“The second step is the formation of near-ground rotation (Davies-Jones 2015). Steps 1 and 2 are necessary, but not sufficient for supercell tornadogenesis (Coffer et al. 2023). The final step for tornadogenesis is the contraction of near-ground rotation into a tornado-strength vortex. The contraction is associated with strong updrafts with intense vertical acceleration

(and strong horizontal convergence) near the surface, which can provide strong stretching to intensify vertical vorticity. Without strong stretching, tornadogenesis will fail even with sufficient vorticity near the ground (Parker 2023). It is commonly believed that the strong near-surface vertical stretching is primarily driven dynamically, by the low-level mesocyclone or the tornado cyclone embedded within, which generates negative dynamic pressure perturbations at the rotation center. This, in turn, establishes a strong upward pressure gradient force (PGF) beneath the strong rotation, promoting vertical acceleration and stretching. Here, a tornado cyclone is defined as a cyclone smaller in size than a mesocyclone but large than a typical tornado funnel (Brooks 1949; Fujita 1958). Tornado cyclone is usually embedded within the mesocyclone circulation (Brown and Wood 1991; Ziegler et al. 2001) and often extends downward above a developing tornado but is not tornado itself.

In the simulation conducted by Coffer and Parker (2015) and Coffer et al. (2017), tornadic supercells with strong mesocyclones have more intense updrafts and are capable to converge and stretch the vortex tube, while the updrafts in non-tornadic supercells are weaker due to disorganized mesocyclone. Roberts and Xue (2017) showed that in their simulation with surface drag applied to the full wind (i.e., not to storm-induced perturbation wind), the intensification and lowering of the mesocyclone toward the ground generates a strong upward PGF leading to tornadogenesis. In contrast, in the simulation with drag applied only to the base-state wind, the mesocyclone only intensifies and lowers modestly and tornadogenesis fails to occur. Flournoy et al. (2020) also found that tornadic cases have stronger low-level mesocyclones to promote stretching and lifting compared to non-tornadic cases. The critical role of low-level mesocyclone in tornadogenesis has also been substantiated in the observational study of Houser et al. (2015), using rapid-scan, polarimetric, Doppler radar observations on a supercell with two tornadoes."

2. Fig. 3 and associated text: I don't see a clear connection between the vertical acceleration and vorticity. The peaks indicated seem fairly random and the 60s delayed is not obvious to me. I suggest objectively testing the correlation of the two timeseries with a lag of 60s.

Thank you for pointing this out. Since the horizontal cross sections shown in Figs. 4, 6, and 7 are drawn at approximately 400 m AGL, the new Fig. 3 now presents the maximum vertical acceleration at 400 m AGL instead of near the

surface. The correlation coefficient between near-surface vertical vorticity and vertical acceleration at 400 m AGL is strongest at a lag of 51 seconds, with a value of 0.945. And we have revised the corresponding statements in Section 3 as follows:

"… The correlation coefficient between the two time series is maximized at 0.945, when the time series of vorticity maximum lags behind that of vertical acceleration by 51 seconds.…

After tornadogenesis, near-surface ζ slightly briefly decreases between 0703:30 and 0704. The decrease in ζ lags behind a sharp decrease in vertical acceleration that begins around 0702:40. After 0705:20, vertical acceleration increases significantly once again, also followed by a notable increase in ζ after 0706."

3. Line 308 and following analysis: It is never formally defined what tornadogenesis success means. Judging from lines 333 and 373, the authors define this when "the maximum zeta is shifted to the surface and the surface vorticity exceeds the vorticity above". However, I don't think this is a generally used criterion for tornadogenesis. This is important because the authors base most of their analysis on comparing periods before and after their stated time of tornadogenesis.
I agree that the near-ground vortex becomes more organized around 0703-0704 but I see some problems with identifying this time as clear tornadogenesis: (1) there is a well-defined column of vertical vorticity and pressure deficit already at 0701 (Figs. 2 and 9), (2) even at the lowest model level the maximum zeta oscillates but is already high at the beginning of the investigated period (Fig. 3), (3) there are similarly intense surface winds throughout the whole period (Fig. 1), (4) the authors interpret a vorticity maximum around 1.5-3 km as the mesocyclone (e.g., lines 321 and 446) but this feature has a maximum intensity of 0.4 /s and the same diameter as the later tornado (~500m) which are almost an order of magnitude larger than the characteristic values of zeta and diameter of a mesocyclone (e.g., Davies-Jones 2015, page 275).
Thus, it seems more fitting that a TLV is already present before the period investigated here and is simply going through typical phases of changing intensity and structure. This interpretation is also consistent with Sun et al. (2019) who show a continuous swath of tornadic winds from 0500-0730 (their Fig. 11f). On page 182 they write: "From 0700 to 0706 UTC these small vortices revolve counter-clockwise around the main tornado vortex…", so there is a main vortex during the period analyzed in the present study.
To reflect this, I think the authors need to rephrase their study that it doesn't analyze periods before and after tornadogenesis but a period of the tornado when the near-ground vortex is disorganized (e.g., before 0703) and becomes

organized again (e.g., after 0704). Alternatively, the authors could redo their analysis at other times of the simulation when the tornado is better defined (e.g., the times in Sun et al. Fig. 8 seem interesting to look at!).

Thanks for pointing out the lack of a clear definition of tornadogensesis in this paper. We have modified our related text to give clear definition. We now have the following text in section 3:

"Very shortly afterward, at 0703:20 (not shown), the maximum ζ shifts to the surface, i.e., the surface vorticity exceeds that aloft and is significantly increased (Fig. 1d and Fig. 2d). At this point, strong vertical vorticity becomes continuous from the ground upward, signifying successful tornadogenesis. Here, our definition of tornadogenesis is consistent with the high-resolution radar studies focusing on tornadogenesis evolution (French et al. 2013; Houser et al. 2015; Bluestein et al. 2019), where a tornado is considered to be successfully formed when the low-level mesocyclone (corresponding to low-level tornado cyclone in our study) intensifies to align with strong near-surface rotation, resulting in a coherent tornado column. Because of the presence of multiple small vortices, some of which exhibit stronger near-surface vorticity than the tornado vortex V0 at some times, we choose to identify tornadogenesis mainly based on the structural changes within the tornado vortex, rather than specific thresholds of surface wind speed and/or vertical vorticity, as done in some simulation studies (e.g., Schenkman et al. 2014; Roberts et al. 2016; Markowski 2024)."

We agree that strong near-surface vertical vorticity is present before 0701 UTC. However, as shown in Fig. 5 of Sun et al. (2019), this vorticity does not form a strongly coherent vertical column. After 0703 UTC, by contrast, strong vertical vorticity becomes continuously aligned from the surface to approximately 2 km, which justifies our focus on the period between 0701 and 0706 UTC to examine tornado intensification and maintenance.

To avoid confusion, we now deliberately differentiate the vortex before and after tornadogenesis. Before tornadogenesis, the vortex is called "tornado vortex" while after tornadogenesis, is called "tornado". We have added definitions in Section 3 as follows:

"Here, by "tornado vortex" refers to a pre-tornadic column of air with relatively large vertical vorticity and a diameter typically ranging from 100 m to 1 km, which ultimately develops into a tornado (Bluestein et al. 2018)"

and

“By 0704, the vorticity isosurfaces associated with the low-level tornado grow upward and is fully connected to the tornado cyclone above (Fig. 2d); the tornado vortex has evolved into a deep column of strong cyclonic rotation that can be called a tornado (or a TLV as in some studies, where the ~50 m horizontal grid spacing is believed to be insufficient to fully resolve the detailed circulation structures of a tornado – in this paper we choose to call it tornado).”

In response to the concern that the magnitude of the “low-level mesocyclone” in our study is larger than the typical values defined by Davies-Jones (2015), we have replaced the term “low-level mesocyclone” with “low-level tornado cyclone”. The term “tornado cyclone” was first introduced by Brooks (1949) and then used by Fujita (1958) to describe a cyclone intermediate in size between a regular cyclone and a tornado funnel. In the studies of Brown and Wood (1991) and Ziegler et al. (2001), the tornado cyclone is more specifically specified as a cyclone embedded within the outer mesocyclonic circulation (Brown and Wood 1991; Ziegler et al. 2001).

We have added this clarification in the Introduction as follows:

“It is commonly believed that the strong near-surface vertical stretching is primarily driven dynamically, by the low-level mesocyclone or the tornado cyclone embedded within, which generates negative dynamic pressure perturbations at the rotation center. This, in turn, establishes a strong upward pressure gradient force (PGF) beneath the strong rotation, promoting vertical acceleration and stretching. Here, a tornado cyclone is defined as a cyclone smaller in size than a mesocyclone but large than a typical tornado funnel (Brooks 1949; Fujita 1958). Tornado cyclone is usually embedded within the mesocyclone circulation (Brown and Wood 1991; Ziegler et al. 2001) and often extends downward above a developing tornado but is not tornado itself.”

The term “mesocyclone” has been revised to “tornado cyclone” throughout the manuscript.

4. Section 6: The parcel analysis is a great addition but I'd like to raise some questions about its robustness.
(1) Only 2 representative trajectories are analyzed and the reader has no way of assessing the uncertainty of them. I suggest showing average parcel information to make your results more robust (as e.g., done by Fischer and Dahl

2020). Footnote 1 says that the parcels accelerations are similar so if this is the case average parcels should be possible although I understand that this might be difficult since the flow is so complex with multiple smaller vortices and spiral motion. However, I think this complexity also makes it necessary to prove that your conclusions hold on average and not just for 2 selected parcels.

Thanks for your suggestion, the average trajectories of the parcels initialized at 0702 and 0703 UTC have been calculated and shown in new Fig. 19 and Fig.20, respectively. We have added the following discussions:

"In addition to the representative trajectories, we also calculate the averages and associated diagnostics of the trajectories initialized at 0702 and 0703 and integrated through 0712 and 0713, respectively (Fig. 19 and Fig. 20). Similar to the representative trajectories (cf. Fig. 17c and Fig. 18c), the dominant term for low-level vertical acceleration (black curves in Fig. 19c and Fig. 20c) and consequently the increase in vertical vorticity (purple curves in Fig. 19a and Fig. 20a), is the dynamic forcing (blue curves in Fig. 19c and Fig. 20c). The dominant term in dynamic forcing in the average trajectories is also similar. For the average trajectory initialized at 0702, in which parcels enter the tornado vortex core before tornadogenesis, the parcels first experience upward DVPPGF due to the spin term prior to 0702:35 (orange curve in Fig. 19c). For the average trajectory initialized at 0703:00, in which most parcels enter the tornado core after tornadogenesis, the DVPPGF due to the spin term is mostly negative (orange curve in Fig. 20c), whereas that due to the splat term is always positive (yellow curve in Fig. 20c). As the parcels reach their respective LCLs, with relative humidity approaching 100% (cyan lines in Fig. 19a and Fig. 20a), the buoyancy forcing becomes persistently positive and contributes significantly to continued ascent (red curves in Fig. 19c and Fig. 20c).

Due to the asymmetry of the surface tornado vortex and the associated spin term (cf. Fig. 6n and o), the timing of the transition of the spin term from negative to positive differs somewhat among the trajectories. For the average trajectory initialized at 0702, the transition occurs at approximately 0702:40 (orange curve in Fig. 19c), which is earlier than the tornadogenesis time of 0703:20. The slightly positive value of the splat term in the average trajectory before 0702:40 (yellow curve in Fig. 19c), in contrast to the negative value in the representative trajectory (yellow curve in Fig. 17c) for parcels initialized at 0702, may also be explained by differences among individual trajectories. For parcels initially located on the east side of tornado, the splat term is already

positive by 0703 (cf. Fig. 6u).

Due to the smoothing effect of the averaging, the magnitudes of the forcing terms are much smaller in the average trajectories (Fig. 19c and Fig. 20c) than in the representative trajectories (Fig. 17c and Fig. 18c). In addition to the smoothing effect, the smaller spin term in the average trajectory initialized at 0702:00 (orange curve in Fig. 19c) compared to the representative trajectory (orange curve in Fig. 17c) may also be partly due to discrepancies between the interpolated and integrated vertical velocities (dashed vs. solid black curves in Fig. 19c). This explanation is supported by the similar magnitudes of the splat term between two average trajectories (yellow curves in Fig. 19 and Fig. 20c). Although using the criterion proposed by Peters et al. (2019) can limit the discrepancies between the interpolated and integrated vertical velocities, it primarily constrains the maximum w along the trajectory to within 10%, and is less effective at controlling errors during the early stages of integration. This limitation is particularly significant near the surface, where the vertical vorticity field is complex, with six small vortices rotating around the tornado vortex (cf. Fig. 1).

In summary, despite some differences between the representative and average trajectories, the key findings are consistent. The dynamic forcing is primarily responsible for rapidly lifting parcels off the ground and enhancing low-level convergence to intensify the tornado vortex and maintain the tornado. The spin term contributes positively to dynamic forcing before tornadogenesis and negatively afterward. The splat term becomes the dominant positive contribution to dynamic forcing after tornadogenesis. As the parcels rise to heights near their LCLs, buoyancy forcing becomes the main driver for continued ascent to upper levels, while the dynamic forcing turns negative."

(2) Furthermore, if I understand correctly, the authors conclude that the vertical acceleration by p'_st is the main driver of the acceleration in the corner region once the tornado is established (at least with two-celled structure). This makes sense, but the parcel B is not showing this as it shows a gradual increase in vertical vorticity and height. Shouldn't there be an abrupt increase if it were representative of the corner region?

From 0703:00 to 0704:30, parcel B has not entered the corner flow region of the tornado and just spirals around the south side of the tornado (Fig. 16b). Therefore, the VPPGF induced by splat is small and the increases in vertical

vorticity and height are both gradual (Fig. 18). When the parcel B enters the tornado, both heights and vertical vorticities increase dramatically between 0704:30 and 0706:00. Parcel B rises from ~60 to ~200 m AGL (Fig. 18c), and vertical vorticity increases from ~0.025 to 0.13 s^{-1} during this period. These details were included in the original manuscript and are reproduced below:

"Specifically, parcel B takes some time to be drawn into the tornado. From 0703:00 to 0704:30, the parcel spirals around the south side of the tornado (see right panels of Fig. 16). In the vertical direction, it rises very slowly and is at ~60 m AGL at 0704:30 (green curve in Fig. 18c). The vertical vorticity also increases only very slightly during the period (Fig. 18a). Between 0704:30 and 0706:00, the parcel rises more rapidly to ~200 m AGL (Fig. 18c), and the vertical vorticity increases from ~0.025 to 0.13 s-1 (Fig. 18a)."

Minor comments:

1. Lines 38-40: Consider removing this sentence

Thank you for this suggestion. Instead of removing this sentence, we rewritten this sentence as follows:

"Trajectory analyses of parcels entering the tornado vortex further substantiate that the dominant term in the upward dynamic VPPGF transitions from the spin term before to the splat term after tornadogenesis."

2. Throughout the intro (e.g., lines 91-97 and 152-155): The introduction jumps between describing the roles of dynamic and buoyancy forcing at different levels of the updraft. I think the fact that buoyancy forcing dominates at mid and upper levels of the supercell is irrelevant for the present study, which only deals with the lowest few km where I think it is established that dynamic forcing dominates. Thus, consider removing content about upper levels to make the focus clear from the start.

We agree that the buoyancy term contributes mainly at upper levels along parcel trajectories. However, the study of Peters et al. (2019) primarily focuses on the **maximum vertical velocity** generated by different forcing terms. And they did not emphasize the heights at which each forcing term dominates along trajectories. We reference their study to underscore the possibility that buoyancy forcing may also play a role in tornadogenesis.

Therefore, in lines 152-155, we proposed that the buoyancy term may

contribute as significantly as dynamic forcing to tornadogenesis. Assessing the relative contributions of dynamic and buoyancy forcing is one of the key questions our study aims to address. For these reasons, we prefer to retain these sentences in the introduction.

3. Line 162-168: I agree but I suggest adding references to support your statement that tornadic zeta decreases with height. One that comes to mind is Davies-Jones (2015) Fig. 6 but a few more would help to show that this is also the case in non-axisymmetric simulations as yours.

Thanks for your suggestion, we have added the references of Davies-Jones (2015), Houser et al. (2015), Bluestein et al. (2019), and Roberts et al. (2020), to support the statement that vertical vorticity in tornadoes generally decreases with height. In particular, Houser et al. (2015) and Bluestein et al. (2019) found that the tornado develops upward based on data from a mobile, polarimetric, rapid scan, X-band, Doppler radar.

4. Furthermore, I agree that this is an interesting research topic. Consider adding "due to spin" after "the largest negative pressure perturbation" because later you show that the pressure gradient can be reversed because of the splat term.

We have added “associated with the spin term” behind “the largest negative pressure perturbation”.

5. Line 209: The lowest model level is at 26m AGL which suggests the vertical resolution near the ground is around 50m? Can the tornado boundary layer and corner flow be resolved with this grid spacing? You could argue that Sun et al. 2019 show detailed evolution of tornado structure to assure the reader. However, please add some discussion in the final section how this limit in resolution might affect the results.

Indeed, the near ground vertical resolution is about 50 m, which is only marginal in resolving corner flows. We have added the following at the end of section 2a:

“We note here that the horizontal and vertical grid spacings are both about 50 m near the ground, which may be considered only marginal in resolving the corner flow structure within developed a tornado. The tornado simulated may be more appropriately called a TLV, but for simplicity we will call it tornado in this paper.”

In response to “add some discussion in the final section how this limit in resolution might affect the results”, we have added some discussion in the final section as follows:

“According to Bluestein et al. (2014), a vertical resolution of approximately 1–1.5 meters in the corner region of a tornado is likely sufficient to resolve vertical variations in the wind. In our study, ~ 50 m horizontal and vertical grid spacings near ground cannot fully resolve the structure of corner flow, which may quantitatively affect the results of diagnosed p'_{st} distribution. However, given that the simulation does capture convergent low-level flows that abruptly turn upward to form strong updraft cores around central downdraft at the two-cell stage of the tornado (see Fig.8 in Sun 2019), we believe our results are at least qualitatively correct or reasonable.”

6. Line 303: Perhaps I missed something but why are the grids different? Aren't WRF grids also terrain-following?

We have added interpretation at the end of the Section 2b as follows:

“The horizontal grid and vertical model levels are defined to be effectively the same between WRF and ARPS, although WRF employs a hydrostatic pressure-based vertical coordinate while ARPS uses a flexible height-based vertical coordinate. The heights of the ARPS model levels are derived from the geopotential heights of the hydrostatic-pressure-based WRF model levels. Therefore, the grid conversion mainly involves conversions among selected WRF and ARPS state variables.”

7. Fig. 12: You are not discussing the x and y components in the text so I suggest using the same colorscale as for the z component to make you point clearer that it is much larger.

We try to use the same color scales for x, y, and z components of vorticities. However, the magnitudes of p'_{sn} associated with the horizontal vorticity is much smaller than that of vertical vorticity. The minimum of p'_{sn} associated with the horizontal vorticities is ~300 Pa, while the p'_{sn} associated with the vertical vorticity is ~2100 Pa. Therefore, if the p'_{sn} associated with horizontal vorticities is also colored from -2100 to -300 Pa, the details of the p'_{sn} will not be clear, so we still keep the original color scale here. While we add a description of the magnitudes of the horizontal vorticities, as following:

"At both times, the dominant component of p'_{sn} is associated with vertical vorticity (the third column of Fig. 12). This result is reasonable, as the magnitude of horizontal vorticity (~10^{-2} s^{-1}) is much smaller than that of vertical vorticity (~10^{-1} s^{-1}) from 0701 to 0706 (figures not shown)."

8. Lines 702-705: Can you elaborate or provide references why you think the increasing centrifugal force is the main cause slowing the radial inflow? My interpretation would be that this is mainly controlled by tornado structure with the central downdraft in a two-celled vortex leading to the corner region being pushed outward.

Thanks for your suggestion. We have added detailed interpretations as follows:

"As suggested earlier, the strong convergence/divergence occurs because, as the swirling air parcel flows towards the tornado center, it will be halted at certain radius r from the tornado center, since the radial wind must vanish at r = 0 and the tangential velocity will reach infinity due to the angular momentum conservation at r = 0. At the later two-cell stage of the tornado, the central downdraft also acts to prevent the near-surface radial inflow from reaching excessively small radii. Therefore, due to mass continuity as well as the increase in centrifugal force, the swirling air rushing in from all directions must abruptly slows down, turn, and flow upward (Bluestein 2013). Therefore, the radial convergence is largest at the periphery of the tornado core, especially at the west and north edges"

9. Line 1058: Can you add a reference for why updraft should be near the maximum tangential velocity? Aren't one-celled vortices defined by their vertical jet near the central axis (e.g., Lewellen 1993, Bryan at al. 2017)? Or is this what you mean because u_tan is maximized near the center?
Lewellen, W. S. (1993). Tornado Vortex Theory. The Tornado: Its Structure, Dynamics, Prediction, and Hazards, 79, 19-39.
Bryan, G. H., Dahl, N. A., Nolan, D. S., & Rotunno, R. (2017). An eddy injection method for large-eddy simulations of Tornado-like vortices. Mon. Wea. Rev., 145(5), 1937-1961

Thank you for pointing this out, we agree that the radius of strongest updraft does not coincide with that of the maximum tangential wind in a one-cell tornado. In an axisymmetric one-cell tornado structure, the strongest updraft is located at the tornado center, whereas the radius of maximum tangential velocity lies slightly farther from the tornado center (see Fig. 10 in Rotunno

2013). This sentence has been revised accordingly:

“When the tornado has a one-cell structure, the strongest near-surface updraft is usually near the tornado center (Rotunno 2013), but when the tornado has a two-cell structure, the downdraft is found at the center of vortex that may or may not reach the ground surface while updraft is usually found near the radius of maximum vorticity or vorticity ring, somewhat like the eye wall of tropical cyclones (Huang and Xue 2023).”

Typos:

1. Line 209: "AGL" is not defined anywhere I think.

“Above the ground level” has added before “AGL”

2. Line 243: Missing "the" before "Poisson" (similar missing "the" or "a" in lines 200, 456, 999, 1006, twice in 1040, 1112, 1115; I recommend checking the whole text again for this)

Thank you for your suggestion. We have checked the whole text and added “the/a” in corresponding places.

3. Line 346-349: Sentence structure seems broken in the end of the sentence. Please check.

The sentence has rewritten as “This suggests that the rapid vertical acceleration at the tornado vortex location, along with the accompanying strong near-surface convergence into the tornado vortex, is critical for vortex merger and subsequent intensification via vertical stretching.”

4. Line 502: "effort"
Line 553: "extend"
Line 648: "show"

We have corrected the above typos.

Reviewer #2:

We deeply appreciate the efforts of this reviewer and our point-to-point responses are given below in blue, and quoted texts in the revised paper are given in light blue.

Major comments:

1. Lines 319 and following: The description of the low-level mesocyclone and surface vortex being "disconnected" is somewhat unclear and could be misinterpreted. This may be true of the chosen vorticity isosurface in Fig. 2 (even there, the lowest 0.15 s-1 isosurface does appear to connect the two maxima at 0701), but it seems likely there is a continuous column of large vertical vorticity below that contour value, and as is shown later, the upper maximum has a strong dynamical influence on the lower. Maybe this could be reworded in terms of two local maxima existing at different altitudes?

We have revised Fig.2 to make the disconnected between the low-level mesocyclone and surface vortex clearer in terms of 0.15 s^{-1} vertical vorticity, especially at 0702 UTC.

We have changed the sentence to "At 0701, the low-level tornado cyclone and the surface vortex V0 appear disconnected when rendered using vorticity isosurfaces above 0.15 s^{-1}; at least there are two local maxima existing at different altitudes". The ensuing sentences describing the three-dimensional vertical vorticity structures have also been modified.

2. Fig. 2: What is the vertical scale of the region shown?

Thank you for this suggestion, we have added the vertical scales in the new Fig.2.

3. 631–632: Should this be reversed? The PGFs would have these directions, but the gradients themselves would be upward for p'sn and downward for p'st?

Thank you for pointing out this mistake, we have modified the related sentences as following:

"Note that the vertical gradient of p' and PGF are opposite in sign. The downward vertical gradient of p'_{st} is comparable to the upward vertical gradient of p'_{sn}, particularly on the northwest side of the tornado vortex (Fig. 10d and Fig. 11 d), creating net downward vertical gradient of p' and upward

dynamic PGF there (c.f., Fig. 6d). While p'_{sn} and p'_{st} are slightly weakened from 0705, the minimum p'_{sn} (Fig. 10e–f) and maximum p'_{st} (Fig. 11e–f) remain at the surface. Consequently, the PGF associated with p'_{sn} and p'_{st} remain downward and upward, respectively."

4. Section 6: Given that trajectories are initialized right at the lowest scalar level of 26 m, do any spend time below that lowest level (e.g., Vande Guchte and Dahl 2018)? If so, how are these handled?

In the trajectory calculation using ARPS, if a parcel's height falls below the lowest model level, it is set to a height corresponding to the lowest model level plus 10% of the smallest vertical grid spacing. Although Vande Guchte and Dahl (2018) suggest that the best way to avoid unphysical tendencies in scalar variables along trajectories, particularly when parcels fall below the lowest scalar model level, is to remove such parcels from analyses when using free-slip boundary conditions, the discrepancies between interpolated and integrated vertical velocities along the representative (Fig. 17 and Fig. 18) and the average trajectories (Fig.19 and Fig. 20) are relatively small. Also, we have applied a much more stringent screening procedure that select and keep only 'accurate' trajectories, as described in paragraph 3 of section 6, which has screened a large number of trajectories calculated. This likely have also removed inaccurate trajectories that follow below the lowest model level above ground.

5. Section 6: Compared to the detailed interpretation of the dynamic terms at several key times, relatively little is said about the role of effective buoyancy, even though it dominates the DVPPGF in certain parts of the trajectories shown. Would it be possible to offer a little more physical description, and/or refer the reader to any other works highlighting the role of effective buoyancy at low levels in tornadoes?

Thank you for this comment. The discussions about the role of effective buoyancy were already included in the original manuscript. In section 6, we noted that as the parcels rise to heights near their LCLs, buoyancy forcing becomes the main driver for continued ascent to upper levels, while the dynamic forcing turns negative. Additionally, in the summary and discussions, we emphasized the contribution of effective buoyancy as follows:

"The buoyancy forcing is weakly negative during low-level lifting in the current case. However, buoyancy becomes the dominant positive term once parcels

shortly before reaching their LCLs, facilitating further acceleration and rising of the parcels to higher altitudes, joining the storm updrafts. At this stage, dynamic forcing often becomes negative. The persistent positive buoyancy acting on the rising parcels allows for substantial accumulated vertical momentum and for typical supercell storms, thermal buoyancy is still the primary driving force for the storm updraft. Without it, a strong mesocyclone cannot form. In a real-case simulation, Yokota et al. (2018) also found that non-linear dynamic forcing is important at lower levels, then buoyancy forcing becomes critical before reaching LCL. Wade and Parker (2021) similarly identified a change in the dominant term from dynamic forcing to buoyancy forcing, but they found the occurrence of this transition at the level of mid-level mesocyclone rather than earlier at the LCL. This difference may arise from their simulations being conducted in a high-shear, low-CAPE environment, while our case has significant CAPE."

To respond to the comment that "refer the reader to any other works highlighting the role of effective buoyancy at low levels in tornadoes", actually, we have referred the importance of effective buoyancy in low-levels done by Dawson et al. (2016) in Introduction. The sentenced are reproduced here:

"Another aspect of the dynamic perturbation pressure is its effect on the air parcel density therefore buoyancy; larger negative perturbation pressure within tornadoes corresponds to lower air density and larger positive buoyancy that can help enhance updraft within tornadoes. This effect is found in a simulated tornado-like-vortex (TLV), where negative perturbation pressure is significant (Dawson et al. 2016)."

Minor comments:

1. 93–97: Suggest clarifying the altitudes at which buoyant accelerations are found to dominate dynamic ones.

Although Peters et al. (2019) show the composite vertical profiles of buoyancy and vertical pressure gradient force induced by buoyancy and dynamic in their supercell simulations (see Fig. 6), they do not specify the altitude at which buoyancy forcing (i.e., the sum of buoyancy and the vertical pressure gradient force induced by buoyancy) begins to dominate over dynamic forcing. In their study, their focus is mainly on the **maximum** vertical velocity induced by the

forcing terms rather than the trends of forcing terms along the trajectories. Therefore, we have chosen not to specify the altitude in our discussion.

2. 598: Should p'sa here be p'st?

Yes, "p'_{sa}" has replaced by "p'_{st}".

3. 674: What about the comparable magnitude for y vorticity in Fig. 12b? Some mention or interpretation of that might be helpful here.

The magnitudes of both the x- and y-component vorticities are on the order of 10^{-2} s^{-1}. We have added this information regarding the horizontal vorticity magnitudes as follows:

"This result is reasonable, as the magnitude of horizontal vorticity (~10^{-2} s^{-1}) is much smaller than that of vertical vorticity (~10^{-1} s^{-1}) from 0701 to 0706 (figures not shown)."

4. A couple of the 3D figures lack horizontal scales, which are less important than the vertical scale for Fig. 2, but would still be nice to have.

Adding horizontal scale bars within the figures would introduce visual clutter and potentially obscure the isosurfaces. Therefore, we have included the horizontal extents in the captions of Figs. 2, 9, 10, and 11.

Reviewer #3:

The authors present a comprehensive analysis of the perturbation pressure field evolution associated with a simulated tornadic vortex during tornadogenesis. The goal of the study is to better understanding the low-level forcing that leads to tornadogenesis and early tornado maintenance, especially the role of the deformation field (the 'splat' term in the perturbation pressure equation) which has been largely overlooked in past studies. The results indicate that the low-level deformation field is key for providing an upward directed perturbation pressure gradient force as the low-level rotation increases in the tornado, and these results will be of interest to the severe storms scientific community.

However, there are several issues which I feel need to addressed before the paper can be accepted for publication. There are also many grammatical errors throughout the text, and instances where the clarity of either the writing or the figures could be improved (see minor comments).

We deeply appreciate the efforts of this reviewer and our point-to-point responses are given below in blue, and quoted texts in the revised paper are given in light blue.

Major Comments:

1. A key part of the tornadogenesis process according to the manuscript is the lowering of the mesocyclone toward the surface with time. However, the authors never define what constitutes the 'mesocyclone' in their analysis, and the vertical vorticity values associated with the simulated mesocyclone shown in the figures are quite large (0.2-0.3 s-1). Given the large vertical vorticity values and the fact that horizontal scale of the mesocyclone shown is similar to the scale of the tornado, one could interpret this as a TVS-like feature embedded in the broader mesocyclone. This implies there could already be an incipient tornadic vortex embedded within the mesocyclone prior to surface tornado development, which might be affecting the tornadogenesis process. It's not clear that the surface vortex V0 is completely separate from this mesocyclone feature based on what is shown in Figure 2. Could the authors comment on this? It would be very helpful if the authors define what they mean by 'mesocyclone' in the context of this study. Likewise, it would also be helpful to define what constitutes a 'tornado vortex' and 'tornado' in the simulation, as the latter is usually defined by a wind speed threshold, yet no winds are shown or speed values provided in the text.

This is a very valid comment, and reviewer 1 has raised a similar concern in the major comment 3. Indeed, the vorticity in the so-called low-level mesocyclone is too large for a typical mesocyclone, while the diameter of the

vortex is too small to be considered mesoscale – its dimension are closer to those of tornadoes than mesocyclones. We have therefore replaced all such references to “low-level mesocyclone” with “tornado cyclone” and have added a definition of “tornado cyclone” based on previous studies.

We now have the following in the first paragraph of Introduction:

“It is commonly believed that the strong near-surface vertical stretching is primarily driven dynamically, by the low-level mesocyclone or the tornado cyclone embedded within, which generates negative dynamic pressure perturbations at the rotation center. This, in turn, establishes a strong upward pressure gradient force (PGF) beneath the strong rotation, promoting vertical acceleration and stretching. Here, a tornado cyclone is defined as a cyclone smaller in size than a mesocyclone but large than a typical tornado funnel (Brooks 1949; Fujita 1958). Tornado cyclone is usually embedded within the mesocyclone circulation (Brown and Wood 1991; Ziegler et al. 2001) and often extends downward above a developing tornado but is not tornado itself.”

The term “mesocyclone” has been revised to “tornado cyclone” throughout the manuscript.

Tornadogenesis is also more clearly defined in the following revised text:

“Very shortly afterward, at 0703:20 (not shown), the maximum ζ shifts to the surface, i.e., the surface vorticity exceeds that aloft and is significantly increased (Fig. 1d and Fig. 2d). At this point, strong vertical vorticity becomes continuous from the ground upward, signifying successful tornadogenesis. Here, our definition of tornadogenesis is consistent with the high-resolution radar studies focusing on tornadogenesis evolution (French et al. 2013; Houser et al. 2015; Bluestein et al. 2019), where a tornado is considered to be successfully formed when the low-level mesocyclone (corresponding to low-level tornado cyclone in our study) intensifies to align with strong near-surface rotation, resulting in a coherent tornado column. Because of the presence of multiple small vortices, some of which exhibit stronger near-surface vorticity than the tornado vortex V0 at some times, we choose to identify tornadogenesis mainly based on the structural changes within the tornado vortex, rather than specific thresholds of surface wind speed and/or vertical vorticity, as done in some simulation studies (e.g., Schenkman et al. 2014; Roberts et al. 2016; Markowski 2024).”

“Tornado vortex” and “tornado” are also clearly defined:

“Here, by “tornado vortex” refers to a pre-tornadic column of air with relatively large vertical vorticity and a diameter typically ranging from 100 m to 1 km, which ultimately develops into a tornado (Bluestein et al. 2018)”

and

“By 0704, the vorticity isosurfaces associated with the low-level tornado grow upward and is fully connected to the tornado cyclone above (Fig. 2d); the tornado vortex has evolved into a deep column of strong cyclonic rotation that can be called a tornado (or a TLV as in some studies, where the ~50 m horizontal grid spacing is believed to be insufficient to fully resolve the detailed circulation structures of a tornado – in this paper we choose to call it tornado).”

While for the comment that “it is not clear that the surface vortex V0 is completely separate from this mesocyclone feature based on what is shown in Figure 2”, we agree that the tornado cyclone and pretornadic vortex V0 are not completely separated, the disconnection we mentioned here is in terms of two local maxima at different altitudes. We here want to express that the low-level tornado cyclone, ~1 km, is relatively weak compared to that near the surface and aloft. We have modified the discussions in Section 3 as follows:

“The near-surface vortex V0 now exhibits an oval-shaped “single cell” structure where the maximum ζ is located at the center of vortex (Fig. 1b). The contraction of V0 is clearly related to the strong near surface convergence and the associated vertical stretching at its center, but it remains disconnected from the tornado cyclone aloft when viewed using the 0.15 s^{-1} ζ isosurface (Fig. 2b). This disconnection indicates the presence of a weaker low-level tornado cyclone around 1 km. The characteristic that the low-level tornado cyclone appears weaker than the vortex above and below just before and during tornadogenesis is similar to the vertical structure of the tornado vortex signature (TVS) based on high-resolution radar data (French et al. 2013; Houser et al. 2015; Bluestein et al. 2019).”

2. In 'real world' heterogenous simulations, models often use a reference state defined at the start of the simulation far from the region of interest as the 'base

state' from which buoyancy (B) is calculated. This can sometimes result in a misleading interpretation of the local buoyancy tendencies. Are the buoyancy tendencies shown calculated from a base state that is representative of the storm environment? The results shown indicate that the effective buoyancy is often positive below cloud base and is always positive above the LCL (not the LFC - are they the same?). Given that the effective buoyancy (of which B is a part) is playing an important role in the analysis presented, it's important for the reader to understand how B is calculated in the simulation, and it would be helpful if the authors could elaborate on these issues in the manuscript.

We agree that using a reference state defined at the start of the simulation far from the region of interest in calculating the buoyancy (B), can lead to a misleading interpretation of local buoyancy tendencies. For this reason, we calculate **effective buoyancy (EB)**, defined as the sum of the buoyancy term B and the vertical perturbation pressure gradient force induced by buoyancy, $\frac{1}{\rho}\frac{\partial p'}{\partial z}$, rather than one calculated based on deviation from the remote environment, following Davies-Jones (2003) and Doswell and Markowski (2004).

As discussed by Davies-Jones (2003) and Doswell and Markowski (2004), both the BVPPGF and the buoyancy-induced pressure gradient force (BVPPGF) depend on the choice of base state. However, their sum, EB, depends only on horizontal density variations. Therefore, the choice of base state in our study has limited impact on our results. We have clarified this in the original manuscript (Section 2b), and the relevant texts are reproduced below:

"Within the effective buoyancy term, the contribution of BVPPGF generally opposes that of B, thus considering only B can lead to an overestimation of buoyancy (Houze 2014; Jeevanjee and Romps 2016). Additionally, both BVPPGF and buoyancy depend on the choice of base state, while EB only depends on horizontal variations in the density field, as discussed by Davies-Jones (2003) and Doswell and Markowski (2004). Therefore, using EB to assess the contribution of buoyancy is more appropriate."

Regarding the reviewer's question about the LCL and LFC levels, according to the introduction of mesoscale analysis parameters

(https://www.weather.gov/source/zhu/ZHU_Training_Page/convective_parameters/Sounding_Stuff/MesoscaleParameters.html), the LFC-LCL difference is similar to CIN (convective inhibition). The smaller the difference between the LFC and the LCL, the more likely deep convection becomes.

In our study, the LCL (lifting condensation level) is typically close to the level where **effective buoyancy** becomes positive. While the LFC (level of free convection) is the level where the parcel becomes positively buoyant, meaning that **the buoyancy term B alone** becomes positive above that height. As a result, the lowest level of positive effective buoyancy can be lower than the LFC, provided that the pressure gradient force induced by buoyancy is sufficiently positive to offset negative buoyancy. In our case, since the perturbation pressure induced by buoyancy is positive (Fig. 5), the level at which effective buoyancy becomes positive is near the LCL and lower than the LFC.

3. The synoptic environment in which the simulated storm developed is discussed in words in manuscript, but no figures (or references to figures in other papers) are included. While the focus of this study is not the storm environment, it would be helpful to readers if a representative environmental sounding/hodograph were included in the manuscript to help the reader visualize the storm environment. It would also provide context for interpreting the some of the results discussed in the manuscript (related to point 2 above). An EF4 tornado produced by an HP supercell (as it is described in the text) is not very commonplace, and readers will be curious about the storm environment. It would also be helpful if a figure illustrating the storm structure at/near tornadogenesis time were included to provide readers with some context on the storm structure/features as they relate to the developing tornado.

Thank you for your suggestion. In fact, at least two previous studies have already examined the storm environment associated with the Funing tornado (Sun et al. 2016; Meng et al. 2018). Fig. 4 in Sun et al. (2016) and Fig. 5 in Meng et al. (2018) both present soundings from the Sheyang station, located approximately 60 km east of the Funing tornadic supercell. Given that this information has been adequately documented, we believe it would be redundant to repeat the discussion here. Furthermore, since our study primarily focuses on tornado intensification and maintenance, a detailed

analysis of the broader storm environment falls outside the scope of this work.

We have cited the specific figures of the two prior studies, showing the environmental conditions, in the revised text, however.

4. It would be helpful if a table of the important model grid/physics options used in the simulation were included in the manuscript. The authors refer readers to another paper for a summary table, yet much of this information is discussed in words in the text (except for the vertical grid spacing near the surface which would be an important for the reader to know). Including a table would help the reader find this information quickly in one place, and the text could be shortened a bit by referring to the table.

Thank you for the suggestions. The choices of PBL and SGS schemes are associated with the strong near-surface deformation where corner flow occurs, while the microphysics and cumulus parameterization schemes would influence buoyancy forcing. Therefore, we provide the above information in the manuscript. While providing a table could help readers locate the information quickly, our study does not focus on the simulation configuration itself, and using text allows us flexibility in give more or less details on certain schemes depending on their relevance to tornado simulations.

5. The discussion on page 29 is somewhat confusing as the arguments presented are based on the forcing terms associated with the 'tornado vortex', but the p' maxima shown in Fig. 13, 14 do not correspond with the locations of the maximum forcing terms and it's not clear the cross section shown in Fig. 11 captures this fact. Based on what is shown in the Fig. 13, 14, it appears that the broader mesocyclone flow is playing a significant role in p' distribution from deformation, not just the flows associated with the tornado vortex and other vortices. This weakens the argument made in the manuscript that it is the strengthening of the tornadic vortex which increases the deformation field (and the magnitude of the 'splat' term in the p' calculations) as it appears the strengthening of the low-level mesocyclone could also be playing a key role in this process. It would be helpful the authors could address this issue and clarify their arguments.

Thank you for pointing out that the locations of the maximum of the deformation term were not consistent with the corresponding p'_{st} maxima in Fig. 13 and Fig.14. The figures have been revised to accurately to reflect the p'_{st} maxima and the associated flow patterns, as shown in the updated Figs. 13 and 14.

Note that the distribution of p' is expected to appear smoother than that of its corresponding forcing term, since the forcing term is the second derivatives of pressure. As a result, small-scale variations in p' may be difficult to identify directly, but they become more apparent after second derivative. Therefore, the distributions of the p'_{st} and its associated forcing term are not accurately aligned.

Despite of apparent inconsistency, the locations of the strongest p'_{st} and the strongest deformation are in fact consistent. The distributions of larger p'_{st} values associated with e_{11}, e_{22}, and e_{12} all shift to the west side of the tornado, rather than displaying symmetric patterns. Similarly, the p'_{st} components associated with e_{13} and e_{23} shift to the west and north sides of the tornado, respectively. The larger p'_{st} values are located on the north and west sides of the tornado, consistent with Fig. 11d. To avoid confusion, we have added interpretations about the patterns between p'_{st} and the flow patterns are not strictly consistent as follows:

"Note that the patterns of the p'_{st} (the second row of Fig. 13) and of the associated forcing term (the first row of Fig. 13) do not appear closely matched. This should be because that the forcing term is the second derivatives of pressure; the pattern of p' is expected to be smoother than that of corresponding forcing term therefore small-scale variations in p' are much less pronounced."

We agree that the low-level tornado cyclone, embedded within a broader mesocyclonic circulation, plays an important role in enhancing deformation. Without the upward suction associate with the low-level tornado cyclone, convergence would not intensify, and consequently, deformation would remain weak. This point was noted in the summary and discussion section of the original manuscript, and is reproduced here:

"It is important to note that, although the spin term becomes negative after tornadogenesis, the role of the mesocyclone is still important. The mesocyclone now acts as a background structure in which the tornado vortex is embedded, promoting a broader region of strong updraft and correspondingly strong low-level convergence. The mesocyclone supports the overall convergence and merging of smaller vortices or horizontal vorticity within the airstream into the main vortex center."

Just an additional comment: The 'summary' paragraphs at the end of each of the results sections were very helpful in summarizing the main points/findings in each section, and are much appreciated by the reader given all the detail provided in the text and figures.

We are glad that the summary paragraphs at the end of each results section are helpful and appreciate your acknowledgment of this effort.

Minor Comments:

1. Lines 87-91: This is a bit of a run-on sentence. Recommend breaking this into two sentences.

This sentence is rewritten as following

"Buoyancy and dynamic vertical PGF are the two primary mechanisms driving updraft acceleration. The key questions are: how much does each of them contribute to the total forcing as the air parcels rise from near ground through the main storm updraft. In the case of dynamic PGF, which components of the flow are responsible for the perturbation pressure patterns that generate these PGFs?"

2. How was the EF4 rating determined? Is there a similar tornado rating system in China?

The EF4 rating of the Funing tornado was determined based on a field damage survey. Xue et al. (2016) has provided documentation of the survey results. Three unmanned aerial vehicles were deployed to analyze the damage path of the tornado. According to their analysis, the EF4 classification is supported by observations. They are reproduced here:

"Figure 1b shows extensive damages to single-family farmhouses, with most of them completely flattened to the ground, although the debris mostly remains on or near the foundations, indicating EF4 damage."

The tornado rating system in China also depends on the maximum near-surface wind speed. It consists of four levels.

The relationship between China's tornado intensity scale and the U.S. Enhanced Fujita (EF) scale is as follows:

- Level one corresponds to EF0 and weaker,
- Level two corresponds to EF1,
- Level three corresponds to EF2 and EF3, and
- Level four corresponds to EF4 and EF5.

Xue, M., K. Zhao, M. Wang, Z. Li, and Y. Zheng, 2016: Recent significant tornadoes in China. Adv. Atmos. Sci., 33, 1209–1217, https://doi.org/10.1007/s00376-016-6005-2.

3. Line 266: Referring to the 'rerun', was this simulation rerun with WRF?

Yes, the model output used by Sun et al. (2019) has a temporal resolution of 1 minute, which is too coarse to adequately resolve the evolution of tornado intensification and maintenance processes.

4. Line 303: What does 'converted' mean in this context? Interpolated? Or is there more involved?

We have added interpretation as follows:

"The vertical and horizontal grids are same between WRF and ARPS. Only some variables are interpolated to ARPS grid."

5. Line 308: A hyphen is needed in 'near-surface'.

A hyphen has been added.

6. Fig 1: The labels/units on the figure axes are missing.

The labels/units on the Fig.1 have been added.

7. Fig. 2: It's hard to reconcile the stated 'view' with what is shown in the plots in Fig. 1. It looks like the view is looking south (not west). Is this correct? Is the area shown the same as in Fig. 1? There are no tick marks or labels on the figure axes to provide any clues. It would also be helpful if each panel were enclosed in a bounding box so it would be more clear which time labels are associated with each plot.

Thank you for this suggestion. The viewpoint corresponds to that of an observer located on the east side of the domain, looking toward the west. To avoid confusion, we have revised the caption of Fig.2 to clarify the orientation. We also add labels indicating the south side of the domain and the location of

the RFGF in the new Fig. 2a. The scale height of the tornado vortex is now indicated by black lines. Additionally, the horizontal extents in the y-direction for each panel have been included in the revised caption. The updated caption for Fig. 2 is reproduced below:

"Volume-rendered ζ (isosurfaces at 0.15, 0.2, 0.3, 0.4 s^{-1}), surface potential temperature (shaded, K), and surface ζ (contours at 0.1 s^{-1}) at the lowest model level from 0701 to 0706. The vertical black lines indicate the scale height of the tornado vortex and then the tornado in each panel. View is toward the west. The southern part of the domain is labeled in (a). The position of rear-flank gust front (RFGF) is labelled by cyan line in (a). Because the camera views are slightly different to better display the structure of the tornado vortex/tornado, the horizontal scales of the domains vary in each panel. In panels (a) through (f), the horizontal extents in y direction are ~5.5, 3.2, 5.5, 4.5, 4.5, and 4.1 km, respectively."

8. Lines 502-503: Recommend removing the part of the sentence in parenthesis.

The sentence in parenthesis has been deleted.

9. Fig. 9 and 10: The orange and black contours are difficult to see against the dark green/blue backgrounds. Also recommend making the labels inside the figures thicker so they are easier to read (note also that one of the labels in figure 1f is cut off).

Thank you for the suggestions. We have revised the orange and black contours to a white–gray–black contours for improved visibility in new Figs.9, 10, and 11. The transparency of the isosurfaces for perturbation pressure has been removed to enhance clarity. Additionally, the isosurfaces of dynamic perturbation pressure, as well as those associated with the spin and splat terms, are now plotted at intervals of 200 Pa and 300 Pa, respectively, instead of 100 Pa, to reduce visual clutter. The vertical labels within the figures have also been thickened for better readability.

10. Fig. 11: The red/orange contours are difficult to see against the red/orange shading.

The orange and black contours have been revised to a white–gray–black contours in new Fig.11.

11. Line 692: It would be helpful if the times corresponding to 'the period' were state explicitly.

This sentence has been rewritten as "The p'_{st} associated with shearing and stretching deformation, and the corresponding flow patterns are shown in surface horizontal and vertical cross sections at 0704 as p'_{st} increases substantially and becomes the strongest after tornadogenesis".

12. Is the timestep used in trajectory calculations the same as the 1s interval in model output? (p 31) This is not clearly stated in the text.

Yes. We have added "The time step for trajectory integration is 1 second" in Section 6.

13. Also on page 31, could the authors explain why were there different areas used for the trajectory calculations?

We have added interpretation as following:

"The parcels are selected to cover both the primary tornado vortex and the surrounding small vortices. At 0703, the tornado vortex region occupies a smaller area than at 0702 due to convergence"

14. Line 769: Recommend changing the text 'ultimately sucked into….' to make it less colloquial.

This sentence has rewritten as

"Some parcels are initially drawn into those small vortices surrounding the central vortex (Fig. 15b–e), and are ultimately entrained into the main vortex together with the small vortices as they merge into the main vortex by 0706:00 (Fig. 15f)."

15. Fig 16 is a bit confusing. The height axis on the y-z 'sidewall' is backwards from what one would expect by 'folding up' the sidewall. The grey lines are also hard to see.

We have revised the orientation of the z-axis in Fig. 16a such that the smaller z-values in the y–z planes for parcels A and B are now positioned closer to the x–y plane. And the grey lines have been thickened.

16. Line 954: Recommend clarifying what 'further up' means.

Thank you for your suggestion, this sentence is written as

"Shortly before reaching their LCL, positive buoyancy becomes the primary and essential driving force for accelerating the air parcels to higher altitudes."

17. Line 967: The text states that 'It is clear that the spin term is responsible for the rapid lifting of the air parcel off (the) ground, and the associated stretching causes tornadogenesis'. If the parcel is being lifted off the ground, how could this be causing tornadogenesis at the surface? This statement needs to be clarified/rewritten.

This sentence has been rewritten as follows:

"It is clear that the spin term is responsible for the rapid lifting of the air parcel off the ground, which enhances low-level convergence as additional parcels are drawn into the developing vortex. The strong convergence with the associated vertical stretching near the surface facilitates tornadogenesis."

18. There are many grammatical errors throughout the text. Below is a list of the lines containing the start of sentences with grammatical errors. Sentence starting on line:

60
166
181
218
452
640
648
652
766
967
970
999
1006
1027
1030
1040
1112

Thanks for your suggestion, we have corrected these errors.

What Forces the Rapid Vertical Acceleration and Vorticity Intensification Near Ground in Tornadoes? Diagnostic Analysis based on a Numerically Simulated Real Tornado

Wei Huang[a] and Ming Xue[b]

[a] *Key Laboratory of Mesoscale Severe Weather/Ministry of Education and School of Atmospheric Sciences, Nanjing University, Nanjing, Jiangsu 210023, China*

[b] *Center for Analysis and Prediction of Storms and School of Meteorology, University of Oklahoma, Norman, OK 73072, USA*

Submitted to J. Atmospheric Science

2/28/2025

Revised 6/23, 2025

Corresponding author

Ming Xue, mxue@ou.edu

ABSTRACT

A numerical simulation of a real-case supercell tornado is analyzed to understand the rapid vertical acceleration of near-surface air parcels leading to intense vertical vorticity stretching and vortex intensification. The vertical acceleration is primarily due to effective buoyancy force and dynamic vertical perturbation pressure gradient force (VPPGF), and the latter is further decomposed into the splat and spin components by solving diagnostic pressure equations. Positive dynamic VPPGF is the dominant forcing responsible for near-ground vertical acceleration, while effective buoyancy is much smaller near ground. In the initial stage of tornado vortex intensification, upward dynamic VPPGF is dominated by the spin term associated with the vorticity of lowering tornado cyclone embedded within a mesocyclone, because maximum vertical vorticity and associated perturbation pressure minimum are located off the ground. After tornadogenesis occurs, the maximum vertical vorticity and corresponding perturbation pressure minimum shift to the ground level, the dynamic VPPGF due to spin becomes negative or downward. At this stage, upward VPPGF associated with the splat term is found to be responsible for promoting and supporting continued upward vertical acceleration and vorticity stretching near the ground. The splat component is largest near the ground and close to the corner region of tornado vortex because of the strong flow deformation there. Trajectory analyses of parcels entering the tornado vortex further substantiate that the dominant term in the upward dynamic VPPGF transitions from the spin term before to the splat term after tornadogenesis. Afterwards, buoyancy becomes the primary force for continued updraft acceleration, usually shortly before reaching the lifting condensation level.

SIGNIFICANCE STATEMENT

The important role of low-level intense vertical acceleration in tornadogenesis has been highlighted in recent studies because of the resulting near-ground vertical vorticity stretching. However, quantitative analyses on the buoyancy force and dynamic pressure gradient force (PGF) causing such vertical acceleration are generally lacking. The flow patterns responsible for the dynamic PGF are not well understood either. Through both Eulerian and trajectory-based Lagrangian analyses, this study finds that dynamic forcing is the primary driver of low-level vertical acceleration. Before tornadogenesis, the upward dynamic PGF near the low-level tornado vortex is mainly attributed to the spin term

associated with mesocyclone rotation, while after tornadogenesis, the spin term reverse sign and the splat term associated with deformation flows becomes the dominant contributor. The important role of dynamic PGF associated with the splat term in tornado dynamics has not been explicitly recognized before in the tornado literature.

1. Introduction

Supercell tornadogenesis typically involves three steps as described by Davies-Jones (2015). The first step is the formation of a mesocyclone through the upward tilting of horizontal vorticity associated with environmental vertical wind shear by thermally driven updraft. This process has been extensively studied and is well understoood (Lilly 1982; Rotunno and Klemp 1982; Davies-Jones 1984; Weisman and Rotunno 2000). The second step is the formation of near-ground rotation at ground (Davies-Jones 2015). Steps 1 and 2 are necessary, but not sufficient for supercell tornadogenesis (Coffer et al. 2023). The final step for tornadogenesis is the contraction of near-ground rotation into a tornado-strength vortex. The contraction is associated with strong updrafts with intense vertical acceleration (and strong horizontal convergence) near the surface, which can provide strong stretching to intensify vertical vorticity. Without strong stretching, tornadogenesis will fail even with sufficient vorticity near the ground (Parker 2023). It is commonly believed that the strong near-surface vertical stretching is primarily driven dynamically, by the low-level mesocyclone or the tornado cyclone embedded within, which generates negative dynamic pressure perturbations at the rotation center. This, in turn, establishes a strong upward pressure gradient force (PGF) beneath the strong rotation, promoting vertical acceleration and stretching. Here, a tornado cyclone is defined as a cyclone smaller in size than a mesocyclone but large than a typical tornado funnel (Brooks 1949; Fujita 1958). Tornado cyclone is usually embedded within the mesocyclone circulation (Brown and Wood 1991; Ziegler et al. 2001) and often extends downward above a developing tornado but is not tornado itself.

In the simulation conducted by Coffer and Parker (2015) and Coffer et al. (2017), tornadic supercells with strong mesocyclones have more intense updrafts and are capable to converge and stretch the vortex tube, while the updrafts in non-tornadic supercells are weaker due to disorganized mesocyclone. Roberts and Xue (2017) showed that in their supercell simulation with surface drag applied to the full wind, the intensification and lowering of the mesocyclone toward the ground generates a strong upward PGF leading to tornadogenesis. In contrast, in the simulation with drag applied only to the base-state wind (i.e., not to storm-induced perturbation wind), the mesocyclone only intensifies and lowers modestly and tornadogenesis fails to occur. Flournoy et al. (2020) also found that tornadic cases have stronger low-level mesocyclones to promote stretching and lifting compared to non-tornadic cases. The critical role of low-level mesocyclone in tornadogenesis has also

been substantiated in the observational study of Houser et al. (2015), using rapid-scan, polarimetric, Doppler radar observations on a supercell with two tornadoes.

Some studies have investigated specifically the forcing mechanisms of strong updrafts in severe storms (Rotunno and Klemp 1982; Klemp and Rotunno 1983; Weisman and Klemp 1984; McCaul and Weisman 1996; Weisman and Rotunno 2000; Peters et al. 2019). Buoyancy and dynamic vertical PGF are the two possible mechanisms driving updraft acceleration. The key questions are: how much does each of them contribute to the total forcing as the air parcels rise from near ground through the main storm updraft. In the case of dynamic PGF, which components of the flow are responsible for the perturbation pressure patterns that generate these PGFs? Analyzing a suite of idealized supercell simulations under different environmental conditions, Peters et al. (2019) found that the maximum updrafts in the simulated supercells are to a larger extent determined by the buoyancy while the positive dynamic pressure acceleration, though helpful, is significantly offset by downward buoyant pressure acceleration. In simulations of non-supercell thermal convection, vertical acceleration has been found to be dominated by buoyancy and buoyancy-induced pressure forcing (Peters 2016; Morrison and Peters 2018). We note that these studies do not focus specifically on near-surface vertical acceleration, however. Another aspect of the dynamic perturbation pressure is its effect on the air parcel density therefore buoyancy; larger negative perturbation pressure within tornadoes corresponds to lower air density and larger positive buoyancy that can help enhance updraft within tornadoes. This effect is emphasized by Dawson et al. (2016) in a simulated tornado-like-vortex (TLV) where negative perturbation pressure is significant.

The dynamic perturbation pressure associated with different components of the flow can be obtained by solving the elliptic diagnostic pressure equation. By decomposing the wind field into the environmental and perturbation components and solving the linearized diagnostic pressure equation, Rotunno and Klemp (1982) pointed out that dynamic PGF would preferentially enhance updraft growth on the right flank of the storm in a veering environmental wind shear. This result was further supported by numerical simulations in Klemp and Rotunno (1983) and Weisman and Klemp (1984). In numerical simulations of tornado-producing landfalling hurricanes, the upward dynamic PGF can contribute three times as much to the maximum updraft speed as does explicit buoyancy (McCaul and Weisman 1996). The important role of dynamic forcing in tornadogenesis is also underscored by Coffer et al. (2017) and Coffer and Parker (2018).

The nonlinear component of dynamic forcing refers to the dynamic perturbation pressure primarily induced by rotation and strain within the storms (Hastings and Richardson 2016). Weisman and Rotunno (2000) further confirmed earlier results of Rotunno and Klemp (1982, 1985) and stated that "the physical processes that promote storm maintenance, rotation, and propagation are similar for all hodograph shapes employed, and are due primarily to nonlinear interactions between the updraft and the ambient shear, associated with the localized development of rotation on the storm's flank". Davies-Jones (2002) derived a formal solution of the Poisson equation for nonhydrostatic (dynamic) pressure and also found the important role of non-linear dynamic pressure forcing in supercell storm maintenance. Comparing low-shear with strong-shear environments, the latter is associated with stronger non-linear dynamic forcing that leads to an intense cyclonic vortex near the surface (Markowski and Richardson 2014; Goldacker and Parker 2021). The development of strong surface vortices under high-shear and low-CAPE (convective available potential energy) environment is also found to be closely linked to strong non-linear dynamic forcing (Sherburn and Parker 2019). Within an ensemble of simulated supercells, stronger non-linear dynamic forcing is found in the tornadic ensemble members compared to nontornadic members (Flournoy et al. 2020).

The non-linear forcing term in the diagnostic pressure equation can be further decomposed into "spin" and "splat" terms (Rowland 1880; Bradshaw and Koh 1981; Davies-Jones 2002). The spin and splat terms are associated with rotation and deformation of fluid, respectively. The spin term, together with the associated dynamic PGF, is what has been emphasized in most of the earlier studies on supercell storm maintenance, rotation, and propagation (Rotunno and Klemp 1982, 1985; Weisman and Rotunno 2000; Davies-Jones 2002). Positive spin component of non-linear dynamic forcing associated with strong mesocyclone rotation is well recognized as an important factor in tornadogenesis (Coffer and Parker 2015, 2017). For supercells in high-shear, low-CAPE environments, Wade and Parker (2021) found that the largest vertical velocities result from dynamic accelerations associated with low-level mesocyclones and vortices, not from buoyancy. Low-CAPE tornado-like vortex parcels also sometimes stop ascending near the vortex top instead of carrying large vorticity upward into the midlevel updraft. These behaviors are attributed to dynamic perturbation pressure gradient accelerations that are maximized at lower levels. Some studies found that buoyancy and nonlinear dynamic forcing are equally important for the intensification and maintenance of supercell updrafts. Davenport and Parker (2015)

found that buoyancy and nonlinear dynamic accelerations had similar effects on supercell evolution as the storm environment changes. The importance of buoyancy and nonlinear dynamic forcing for tornadogenesis is also emphasized by Yokota et al. (2018) in a real case supercell tornado simulation. The evolution in total vertical acceleration was found to be primarily related to changes in accelerations that were connected to updraft rotation as well as changes in buoyancy.

The prior studies have clearly established the importance of dynamic perturbation pressure in promoting vertical acceleration that is important for both supercell storms and supercell tornadoes, although some studies have shown equal importance of buoyancy. The relative importance may also be case dependent. Most of the previous studies focused on the updrafts at the storm scale, based on simulations using grid spacings of 250 m or larger (e.g., McCaul and Weisman 2001), while a few used grid spacings between 50 and 250 m and examined vertical accelerations affecting TLVs (e.g., Coffer and Parker 2015; Yokota et al. 2018; Flournoy et al. 2020). For the dynamic perturbation pressure, discussions were almost exclusively focused on the strong vertical rotation associated with the mesocyclone that produces negative pressure perturbations and therefore upward PGF underneath, and many of such studies only explained such effects qualitatively. One important issue that has received little attention is that when a tornado does occur, the largest vertical vorticity and therefore the largest negative perturbation pressure associated with the spin term are found very close to the ground (Davies-Jones 2015; Houser et al. 2015; Bluestein et al. 2019; Roberts et al. 2020). In such a case, downward vertical perturbation PGF (VPPGF) would be found within the tornado vortex which would promote downdraft. Therefore, an important unresolved question is: What force(s) is/are responsible for the intense near-ground upward vertical acceleration that is critical for tornado maintenance after tornadogenesis?

In this study, we want to answer the above question by analyzing the simulation of a real tornado case. This tornado happened in Funing, Jiangsu Province, China, and was successfully simulated by Sun et al. (2019). Specifically, we aim to address the following questions: How much do buoyancy and dynamic forces each contribute to the low-level vertical acceleration in an incipient and established tornado? What flow features among the rotational and deformation flow components that are related to the spin and splat terms in the diagnostic pressure equation are responsible for the dynamic perturbation pressure and what are their effects on the near-surface vertical acceleration?

The remainder of the paper is organized as follows: Section 2 offers an overview of the Funing tornado case. The vertical acceleration terms in the moment equation, and components within the diagnostic pressure equations and the solution procedure are also presented. Section 3 describes the rapid intensification processes of the simulated Funing tornado. Section 4 gives detailed analyses of the dynamic PGF and buoyancy force at the tornado vortex scale and discusses their impacts on low-level vorticity stretching and intensification. The components of dynamic perturbation pressure and the associated flow features are discussed further in Section 5. In Section 6, parcel trajectory-based analyses are conducted to determine the quantitative contributions of dynamic and buoyancy forcings to vertical acceleration along the trajectories. A summary and discussions are given in Section 7.

2. Methodology

a. Case Overview

An EF4 tornado occurred in Funing County of Yancheng City, Jiangsu Province, China, in the afternoon of June 23, 2016. This tornado formed within a supercell located south of the Meiyu rainband. Funing was located southeast of a shallow 500-hPa trough extending from a cold vortex in northeast China. The 700-hPa trough to the northwest and the 850-hPa jet to the southwest transported rich water vapor to Funing (Fig. 2 in Meng et al. 2018 and Fig. 3 in Sun et al. 2019). The 0-6 km wind shear was greater than 27 m s^{-1}, and the lowest 1 km wind shear was 8.7 m^{-1} km^{-1} veering with height from southeasterly to southerly. The CAPE and CIN were 2663 J kg^{-1} and 8 J kg^{-1}, respectively (Fig. 5 in Meng et al. 2018 and Fig. 4 in Sun et al. 2019). The dynamic and thermodynamic conditions are favorable for tornadogenesis. The supercell storm, the Funing tornado occurred, was a heavy precipitation (HP) type (Meng et al. 2018; Sun et al. 2019). The Funing tornado formed at approximately 0615 UTC (1415 LST), then moved east-northeast, and reached EF4 intensity at about 0620 and again 0635 UTC (all times will be in UTC hereafter unless otherwise noted). The tornado dissipated after about half an hour.

Sun et al. (2019) successfully simulated the Funing tornado using the advanced research version of the Weather Research and Forecasting (WRF-ARW) model (Skamarock et al. 2008) with five nested grids. The horizontal grid spacings of the five nested grids are 4000, 1333, 444, 148, and 49 m, and the time steps are 25, 8.33, 2.78, 0.93, and 0.31 s,

respectively. All domains have 51 vertical levels, with a vertically stretched grid. The lowest model level for scalar and horizontal velocity variables is at about 26 m above ground level (AGL), with 10 model levels residing within the lowest 1 km. The innermost domain uses the fully three-dimensional 1.5-order turbulent kinetic energy (TKE)-based subgrid-scale (SGS) turbulence closure scheme based on Deardorff (1974), and the remaining four grids use Smagorinsky deformation-based horizontal SGS turbulence mixing parameterization (Smagorinsky 1963). All grids use the 2-moment Morrison microphysics scheme (Morrison and Grabowski 2008). The Pleim-Xiu land surface and surface layer models (Pleim 2006) coupled with the Asymmetric Convective Model (Version 2, ACM2) PBL scheme (Pleim 2007) are used on all grids. Cumulus parameterization is not used. The detailed model configuration and experiment settings can be found in Section 4 in Sun et al. (2019). The timing and location of the simulated tornado differ somewhat from the observations. The simulated tornado intensifies from 0700, and the formation of a TLV with the maximum vertical vorticity being located very close to the ground occurs shortly after 0703 (1503 LST), later than the observations (at ~0630). The path of the simulated tornado is further north than observed (c.f. Fig. 15 in Meng et al. 2018 and Fig. 11 in Sun et al. 2019). Considering that the intensification mechanism of tornado is the focus of our study, the time and location errors are not a major concern. Our analyses in this paper are all based on the results of the innermost domain of 49 m grid spacing, and the simulation of Sun et al. (2019) is rerun to produce output at 1-second intervals to improve the accuracy of trajectory calculations and associated diagnostics. We note here that the horizontal and vertical grid spacings are both about 50 m near the ground, which may be considered only marginal in resolving the corner flow structure within developed a tornado. The tornado simulated may be more appropriately called a TLV, but for simplicity we will call it tornado in this paper.

b. Vertical accelerations and pressure diagnostics

The vertical momentum equation with Coriolis force neglected is written as

$$\frac{dw}{dt} = -\frac{1}{\rho}\frac{\partial p'}{\partial z} + B + F, \qquad (1)$$

where w is the vertical velocity, B is the buoyancy associated with density variations, $-\frac{1}{\rho}\frac{\partial p'}{\partial z}$ is the VPPGF, and F represents frictional force and other mixing/diffusion

processes in the model including the subgrid-scale turbulent mixing. The total perturbation pressure p' can be decomposed into dynamic perturbation pressure induced by the flow (p'_d) and the perturbation pressure induced by buoyancy (p'_b). Eq. (1) hence can be written as

$$\frac{dw}{dt} = \underbrace{-\frac{1}{\rho}\frac{\partial p'_d}{\partial z}}_{DVPPGF} \underbrace{\underbrace{-\frac{1}{\rho}\frac{\partial p'_b}{\partial z}}_{BVPPGF} + B}_{EB} + F. \quad (2)$$

The first term on the right-hand side (RHS) of Eq. (2) is the dynamic VPPGF (DVPPGF), and the second term is the buoyancy-induced VPPGF (BVPPGF). The sum of second and third terms (i.e., BVPPGF and B) on the RHS is referred to as "effective buoyancy" (EB) (Davies-Jones 2003).

The dynamic perturbation pressure p'_d can be derived as a solution to the Poisson equation

$$\boldsymbol{\nabla}^2 p'_d = -\boldsymbol{\nabla} \cdot (\rho \boldsymbol{V} \cdot \boldsymbol{\nabla} \boldsymbol{V}), \quad (3)$$

where $\boldsymbol{\nabla}^2$ is the three-dimensional Laplacian operator. The RHS of Eq. (3) is responsible for the total DVPPGF and can be expanded into

$$-\boldsymbol{\nabla} \cdot (\rho \boldsymbol{V} \cdot \boldsymbol{\nabla} \boldsymbol{V}) = -\frac{\partial \rho}{\partial x}\boldsymbol{V} \cdot \boldsymbol{\nabla} u - \frac{\partial \rho}{\partial y}\boldsymbol{V} \cdot \boldsymbol{\nabla} v - \frac{\partial \rho}{\partial z}\boldsymbol{V} \cdot \boldsymbol{\nabla} w - \rho\left(\frac{\partial(\boldsymbol{v}\cdot\boldsymbol{\nabla}\mathbf{u})}{\partial x} + \frac{\partial(\boldsymbol{v}\cdot\boldsymbol{\nabla}\boldsymbol{v})}{\partial y} + \frac{\partial(\boldsymbol{v}\cdot\boldsymbol{\nabla}\boldsymbol{w})}{\partial z}\right), \quad (4)$$

with *u* and *v* being the horizontal velocity components. The first three terms on the RHS of Eq. (4) are associated with the product of the density gradient and velocity advection. The VPPGF induced by these terms is denoted as RHOVPPGF, which is often overlooked in previous studies under Boussinesq assumption. These terms are retained when solving the Poisson equation in our case, though they are relatively small. The terms in the parentheses on the RHS of Eq. (4) are the primary forcing terms of DVPPGF, which can be further expanded

$$-\rho\left(\frac{\partial(\boldsymbol{v}\cdot\boldsymbol{\nabla}\mathbf{u})}{\partial x} + \frac{\partial(\boldsymbol{v}\cdot\boldsymbol{\nabla}\boldsymbol{v})}{\partial y} + \frac{\partial(\boldsymbol{v}\cdot\boldsymbol{\nabla}\boldsymbol{w})}{\partial z}\right) =$$

$$-\rho\left[\left(\frac{\partial u}{\partial x}\right)^2 + \left(\frac{\partial v}{\partial y}\right)^2 + \left(\frac{\partial w}{\partial z}\right)^2\right] - 2\rho\left(\frac{\partial v}{\partial x}\frac{\partial u}{\partial y} + \frac{\partial w}{\partial x}\frac{\partial u}{\partial z} + \frac{\partial w}{\partial y}\frac{\partial v}{\partial z}\right) - \rho\boldsymbol{V} \cdot \nabla D, \quad (5)$$

where

$$D = \boldsymbol{\nabla} \cdot \boldsymbol{V} = \frac{\partial u}{\partial x} + \frac{\partial v}{\partial y} + \frac{\partial w}{\partial z}. \quad (6).$$

The first and second terms on the RHS of Eq. (5) can be rewritten as the sum of "splat" and "spin" terms following Bradshaw (1981):

$$-\rho\left[\left(\frac{\partial u}{\partial x}\right)^2 + \left(\frac{\partial v}{\partial y}\right)^2 + \left(\frac{\partial w}{\partial z}\right)^2\right] - 2\rho\left(\frac{\partial v}{\partial x}\frac{\partial u}{\partial y} + \frac{\partial w}{\partial x}\frac{\partial u}{\partial z} + \frac{\partial w}{\partial y}\frac{\partial v}{\partial z}\right) = \underbrace{-\rho e_{ij}^2}_{splat} + \underbrace{\frac{1}{2}\rho|\boldsymbol{\omega}|^2}_{spin}, \quad (7)$$

where $e_{ij} = \frac{1}{2}\sum_{i=1}^{3}\sum_{j=1}^{3}\left(\frac{\partial u_i}{\partial x_j} + \frac{\partial u_j}{\partial x_i}\right)$ is the deformation tensor, where $u_1 \equiv u$, $u_2 \equiv v$, $u_3 \equiv w$, $x_1 \equiv x$, $x_2 \equiv y$, and $x_3 \equiv z$. Deformation is also known as the rate-of-strain tensor crudely associated with eddy collisions (Bradshaw and Koh 1981; Adrian 1982). Deformation describes fluid elements that are stretched or sheared by velocity gradients (Markowski and Richardson 2010). The deformation term is also called the "splat" term, and the VPPGF induced by the splat term is denoted as STVPPGF herein. The deformation includes stretching deformation (when $i = j$) and shearing deformation (when $i \neq j$). Large deformation is associated with confluence, diffluence, and shear (Djurić 1994). $\boldsymbol{\omega}$ is the three-dimensional vorticity vector. $\frac{1}{2}|\boldsymbol{\omega}|^2$ is called the "spin" term associated with rotation (Bradshaw and Koh 1981; Adrian 1982), and the VPPGF induced by spin is denoted as SNVPPGF. The remaining term on the RHS of Eq. (5) is associated with the divergence advection (referred to as DAVPPGF). DAVPPGF is generally ignored in previous studies because of the often-made non-divergence assumption $\boldsymbol{\nabla} \cdot \boldsymbol{V} = 0$ (Markowski and Richardson 2010). For the sake of completeness, we retain DAVPPGF although it is small compared with STVPPGF and SNVPPGF.

The dynamic forcing can also be expressed as the sum of shear and extension terms (Klemp and Rotunno 1983; Rotunno and Klemp 1985; Wakimoto and Cai 2000; Dahl 2024). However, Davies-Jones (2002) argued that this form is variant to the rotation of the x and y axes about the z axis. Instead, he proposed decomposing dynamic forcing into the sum of splat and spin terms, which are invariant under three-dimensional rotations of the coordinate axes.

Within the effective buoyancy term, the contribution of BVPPGF generally opposes that of B, thus considering only B can lead to an overestimation of buoyancy (Houze 2014; Jeevanjee and Romps 2016). Additionally, both BVPPGF and buoyancy depend on the choice of base state, while EB only depends on horizontal variations in the density field,

as discussed by Davies-Jones (2003) and Doswell and Markowski (2004). Therefore, using EB to assess the contribution of buoyancy is more appropriate. In our case, $\frac{dw}{dt}$ is calculated by Eq. (1), and DVPPGF is obtained by solving Eq. (3). The effective buoyancy is then calculated as a residual between the sum of the model diagnosed VPPGA ($-\frac{1}{\rho}\frac{\partial p'}{\partial z}$) and buoyancy ($B$), and DVPPGF terms. The contribution of friction F is small compared to the other three terms in Eq. (2) and is not separated in our study.

The multigrid solver mud3cr available in MUDPACK (Adams 1989) is utilized to solve the Poisson equations with different forcing terms on the RHS to obtain different components of $p'$and the corresponding VPPGF. This method was used by Dawson et al. (2016) and then by Schenkman et al. (2016) for the equations formulated on the Advanced Regional Prediction System (ARPS; Xue et al. 2001) terrain-following grid. The lateral boundary conditions are homogeneous Dirichlet conditions for faster convergence, following Dawson et al. (2016). The results are not sensitive to the choice of either Neumann or Dirichlet conditions. The top and bottom boundary conditions used to solve p' and VPPGF are Neumann and Dirichlet conditions, respectively. More details can be found in Dawson et al. (2016). For our study, the WRF model outputs are converted to the ARPS grid using an existing tool in the ARPS package before applying the multigrid Poisson solver. The horizontal grid and vertical model levels are defined to be effectively the same between WRF and ARPS, although WRF employs a hydrostatic pressure-based vertical coordinate while ARPS uses a flexible height-based vertical coordinate. The heights of the ARPS model levels are derived from the geopotential heights of the hydrostatic-pressure-based WRF model levels. Therefore, the grid conversion mainly involves conversions among selected WRF and ARPS state variables.

3. The evolution of tornado vortex intensification in the simulation

Before 0700, the main near-surface vortex near the later developed TLV has gone through several enhancement processes in the Funing tornado simulation, but the vortex soon weakens and cannot form a tornado (not shown). During 0700–0706, the incipient vortex intensifies dramatically, and a tornado successfully forms. When this happens, the maximum vertical vorticity is located very close to the ground, essentially at the first model level above the ground, that is about 26 m AGL. Fig. 1 shows the horizontal cross sections

at ~26 m AGL from 0701 to 0706. To better visualize this process, the 3D view of vertical vorticity, ζ, is also given in Fig. 2. As described in Sun et al. (2019), six small vortices (labeled as V1–6) that originally develop along the occluded gust front on the north side of the vortex (Fig. 2) revolve counterclockwise around and converge into the developing tornado (V0 in Fig. 1a); they are finally drawn into the tornado vortex V0 one by one by strong spiraling convergent flows from 0701 to 0706 (Fig. 1 and Fig. 2). At 0701, the low-level tornado cyclone and the surface vortex V0 appear disconnected when rendered using vorticity isosurfaces above 0.15 s^{-1}; at least there are two local maxima existing at different altitudes (Fig. 2a). Here, by "tornado vortex" refers to a pre-tornadic column of air with relatively large vertical vorticity and a diameter typically ranging from 100 m to 1 km, which ultimately develops into a tornado (Bluestein et al. 2018). The maximum ζ associated with the mid-level tornado cyclone is located at about 3 km (Fig. 2a). The surface vortex exhibits a "vorticity ring" structure (Fig. 1a) that is typically associated with "two-cell" tornadoes (Davies-Jones et al. 2001). Relatively weak vortex V1 is on its south side and ready to be absorbed into V0 (Fig. 1a).

By 0702, the core of tornado cyclone has descended to a much lower altitude of about 1 km (Fig. 2b). The near-surface vortex V0 now exhibits an oval-shaped "single cell" structure where the maximum ζ is located at the center of vortex (Fig. 1b). The contraction of V0 is clearly related to the strong near-surface convergence and the associated vertical stretching at its center, but it remains disconnected from the tornado cyclone aloft when viewed in terms of the 0.15 s^{-1} ζ isosurface (Fig. 2b). This disconnection indicates the presence of a weaker low-level tornado cyclone around 1 km. The characteristic that the low-level tornado cyclone appears weaker than the vortex above and below just before and during tornadogenesis is similar to the vertical structure of the tornado vortex signature (TVS) based on high-resolution radar data (French et al. 2013; Houser et al. 2015; Bluestein et al. 2019).

By 0703, as the tornado cyclone descends further and the surface vortex develops upward, the two become connected, as indicated by the 0.15 ζ isosurface. The maximum vertical vorticity in the overall column is now quite close to the surface. At this moment, the middle-level tornado cyclone actually weakens slightly and appears disconnected from the low-level tornado cyclone at the vorticity iso-surface thresholds shown (Fig. 2c). Very shortly afterward, at 0703:20 (not shown), the maximum ζ shifts to the surface, i.e., the

surface vorticity exceeds that aloft and is significantly increased (Fig. 1d and Fig. 2d). At this point, strong vertical vorticity becomes continuous from the ground upward, signifying successful tornadogenesis. Here, our definition of tornadogenesis is consistent with high-resolution radar studies focusing on tornadogenesis evolution (French et al. 2013; Houser et al. 2015; Bluestein et al. 2019), where a tornado is considered to be successfully formed when the low-level mesocyclone (corresponding to low-level tornado cyclone in our study) intensifies to align with strong near-surface rotation, resulting in a coherent tornado column. Because of the presence of multiple small vortices, some of which exhibit stronger near-surface vorticity than the tornado vortex V0 at some times, we choose to identify tornadogenesis mainly based on the structural changes within the tornado vortex, rather than specific thresholds of surface wind speed and/or vertical vorticity, as done in some simulation studies (e.g., Schenkman et al. 2014; Roberts et al. 2016; Markowski 2024).

By 0704, the vorticity isosurfaces associated with the low-level tornado grow upward and is fully connected to the tornado cyclone above (Fig. 2d); the tornado vortex has evolved into a deep column of strong cyclonic rotation that can be called a tornado (or a TLV as in some studies, where the ~50 m horizontal grid spacing is believed to be insufficient to fully resolve the detailed circulation structures of a tornado – in this paper we choose to call it tornado). At this time, the surface vortex appears quite symmetric with a one-cell-like structure and vortices V1–3 have been absorbed into the tornado (Fig. 1d). The tornado is best organized at 0704 and its intensity is strongest at this time among the figures shown (Fig. 1d and Fig. 2d). The tornado becomes asymmetric again and slightly weakens after 0705 (Fig. 1f and Fig. 2f) and a vorticity ring/two-cell structure re-establishes at 0706 (Fig. 1f and Fig. 2f). After 0706, the tornado maintains an asymmetric single-cell structure until 0716, and then evolves into five sub-vortices due to barotropic instability of the vortex ring (figure not shown; see Huang and Xue 2023). Due to strong low-level convergence, vortices V1–5 are drawn into the tornado vortex then tornado through the pre-tornadic, tornadogenesis, and maintenance phases from 0701 and 0706 (Fig. 1). This suggests that the rapid vertical acceleration at the tornado vortex location, along with the accompanying strong near-surface convergence, is critical for vortex merger and subsequent intensification via vertical stretching. The phenomenon that a lowering tornado cyclone embedded within a mesocyclone circulation connects with upward developing surface vortex in terms of two local maxima at different altitudes to form a tornado has also been documented using radar data in Skinner et al. (2014) and Houser et al. (2015).

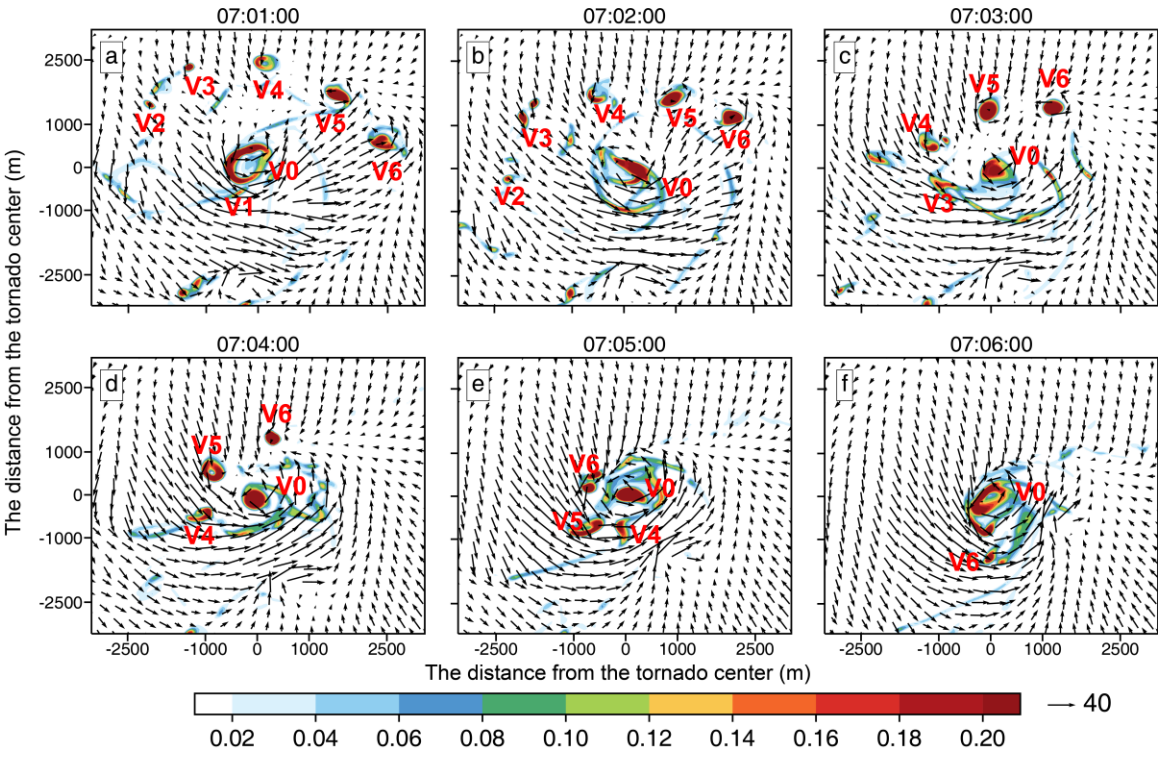

403

404 Fig. 1. Horizontal cross sections of vertical vorticity ζ (shaded, s^{-1}) and horizontal
405 wind vectors ($m \cdot s^{-1}$) at ~26 m AGL from 0701 to 0706. The coordinate origin
406 follows tornado vortex and later tornado V0, and the axis unit is meter.

407

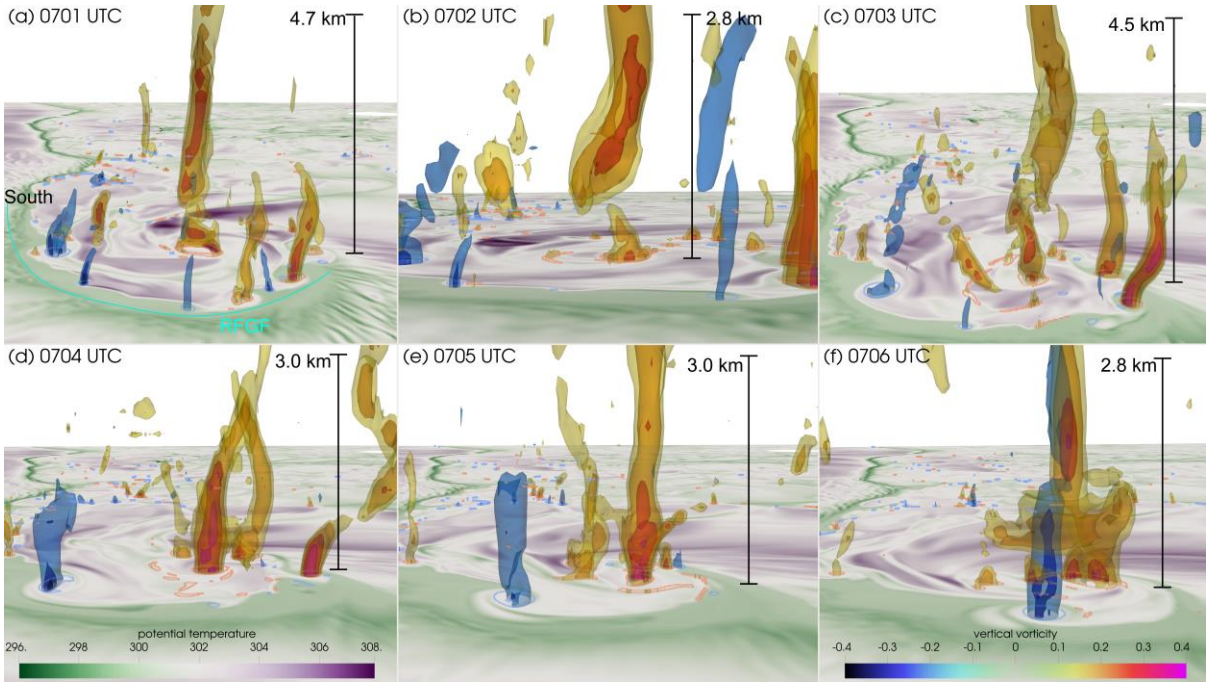

408

409 Fig. 2 Volume-rendered ζ (isosurfaces at 0.15, 0.2, 0.3, 0.4 s^{-1}), surface potential
410 temperature (shaded, K), and surface ζ (contours at 0.1 s^{-1}) at the lowest model level
411 from 0701 to 0706. The vertical black lines indicate the scale height of the tornado
412 vortex and later tornado in each panel. View is toward the west. The southern part

of the domain is labeled in (a). The position of rear-flank gust front (RFGF) is labelled by cyan line in (a). Because the camera views are slightly different to better display the structure of the tornado vortex/tornado, the horizontal scales of the domains vary in each panel. In panels (a) through (f), the horizontal extents in y direction are ~5.5, 3.2, 5.5, 4.5, 4.5, and 4.1 km, respectively.

To see further the connection between surface vorticity and low-level vertical acceleration, the time series of the maximum ζ at the lowest model level (~26 m AGL) and the vertical acceleration at 400 m AGL are shown in Fig. 3. In the initial stage of the vortex intensification, the maximum values of ζ and vertical acceleration associated with vortices V1-V6 can be greater than those of vortex V0 (Fig. 1). To focus on the main central vortex that evolves into the tornado, the maximum values are calculated within a small region surrounding V0. When other vortices are absorbed into V0, they are considered part of V0. Fig. 3 shows that the increase in near-surface vertical acceleration is followed by an increase in ζ. Vertical acceleration starts to increase from 0701:15 and soon after, the enhanced stretching results in an increase in ζ from 0702:40. Vertical acceleration reaches its maximum at 0702:45 while ζ reaches its maximum at 0703:30. The rapid intensification of near-surface ζ between 0702:40 and 0703:30 corresponds to tornadogenesis. The correlation coefficient between the two time series is maximized at 0.945, when the time series of vorticity maximum lags behind that of vertical acceleration by 51 seconds. This suggests a direct role of updraft forcing and acceleration, and the resulting vertical stretching in the intensification of near-surface vorticity.

After tornadogenesis, near-surface ζ slightly briefly decreases between 0703:30 and 0704. The decrease in ζ lags behind a sharp decrease in vertical acceleration that begins around 0702:40. After 0705:20, vertical acceleration increases significantly once again, also followed by a notable increase in ζ after 0706. The changes in near-surface vertical acceleration leading to changes in ζ is evident, confirming the important role of low-level vertical acceleration and the associated stretching in tornado vortex intensification, which is also noted in studies such as Robertson (2017) and Sherburn and Parker (2019). The enhancement and maintenance of strong upward vertical acceleration between 0701 and 0706 and their causes will be the focus of this study.

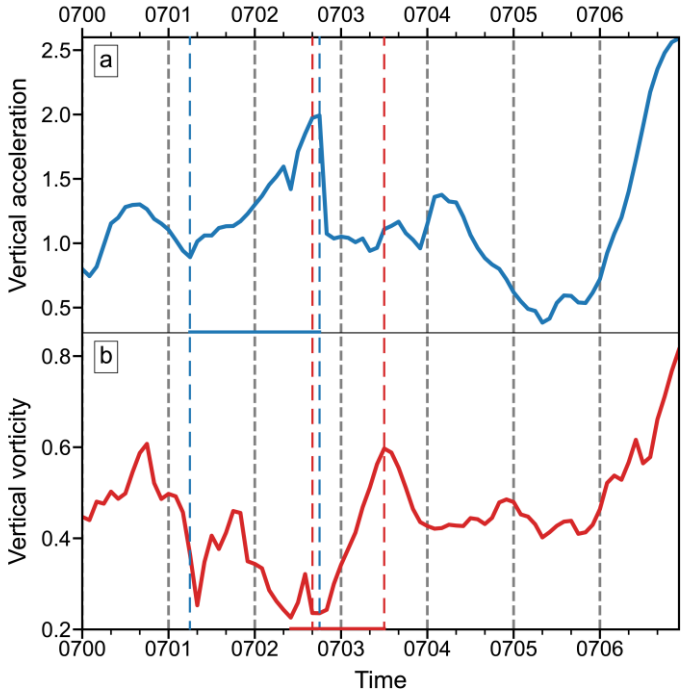

Fig. 3 Time series of (a) maximum vertical acceleration (m s^{-2}, blue line) and (b) maximum ζ (s^{-1}, red line) at the lowest model level (~400 m AGL) from 0700:00 to 0706:00. The blue and red vertical lines represent the start and end times of the increase in vertical acceleration and ζ, respectively.

4. Diagnostics of vertical accelerations responsible for tornado vortex intensification

To find out what terms are responsible for the rapid increase and maintenance of upward vertical acceleration and subsequent tornado vortex intensification, the acceleration terms in the vertical momentum equation are diagnosed that involves solving the elliptic perturbation pressure equation. Figure 4 shows the dynamic forcing (DVPPGF; second row) and effective buoyancy forcing (EB; third row), and the total vertical acceleration (WACCEL; first row) at the 400 m height. The friction/diffusion term F is very small, so that WACCEL is effectively the sum of DVPPGF and EB (see Eq. 2). The 400 m height is between the tornado cyclone and the developing surface tornado. The fields are overlaid with vertical vorticity at ~26 m AGL.

From 0701 to 0706, the spatial distributions of DVPPGF and WACCEL are very similar, and the DVPPGF maxima match those of WACCEL closely (first and second rows of Fig. 4), indicating the dominant contribution of DVPPGF to total WACCEL. At 0701

(Fig. 4g), there is an asymmetric distribution of DVPPGF near the ring-shaped V0 vortex, with positive values on the western portion of the vortex and negative values on the north side. At 0702 (Fig. 4h), the positive DVPPGF is enhanced and is located on the south side of the main vortex V0 (c.f., Fig. 1b) while weaker negative values occupy the north part. At 0703, V0 becomes stronger and more circular (c.f. Fig. 1c), positive DVPPGF now occupies most of the V0 vortex region except for a small area near its center (Fig. 4i), and the largest positive values are on the east side. By 0704 (Fig. 4j), positive values of DVPPGF are even larger and are mostly found on the north to northwest part of the vortex, while the negative values on the southern portion are also larger. Overall, between 0701 and 0704, positive DVPPGF increases in both area coverage and magnitude, and shows a tendency to revolve cyclonically around the vortex center, while negative DVPPGF maintains a generally similar magnitude and has a tendency to shift toward the vortex center. Such tendencies are related to the lowering of tornado cyclone and the development of the surface tornado after 0703. The former increases the positive upward DVPPGF below the tornado cyclone, while the latter creates negative downward DVPPGF near the center of the surface vortex following tornadogenesis. At 0705 (Fig. 4k) and 0706 (Fig. 4l), negative DVPPGF occupies more areas near the vortex center, with positive values of DVPPGF found mainly at the edge of the vortex. As we will discuss further later, after the tornado forms, positive low-level DVPPGF has to come from the splat term, while the spin term contributes negatively near the vortex center. While we discuss these, we should keep in mind that the DVPPGF shown here is at 400 m AGL, not at the level of the surface vortex.

The value of EB is always positive at the tornado center; its value is much smaller compared with DVPPGF, at no more than 0.2 m s^{-2} between 0701 and 0706, suggesting that EB only plays a small, although positive role in the low-level vertical acceleration and hence tornado intensification. Buoyancy will become increasingly larger as the parcels rise off the ground, as seen later in trajectory analyses.

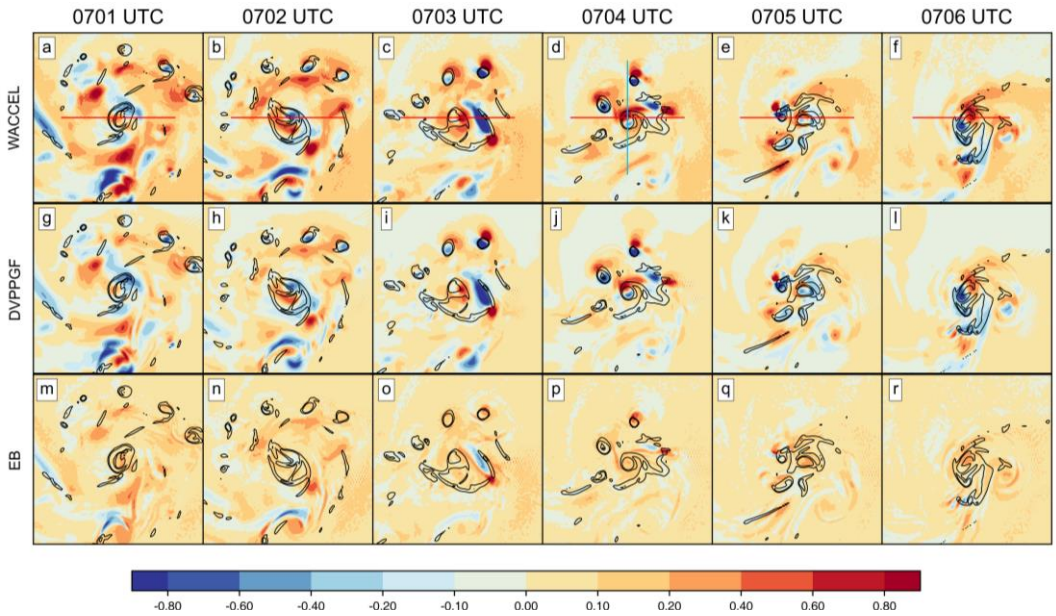

Fig. 4. Horizontal cross sections of (a–f) WACCEL, (g–l) DVPPGF, and (m–r) EB at about 400 m AGL from 0701 to 0706 (shaded, m s^{-2}) overlaid with ζ at the lowest model level about 26 m AGL (black contours at 0.05, 0.15 s^{-1}). Red straight lines in (a-f) indicate the positions of vertical cross sections shown in Fig. 5. While blue line in (d) indicates the position of the vertical cross section shown in Fig. 14a and d. The region plotted is 6×6 km^2.

Vertical cross sections near the center of tornado vortex V0 (along the red lines in Fig. 4) are plotted in Fig. 5 to reveal the vertical structures of WACCEL, DVPPGF, and EB. In the vertical cross sections, the distributions of WACCEL and DVPPGF are again very similar (first and second rows in Fig. 5). Given the dominant contribution of DVPPGF to WACCEL, our remaining analyses will mainly focus on DVPPGF, and will also examine its components. Between 0701 and 0702, the positive values of DVPPGF are primarily found between 500 and 1500 m AGL, below or in the lower part of the tornado cyclone (Fig. 5g and h). The DVPPGF may not be symmetric around the tornado cyclone (Fig. 5g). At 0702, the 8 m s^{-1} *w* contour reaches below ~1 km level at the vortex location. By 0703, the proceeding strong vertical acceleration has increased the low-level updraft dramatically, with the 8 m s^{-1} *w* contour extending to about 200 m AGL (Fig. 5c). Some of the ζ contours of the tornado cyclone now extend all the way to the ground while the highest 0.3 s^{-1} contour is between 400 m and 1 km level (Fig. 5c). The positive upward DVPPGF becomes primarily concentrated below 700 m AGL (Fig. 5i), indicating a strong vertical pressure gradient and associated acceleration at very low levels. This leads to intense vertical velocity divergence, which stretches near-surface vertical vorticity and causes

tornadogenesis within the following minute. By 0704, the tornado has formed with the maximum vorticity located at the surface (Fig. 5j). Within the cross-section shown in Fig. 5j, positive DVPPGF is mainly below 500 m AGL, while strong negative values have developed at and above the mesoscale core (seen in terms of the positive ζ contours). After tornadogenesis, especially after 0705, negative DVPPGF is seen extending to the surface at the location of tornado core (near-surface ζ maximum), although positive DVPPGF values are also found very close to the surface, mostly on the sides of the tornado (Fig. 5j–l). Our later analyses will show that the splat term is responsible for such positive values. The DVPPGF distribution causes the strongest updraft and associated stretching to occur at the edge of tornado core, and they also rotate counterclockwise around the tornado core, as discussed earlier. The resulting tornado and associated forcing structure are asymmetric (Fig. 4).

Before 0703, there is a very thin surface layer of negative EB, which may be related to the lower boundary condition. Overall, EB is mostly positive (Fig. 5m–o). After 0704, positive EB becomes more organized in the column of main vortex and stronger (Fig. 5p-r) but it is always smaller than DVPPGF in magnitude (note the difference in color tables in Fig. 5). To sum up, dynamic forcing is the dominant term of vertical acceleration and thus primarily responsible for low-level vortex intensification, while buoyancy forcing plays a weak but positive role. Before tornadogenesis, low-level positive upward dynamic PGF intensifies as the tornado cyclone lowers. Once tornadogenesis occurs, dynamic PGF becomes negative at the tornado center while positive dynamic PGF develops at the sides of tornado core, which is clearly responsible for continued upward parcel acceleration that supports vorticity stretching and tornado maintenance.

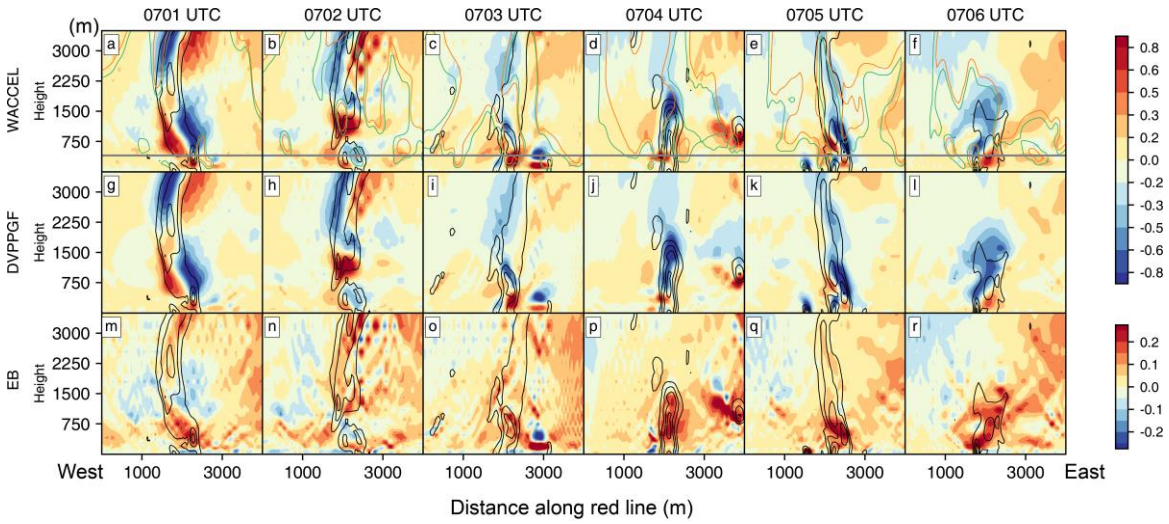

Fig. 5 Vertical cross sections of (a–f) WACCEL, (g–l) DVPPGF, and (m–r) EB from 0701 to 0706 (shaded, m s^{-2}) overlaid with ζ (black contours at 0.1, 0.2, 0.3, 0.4 s^{-1}) and w (green and orange contours at 5, 8 m s^{-1}, respectively) along the red line from west to east in each respective panel of Fig. 4. Grey straight lines in (a-f) indicate the positions of horizontal cross sections shown in Fig. 4 and the axis unit is meter.

To understand the contributions of different flow components to the dynamic PGF, we decompose DVPPGF into SNVPPGF, STVPPGF (third and fourth rows of Fig. 6), RHOVPPGF (first row of Fig. 7), and DAVPPGF (second row of Fig. 7), and they are associated with the spin, splat, density gradient and divergence advection terms, respectively, in Eqs. (4)-(5). The right-hand side of Eq. (3) responsible for the total DVPPGF is directly calculated from the moment advection terms calculated by the ARPS model subroutines and shown in the first row of Fig. 6. STVPPGF, SNVPPGF, RHOVPPGF, and DAVPPGF are calculated from diagnosed pressure perturbations associated with the respective forcing terms on the right-hand side of the elliptic diagnostic pressure equation, as given in Eqs. (4) and (5). Their sum is given as DVPPGF_t in the second row of Fig. 6. The patterns of DVPPGF and DVPPGF_t are similar, except for some negative values east of tornado in DVPPGF_t (Fig. 7g–l) not present in DVPPGF (Fig. 6a–f). Such discrepancy is the result of differences in the finite difference operations performed on different quantities defined on the staggered C grid; several finite differencing/spatial averaging operations are applied to arrive at the forcing terms. The overall similarity between DVPPGF and DVPPGF_t indicates the general correctness of our decomposition calculations.

Between 0701 and 0703, the positive DVPPGF near the tornado vortex is primarily attributed to SNVPPGF, with the positive SNVPPGF aligning well with positive DVPPGF (Fig. 6m–o and a–e). The small differences between DVPPGF and SNVPPGF, especially in magnitude, are attributable to STVPPGF, whose values often oppose those of SNVPPGF at the same locations (Fig. 6s–u and m–o). The negative STVPPGF at 0702 (Fig. 6t) or the small positive STVPPGF at 0701 and 0703 near the tornado center (Fig. 6s and u) indicate that STVPPGF makes a relatively small contribution to DVPPGF between 0701 and 0703.

However, STVPPGF becomes the dominant term in DVPPGF after 0704 (Fig. 6v–x) when the tornado has formed (Fig. 2d–f). From 0704, positive STVPPGF dominates at the tornado center (Fig. 6v–x), while SNVPPGF is mostly negative and rather strong (Fig. 6p–

r), with only a small area of positive SNVPPGF present at 0706 (Fig. 6r). Fortunately, the areas of the strongest positive STVPPGF offset those of strongest negative SNVPPGF, so that their sum (that also includes two other smaller terms) has strong positive total DVPPGF that is usually located off the tornado center where negative DVPPGF is found, especially after tornadogenesis (1st and 2nd rows of Fig. 6). Thus, the splat term is responsible for providing the strong positive near-surface vertical acceleration that is necessary for supporting strong near-surface vertical stretching that sustains tornado, and its positive contribution is also seen before tornadogenesis. The important role of the STVPPGF terms in an established tornado and possibly also in a developing tornado had not been explicitly or quantitatively discussed in the prior literature to our knowledge, and therefore deserves research attention. The contributions of the remaining RHOVPPGF (Fig. 7a–f) and DAVPPGF (Fig. 7g–l) terms are much smaller and can be considered negligible.

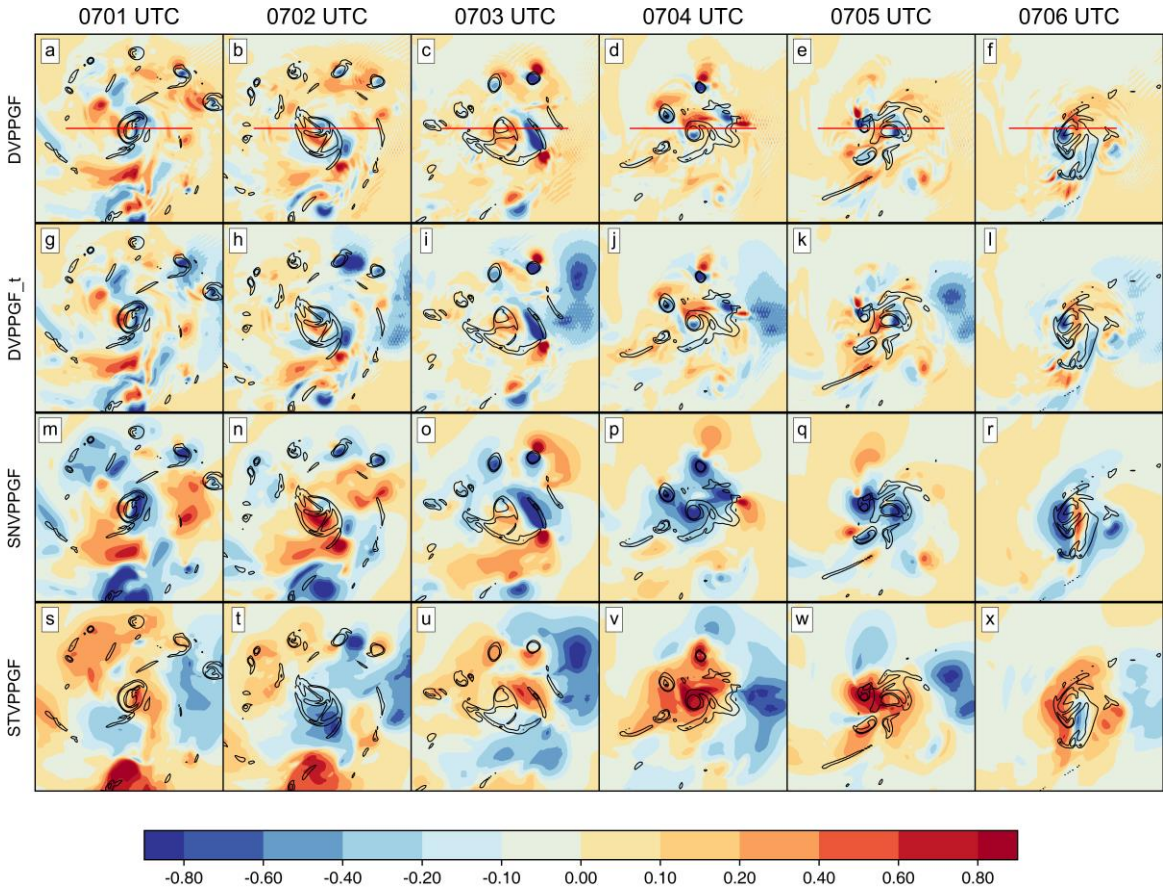

Fig. 6 As in Fig. 4, but for (a–f) DVPPGF directly calculated from the moment advection terms calculated by the ARPS model subroutines, (g–l) DVPPGF calculated as the sum of STVPPGF, SNVPPGF, DAVPPGF and RHOVPPGF, denoted as DVPPGF_t, and the components of DVPPGF (m–r) associated with spin (SNVPPGF) and (s–x) associated with splat (STVPPGF).

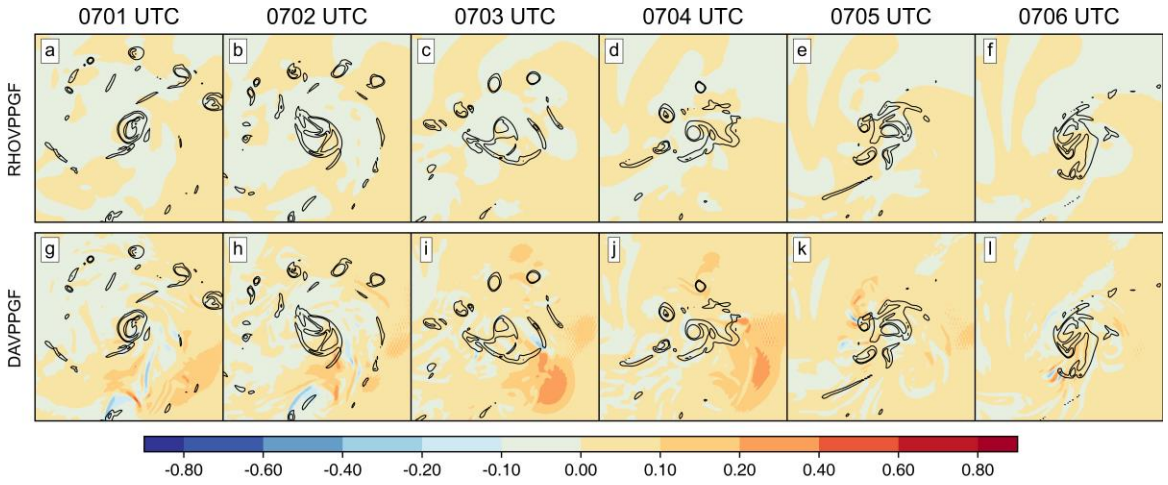

Fig. 7 As in Fig. 4, but for the components of DVPPGF (a–f) associated with density gradient (RHOVPPGF) and (g–i) associated with divergence advection (DAVPPGF).

Given the negligible contributions of RHOVPPGF and DAVPPGF, we will only present STVPPGF and SNVPPGF in the vertical cross sections (Fig. 8). Similar to the results shown in Fig. 6, from 0701 and 0703, the dominant contribution to DVPPGF is SNVPPGF, as indicated by the similar patterns of DVPPGF and SNVPPGF (Fig. 8a–c and g–i). The pattern of STVPPGF is in general opposite to that of SNVPPGF, therefore acts to reduce the effect of SNVPPGF. There is a tendency for a decrease in the elevation of the main positive values of SNVPPGF from 0701 and 0703. The lowering of positive DVPPGF and consequently WACCEL is therefore primarily linked to SNVPPGF with the downward development of the tornado cyclone. STVPPGF is generally positive near the surface but smaller in magnitude than SNVPPGF during this period (Fig. 8m–o).

There are dramatic changes in the patterns of SNVPPGF and STVPPGF in the vertical cross sections between 0703 and 0704 when tornadogenesis occurs. The positive values of SNVPPGF disappear completely in the tornado region at 0704, while the negative values increase significantly in magnitude, especially above 500 m height (Fig. 8j). At the same time, the positive values of STVPPGF also increase significantly, with the largest values found between ~300 to 700 m, and the positive values extend all the way to the surface especially on the west side of tornado core (Fig. 8p). Due to the opposing and somewhat offset patterns of SNVPPGF and STVPPGF, their sum gives rise to the pattern shown in Fig. 8d. In this pattern, negative DVPPGF dominates the vortex center column from ~500 m upward, while positive DVPPGF extends from that level downward to the surface,

flanking a small region of negative DVPPGF at the surface vortex core. We point out here that due to the choice of the vertical cross-section location of Fig. 8d as indicated in Fig. 6d, this cross-section does not cut across the largest positive and negative values of DVPPGF at the lower levels. If a northwest-southeast cross section is chosen, large positive values on the north-northwest side of the surface vortex, and large negative values near the vortex center will be more clearly seen, illustrating more clearly the asymmetric pattern of near-surface DVPPGF as the spin and splat term contributions evolve. Again, the splat term is responsible for providing the positive near-surface dynamic forcing after tornadogenesis, and to a smaller extent before tornadogenesis also.

In summary, the above analyses suggest that the primary contribution to the vertical acceleration within a developing and established tornado, as simulated here, is dynamic forcing, while buoyancy forcing is weakly but consistently positive. The spin term is the primary form of positive dynamic forcing before tornadogenesis with the vorticity in the tornado cyclone being greater than that near the surface. Once the surface tornado vortex intensifies and surpasses the strength of the tornado cyclone in terms of vertical vorticity, the contribution of the spin term becomes predominantly negative, and the splat term takes over as the main positive dynamic forcing near the surface. The regions of large (positive or negative) values of the spin and splat terms do not completely overlap, and as a result, the net positive upward dynamic forcing can exist near the surface and is usually located off the tornado center, where the negative spin-term forcing usually dominates. Such a forcing pattern would support the tornado corner flow where the updraft jet ejects off the ground at a small radius from the tornado center (Davies-Jones 1986; Rotunno 2013).

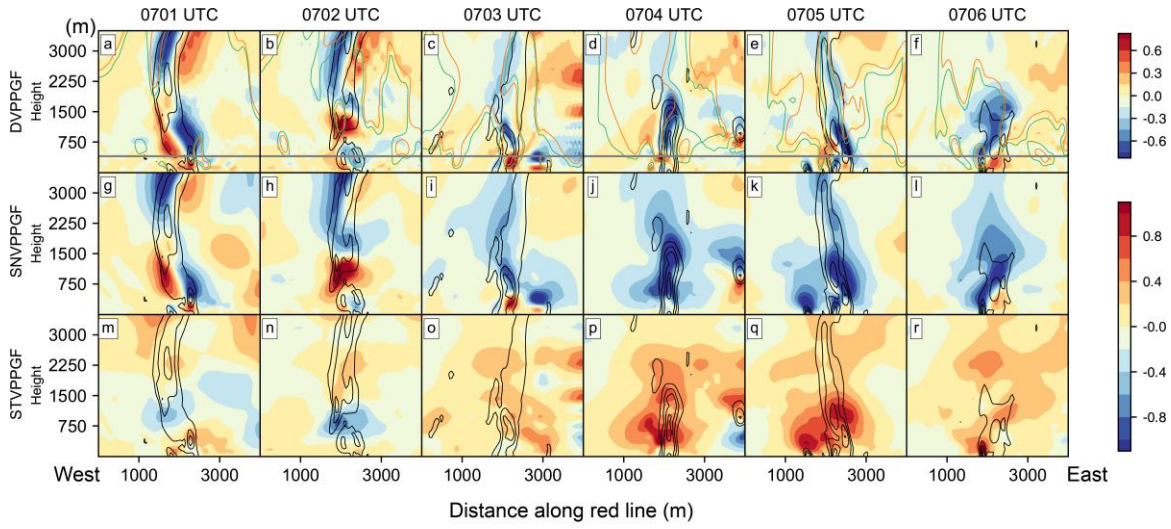

Fig. 8 As shown in Fig. 5, but for (a–f) DVPPGF, (g–l) SNVPPGF, (m–r) STVPPGF.

5. Perturbation pressures and corresponding flows

The important roles of the dynamic PGF, as the sum of the spin and splat term contributions, have been discussed in a number of prior studies with respect to the formation mechanisms of strong updrafts in supercells or tornadoes (e.g., Muehr et al. 2024). However, there is a general lack of quantitative analyses on the respective contributions of the two terms and the related flow processes. In particular, the role of the splat term is rarely analyzed in previously published studies, with most attention paid to the spin term associated with mesocyclone rotation. In this section, we will examine further the low-level flow patterns that produce the distributions of the splat and spin terms.

First, we show in Fig. 9, Fig. 10, and Fig. 11 three-dimensional visualizations of perturbation pressures p'_d, p'_{sn} and p'_{st} which correspond to DVPPGF, SNVPPGF, and STVPPGF, respectively. These figures complement the two-dimensional cross-section plots shown earlier. Because RHOVPPGF and DAVPPGF are much smaller, the corresponding perturbation pressure fields are not shown. Note that the color pallets of p'_d, p'_{sn}, and p'_{st} are different. Also shown in the figures are the vertical cross sections of ζ contours through the vortex core, and horizontal cross sections of ζ near the surface. For well-behaved fields away from the boundaries, $\boldsymbol{\nabla}^2 p'$ is proportional to $-p'$, therefore p'_{st} and p'_{sn} are proportional to the splat term e_{ij}^2 and the negative spin term $-|\omega|^2$, respectively, according to Eq. (7) (Markowski and Richardson 2010). Fig. 10 shows that p'_{st} is all positive near the tornado vortex and then the tornado, while p'_{sn} is all negative in Fig. 11, consistent with the equation. Therefore, at any location, the total perturbation pressure p'_d will be positive when the splat term dominates over the spin term, and is negative if it is the other way around.

Between 0701 and 0703, the minimum p'_{sn} is away from the ground, generating positive VPPGF underneath the minimum. The position of minimum p'_{sn} aligns closely with the position of the tornado cyclone core. As the tornado cyclone develops downward, the height of minimum p'_{sn} (Fig. 10a–c) and hence minimum p'_d (Fig. 9a–c) also lowers from about 2 km to 500 m. Compared to p'_{sn}, the magnitude of p'_{st} is much smaller (compare Fig. 11a–c and Fig. 10a–c). At 0701 and 0702, the maximum of p'_{st} is between

2 km and 1.5 km above ground and therefore creates a downward PGF. At these times, there are weaker secondary maximum values at the ground close to the vorticity maximum, creating weak upward PGF near the surface (Fig. 11a–b). By 0703, the maximum p'_{st} is shifted to the ground level, on the east side of the surface vorticity maximum (Fig. 11c), creating significant upward PGF there (c.f., Fig. 6u).

Tornadogenesis occurs at around 0703:20 when the maximum ζ at the surface exceeds that above (not shown). Correspondingly, the magnitudes of both p'_{sn} (Fig. 10d–f) and p'_{st} (Fig. 11d–f) increase notably, reaching their largest magnitudes around 0704. At 0704, both minimum p'_{sn} and maximum p'_{st} are at the surface, with the minimum p'_{sn} located near the tornado center (Fig. 10d) while the maximum p'_{st} is located somewhat off the tornado center to the northwest side (Fig. 11d). Although the general magnitude of p'_{st} remains smaller than that of p'_{sn} so that their sum p'_d is mostly negative (Fig. 9d), the vertical gradient of p'_{st} can be significant compared to that of p'_{sn}, as indicated by the densely packed p'_{st} isosurfaces in the vertical direction (Fig. 11d). Note that the vertical gradient of p' and PGF are opposite in sign. The downward vertical gradient of p'_{st} is comparable to the upward vertical gradient of p'_{sn}, particularly on the northwest side of the tornado (Fig. 10d and Fig. 11 d), creating net downward vertical gradient of p' and upward dynamic PGF there (c.f., Fig. 6d). While p'_{sn} and p'_{st} are slightly weakened from 0705, the minimum p'_{sn} (Fig. 10e–f) and maximum p'_{st} (Fig. 11e–f) remain at the surface. Consequently, the PGF associated with p'_{sn} and p'_{st} remain downward and upward, respectively. As noted earlier, the p'_{sn} minimum and p'_{st} maximum do not coincide exactly; they are somewhat offset in location. The p'_{st} maximum is usually found on one side of the tornado vortex or tornado center while the p'_{sn} minimum is at the center (Fig. 11c–f), this offset creates net upward dynamic PGF off the center as noted earlier. In addition to the effect on vertical dynamic PGF, we note here that the negative perturbation pressure near the tornado center due to spin creates strong horizontal PGF also that draws air towards the tornado center throughout the period. As the flow accelerates towards the tornado center, the air has to slow down, turn, and flow upward due to mass continuity. The point where the radial inflow terminates also corresponds to the region of maximum flow deformation, which likely explains why the maximum p'_{st} is located slightly off the tornado center. Due to the vortex circulation asymmetry, the maximum p'_{st} often appears on the side where radial inflow is strongest.

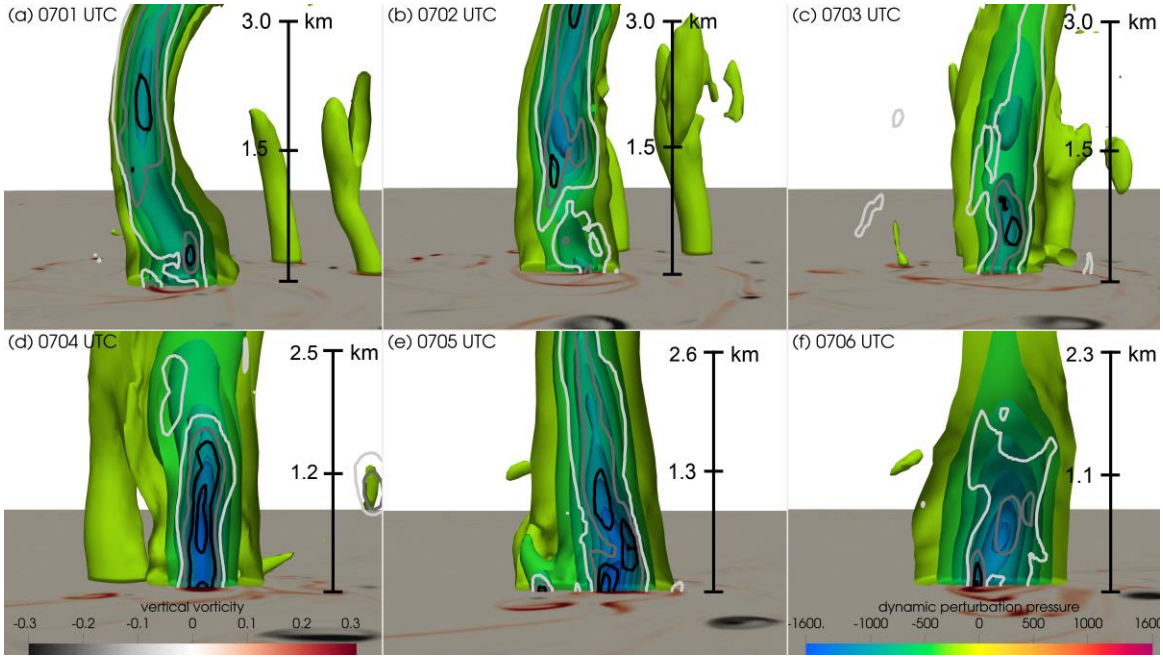

704

705 Fig. 9. Vertical cross sections of three-dimensional isosurface rendering of total
706 dynamic perturbation pressure p'_d (isosurfaces every 200 Pa starting from -200 Pa;
707 the corresponding color palette is at the bottom of Fig. 9f) along the horizontal red
708 line from west to east displayed in the respective panel of Fig. 4. To better show the
709 position of the tornado vortex and the tornado, isosurface rendering is overlaid with
710 vertical cross sections of vertical vorticity (white to black contours at 0.1, 0.2, 0.3,
711 0.4 s^{-1}). Horizontal cross section of vertical vorticity (shaded, m s^{-1}; the
712 corresponding color palette is at the bottom of Fig. 9d) at ~26 m AGL from 0701 to
713 0706. The vertical extent of each panel is indicated. View is toward the north. The
714 horizontal extents in *x* direction of (a–f) are about 5.1, 4.9, 4.9, 3.3, 3.9, and 3.3 km,
715 respectively.

716

717

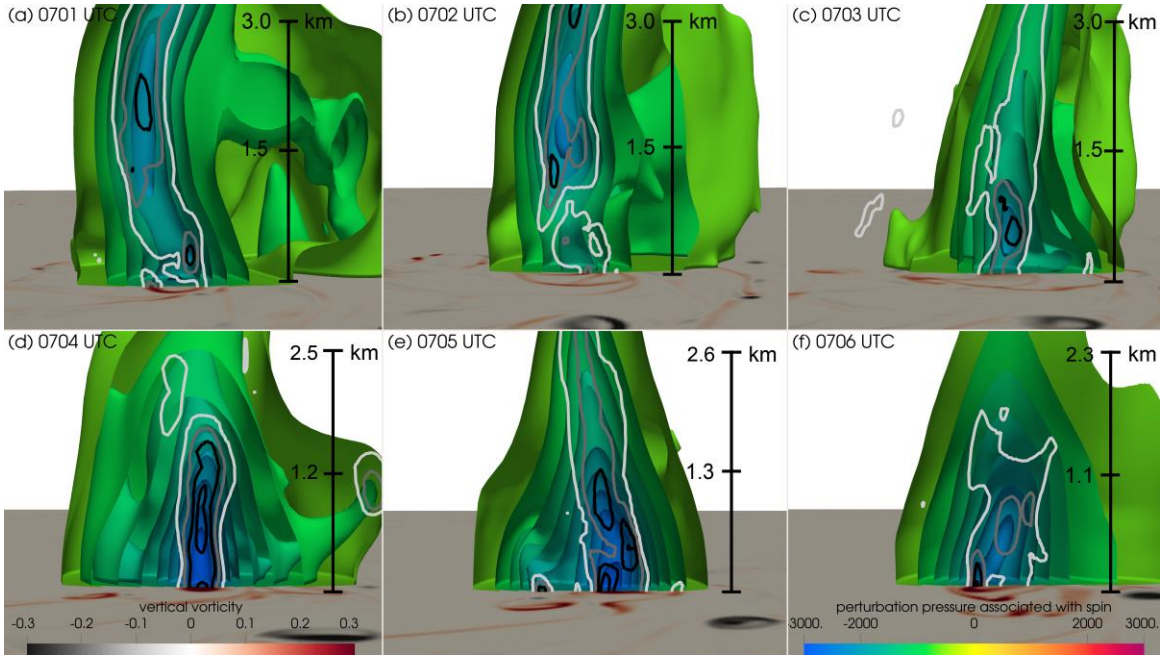

718

719 Fig. 10. As Fig. 9, but the perturbation pressure visualized is the spin component
720 p'_{sn}.The isosurfaces are from -3000 to -600 Pa every 300 Pa.

721

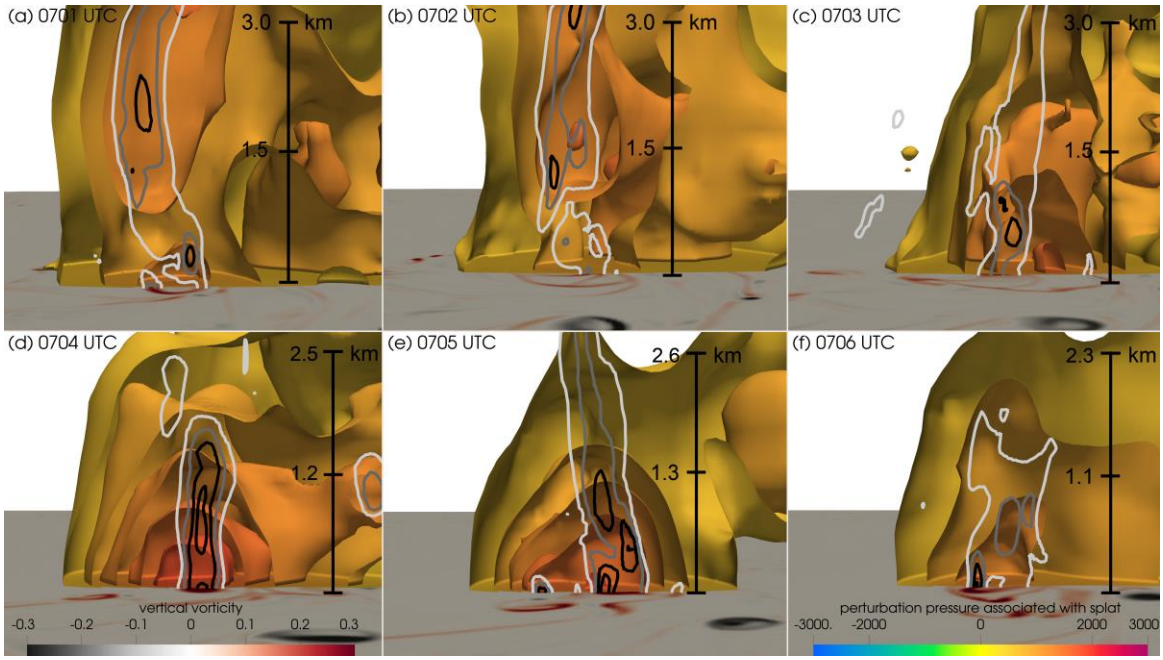

722

723 Fig. 11 Same as Fig. 9, but the perturbation pressure visualized is the splat
724 component p'_{st}.The isosurfaces are from 600 to 3000 Pa every 300 Pa.

725

726 To see how the perturbation pressures associated with the spin and splat terms are linked
727 to different components of the flow fields, we examine the flow features associated with
728 p'_{st} and p'_{sn} next. It is noted that the pressure equation is a diagnostic equation, the

729 solution of the equations does not tell us the cause or effect, it only tells us how certain
730 flow fields must have the corresponding pressure perturbations in order to satisfy the
731 equations of motion and mass continuity (Markowski and Richardson 2010).

732 According to the equations in section 2b, the spin term includes the *x*, *y*, and *z* vorticity
733 components. To see which component makes more contribution, we further diagnose
734 perturbation pressure p'_{sn} associated with the three vorticity components, as shown in Fig.
735 12. We focus on 0701 and 0704, corresponding to the times when the strongest perturbation
736 pressure is aloft and near the ground, respectively (Fig. 9b and d). At both times, the
737 dominant component of p'_{sn} is associated with vertical vorticity (the third column of Fig.
738 12). This result is reasonable, as the magnitude of horizontal vorticity (~10^{-2} s^{-1}) is much
739 smaller than that of vertical vorticity (~10^{-1} s^{-1}) from 0701 to 0706 (figures not shown).
740 This explains the well-aligned positions between vertical vorticity and p'_{sn}. The height of
741 minimum p'_{sn} decreases as the height of maximum vertical vorticity decreases.
742 Additionally, as the tornado vortex/tornado tilts with height (see also Fig. 10), p'_{sn},
743 especially the component associated with vertical vorticity, also tilts accordingly.

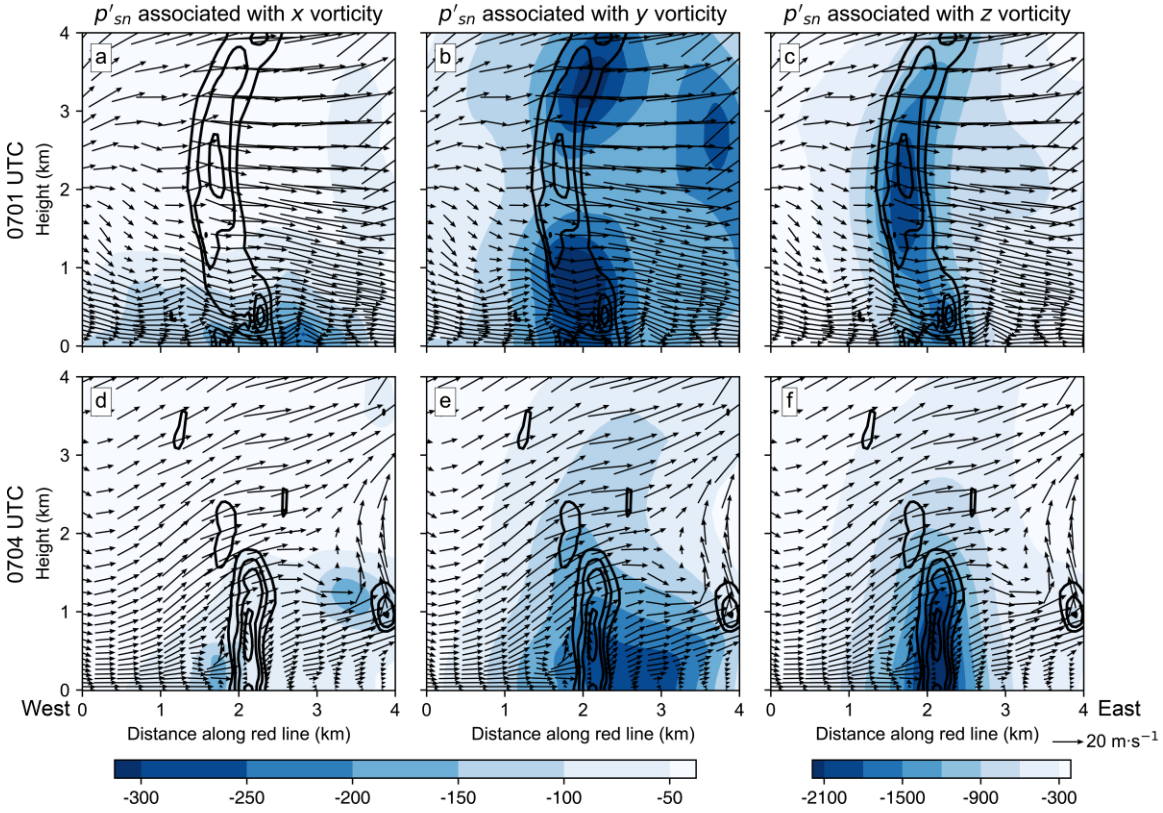

744

745 Fig. 12. Vertical cross sections of p'_{sn} due to (left panels) *x* vorticity, (middle
746 panels) *y* vorticity, and (right panels) *z* vorticity component overlaid with wind
747 vectors and vertical vorticity (contours at 0.1, 0.2, 0.3 s^{-1}) at 0701 (upper panels)

748 and 0704 (lower panels) along the red lines from west to east in Fig. 4a and d,
749 respectively.
750
751 According to section 2b, the splat term has two components: the stretching deformation
752 when $i = j$ in e_{ij} and shearing deformation when $i \neq j$. The p'_{st} associated with shearing
753 and stretching deformation, and the corresponding flow patterns are shown in surface
754 horizontal and vertical cross sections at 0704 as p'_{st} increases substantially and becomes
755 the strongest after tornadogenesis (Fig. 13). Note that the patterns of p'_{st} (the second row
756 of Fig. 13) and of the associated forcing term (the first row of Fig. 13) do not appear closely
757 matched. This is because that the forcing term is the second derivative of pressure; the
758 pattern of p' is expected to be smoother than that of corresponding forcing term therefore
759 small-scale variations in p' are much less pronounced.
760 The stretching deformation describes the rate of change in fluid velocity per unit length
761 associated with convergence or divergence of fluid. For the p'_{st} associated with the
762 stretching deformation (the second row of Fig. 13), the horizontal convergence/divergence
763 components (e_{11} and e_{22}) are the dominant terms (Fig. 13d and e) while the vertical
764 convergence/divergence term (e_{33}; Fig. 13c) is much smaller (Fig. 13a and b). Recall that
765 both divergence and convergence are associated with positive perturbation pressure,
766 consequently, the p'_{st} associated with e_{33} (Fig. 13f) is much smaller than those
767 associated with e_{11} and e_{22} (Fig. 13d and e). We also note that horizontal convergence
768 or divergence (Fig. 13a and b) and the corresponding pressure perturbations (Fig. 13d and
769 e) are the strongest at the periphery of the tornado rather than at its center. As suggested
770 earlier, the strong convergence/divergence occurs because, as the swirling air parcel flows
771 towards the tornado center, it will be halted at certain radius *r* from the tornado center, since
772 the radial wind must vanish at $r = 0$ and the tangential velocity will reach infinity due to
773 the angular momentum conservation at $r = 0$. At the later two-cell stage of the tornado, the
774 central downdraft also acts to prevent the near-surface radial inflow from reaching
775 excessively small radii. Due to mass continuity as well as the increase in centrifugal force,
776 the swirling air rushing in from all directions must abruptly slows down, turn, and flow
777 upward (Bluestein 2013). Therefore, the radial convergence is largest at the periphery of
778 tornado core, especially at the west and north edges. As a result, the horizontal
779 convergence/divergence, along with the associated p'_{st}, are strongest near the edge of
780 tornado core and their maxima are shifted to its west and north sides, rather than being

centered on the tornado. This pattern is also evident in Fig. 11. In an observational study of Wakimoto and Cai (2000), positive perturbation pressure was found to the south and southeast of the mesocyclone, where the rear-flank gust front was located with strong convergent flow. Their study did not present the actual distribution of perturbation pressure associated with convergence/divergence, however.

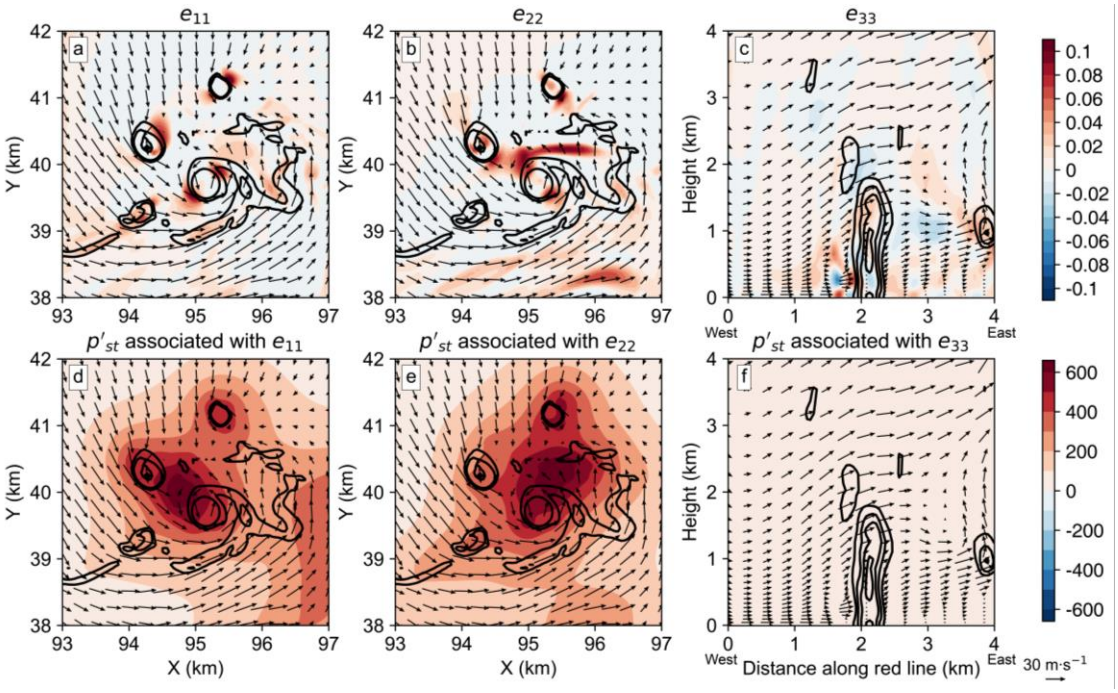

Fig. 13. At 0704, the horizontal cross-sections of (a) e_{11} (shaded, s^{-1}), (b) e_{22} (shaded, s^{-1}), (d) p'_{st} associated with e_{11}(shaded, Pa), and (e) p'_{st} associated with e_{22} (shaded, Pa) at ~26 m AGL, overlaid with wind vectors and vertical vorticity (contours at 0.05, 0.15 s^{-1}). The vertical cross-sections of (c) e_{33} (shaded, s^{-1}) and (f) p'_{st} associated with e_{33} (shaded, Pa) along the red line from west to east in Fig. 4d, overlaid with wind vectors and vertical vorticity (contours at 0.1, 0.2, 0.3 s^{-1}).

The shearing deformation describes the rate of change of velocity along axes that are not aligned with the coordinate axes, leading to fluid shape change. According to Eq. (7), the shearing deformation has three components: changes in shape caused by velocity gradients between pairs of axes across the *y*-*z* plane (e_{23}; Fig. 14a), across *x*-*y* plane (e_{13}; Fig. 14b), and across x-y plane (e_{12}; Fig. 14c), respectively. In the three components, large shearing deformation is generated as the flow approaches the tornado and changes its direction quickly (Fig. 14a–c). The dominant term of shearing deformation is e_{12} while e_{23} and e_{13} are much smaller. Therefore, the p'_{st} associated with e_{12} (Fig. 14f) is much greater than those associated with e_{23} and e_{13} (Fig. 14d and e). In other words, the large

p'_{st} is primarily associated with changes in shape caused by velocity gradients between pairs of axes across the horizontal plane near the surface, rather than across the vertical planes passing through the tornado center. Due to the strongly rotating flow of the tornado, a large amount of airflow will not only produce convergence and divergence at the periphery of the tornado, but also produce strong wind shear, resulting in intense shearing deformation. Therefore, the horizontal shearing deformation (e_{12}; Fig. 14c) is found to be strongest at the periphery of the tornado rather than at its center, similar to the horizontal distribution of convergence/divergence (cf. Fig. 13a and b), creating a large positive pressure perturbation there.

In summary, as the near-surface vortex intensifies and the maximum vorticity is near the surface at 0704, the convergence/divergence and wind shear, especially those associated with horizontal wind components, increase dramatically near the tornado and the corner region. This leads to a much larger flow deformation that directly contributes to the splat term, resulting in a large, positive dynamic perturbation pressure that is responsible for the positive upward DVPPGF near the ground.

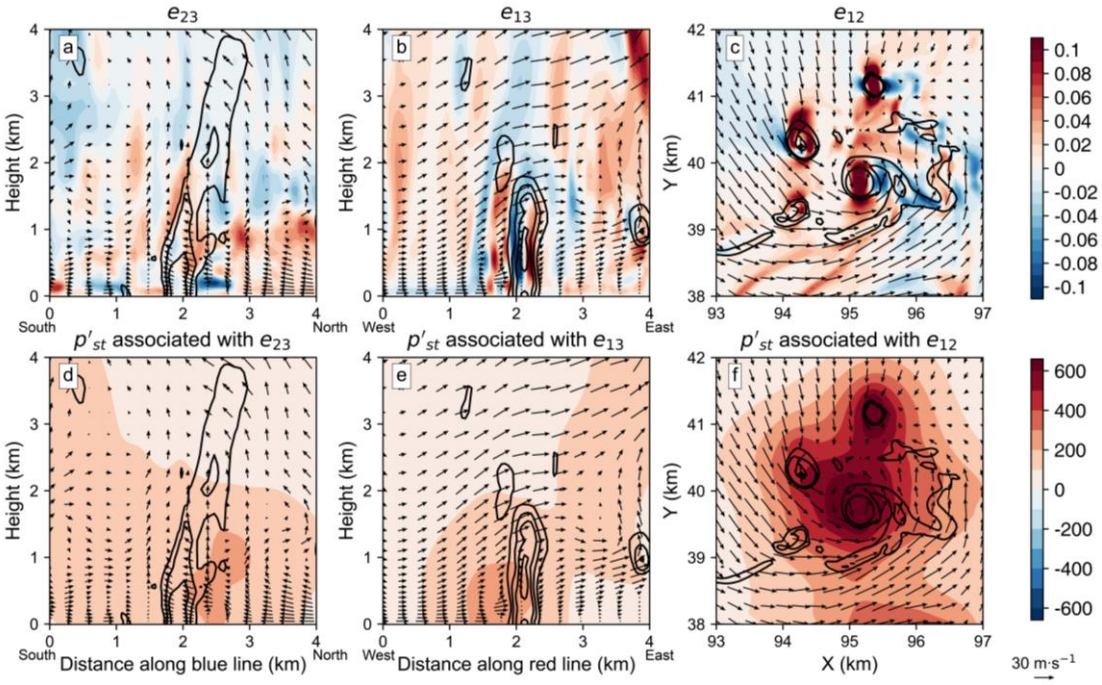

Fig. 14. At 0704, vertical cross sections of (a) e_{23} (shaded, s^{-1}) and (d) p'_{st} associated with e_{23} (shaded, Pa) along the blue line in Fig. 4d from south to north. The vertical cross-sections of (b) e_{13} (shaded, s^{-1}) and (e) p'_{st} associated with e_{13} (shaded, Pa) along the red line from west to east in Fig. 4d. The horizontal cross-sections of (c) e_{12} (shaded, s^{-1}) and (f) p'_{st} associated with e_{12} (shaded, Pa) at ~26 m AGL. All panels are overlaid with vertical vorticity (contours: 0.1, 0.2, 0.3

826 s^{-1} for panels a, b, d and e; 0.05, 0.15 s^{-1} for panels c and f) and wind filed (vectors,
827 m s^{-1}).
828

829 ## 6. Trajectory analysis of vertical momentum forcing leading to tornado
830 ## vortex intensification

831 The earlier analyses are in the Eulerian framework; they show the spatial distributions
832 of different force components at particular times but do not directly show how the different
833 force components act on the air parcels that swirl around and converge toward the vortex
834 center and rise off the ground. This is better revealed by Lagrangian trajectory-based force
835 and budget analyses in this section.

836 We initialize a large number of trajectories at ~ 26 m AGL at 0702 and 0703, shortly
837 before tornadogenesis. Trajectories are launched from every grid point within the 4.6 km ×
838 3.1 km (see Fig. 15 for trajectories initialized at 0702) and 3.0 km × 2.7 km boxes (figure
839 not shown), respectively. The parcels are selected to cover both the primary tornado vortex
840 and the surrounding small vortices. At 0703, the tornado vortex region occupies a smaller
841 area than at 0702 due to convergence. A total of 5859 and 3355 trajectories are initialized
842 at 0702 and 0703, respectively. The time step for trajectory integration is 1 second.
843 Influenced by the strong swirling convergent flow, most parcels revolve counterclockwise
844 around the developing tornado, and many are eventually drawn into the vortex over time.
845 Some parcels are initially drawn into those small vortices surrounding the central vortex
846 (Fig. 15b–e), and are ultimately entrained into the main vortex together with the small
847 vortices as they merge into the main vortex by 0706:00 (Fig. 15f).

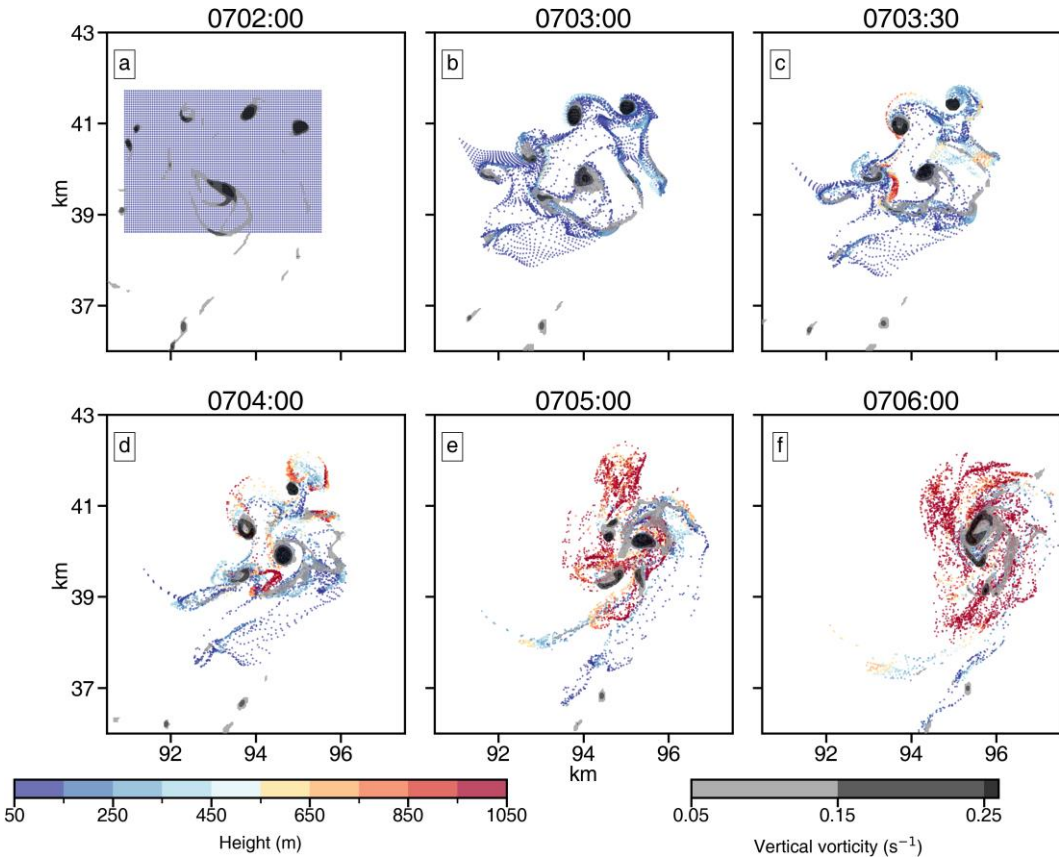

Fig. 15. Vertical vorticity at 26 m AGL (gray shading; s^{-1}) at (a) 0702:00, (b) 0703:00, (c) 0703:30, (d) 0704:00, (e) 0705:00, and (f) 07:06:00 and the positions of the trajectory parcels at the corresponding times (scatters). The color of scatters indicates the height of parcels (m). Panel (a) shows the initial trajectory locations defined on the regular model grid points.

To determine which forcing terms cause the parcels entering the tornado vortex to accelerate vertically and rise rapidly off the ground, we integrate individual terms on the RHS of the vertical momentum equation (2) along the parcel trajectories. The accuracy of the trajectory-based calculations is first checked using the criterion proposed by Peters et al. (2019), and we will only examine "accurate" trajectories. The trajectories are considered accurate if $|[\max(w_{traj}) - \max(w_{integ})]/[\max(w_{traj}) - \max(w_{traj,0})]| < 0.1$, where w_{traj} and $w_{traj,0}$ are the vertical velocities interpolated from the Eulerian grid to the trajectory at time t and at initial time, respectively, and w_{integ} is the result of time integration of Eq. (2) to time t. The max( ) function takes the maximum w along the trajectory throughout the time integration. This ensures that the relative error in max(w) calculated using Eq. (2) remains below 10%. A total of 1222 and 896 trajectories, initialized at 0702 and 0703, respectively, are found to meet this criterion. Among the accurate

trajectories, we choose one representative[1] trajectory for each of the initiation times (parcels A and B in the left and right panels of Fig. 16, and integrate the RHS vertical momentum forcing terms along the trajectories to see how they cause *w* to change (Fig. 17 and Fig. 18). Note that the curves shown in Fig. 17 and Fig. 18 are the integrated (accumulated) changes in *w*, therefore vertical acceleration due to the forcing terms is represented by slope of the curves shown.

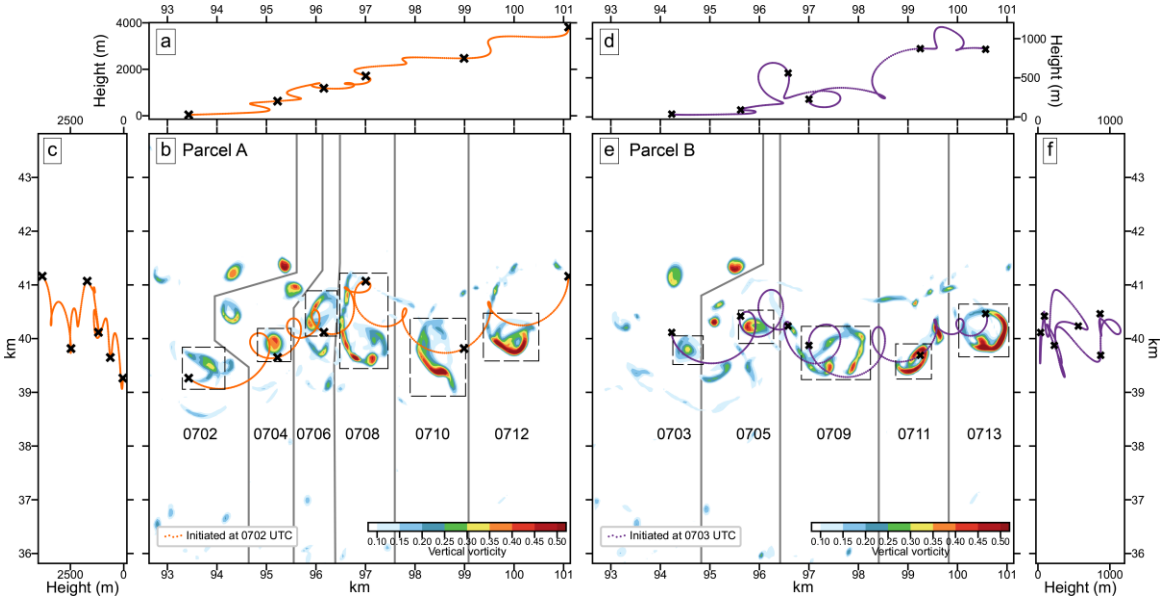

Fig. 16. The swaths of maximum vertical vorticity (shaded; s^{-1}) at ~26 m AGL are shown every 120 s (b) from 0702 to 0712 for representative parcel A and (e) from 0703 to 0713 for representative parcel B. For clarity, the vertical vorticity at 0707 is omitted in (e) due to partial overlap with that at 0705. The trajectories of two parcels tracked forward for 10 minutes are overlaid on the maximum vertical vorticity. The crosses on the trajectories indicate the positions of the parcel every 120 s. The trajectories are projected onto the side walls in panels (a), (c), (d), and (f). Grey lines try to separate the vorticity features at different times. The positions of maximum vertical vorticity at each time are enclosed within black dashed rectangles.

We first discuss the trajectory of parcel A and the associated *w* momentum forcing terms. Overall, the parcel moves eastward along with the tornado vortex and then tornado from 0702:00 to 0712:00 in a spiraling path, leaving a cycloidal track projected to the ground (Fig. 16b). In the vertical direction, the parcel also rises in a spiraling pattern (Fig.

[1] Note that the term 'representative parcel' refers to a similar dominant forcing along the trajectory compared to many parcels that enter the tornado vortex or tornado, even though the final heights to which the parcels rise may differ.

16a and c). Based on the dominant forcing that causes vertical acceleration, the trajectory evolution can be divided into two stages. From 0702:00 to 0703:00, as parcel A approaches the developing tornado, it rises slowly (see green curve in Fig. 17b and c). Once it is drawn into the tornado vortex at around 0703:00 (figure not shown), the parcel rises rapidly due to enhanced DVPPGF (indicated by the larger positive slope of the blue curve in Fig. 17c). The rapidly increasing upward DVPPGF, which remains positive until 0703:20, provides strong upward forcing, causing the parcel to rise quickly from 200 to ~480 m AGL between 0703:00 to 0703:20 (green curve in Fig. 17c).

Before 0703:15, the positive DVPPGF primarily comes from the positive spin term SNVPPGF (slope of orange curve in Fig. 17c) in the presence of a strong low-level tornado cyclone. After ~0703:15, the slope of the orange curve (SNVPPGF) turns negative, and the splat term (STVPPGF, slope of yellow curve in Fig. 17c) increases dramatically after 0703:10, providing the necessary positive dynamic forcing for rapid upward acceleration. Even with the large positive STVPPGF contribution, the total DVPPGF dynamic forcing turns negative after ~0703:20 (negative slope of blue curve in Fig. 17c) when the parcel rises to about 360 m AGL. As a result, *w* of the air parcel goes through a short period of deacceleration while the parcel rises more slowly (Fig. 17c). Later on, DVPPGF oscillates between positive and negative values but is mostly negative (the blue curve in Fig. 17b has an overall negative trend) as the parcel continues to rise to above 3 km AGL (Fig. 17b). Between 0703:30 and 0712:00, the splat and spin terms (STVPPGF and SNVPPGF) are of opposite signs and similar magnitudes, and their sum yields a generally negative DVPPGF that oscillates in time. Note the different vertical scales used by the spin/splat terms and the total forcing term in Fig. 17b. The oscillations in the blue curve, therefore, the periodic sign changes in DVPPGF are apparently due to the axis-asymmetric patterns of the spin and splat terms, as shown in Section 4. As the parcel spirals around the vortex center, it experiences variations in the magnitude of the spin and splat terms.

The buoyancy (EB) becomes the primarily driving force for the continued rise of the parcel after 0703:20. The slope of the red curve is slightly positive from 0702:45 and the slope becomes steeper after 0703:20 (Fig. 17c) when the relative humidity of the parcel increases significantly (cyan curve in Fig. 17a). The parcel reaches the lifting condensation level (LCL) at about 900 m at 0704:30, with relative humidity being close to 100%. The slope of red curve becomes persistently positive and large after 0705:30, providing steady positive buoyancy forcing to the parcel (Fig. 17b). The accumulative contribution of EB to

the vertical acceleration causes w to reach above 40 m s^{-1} and the parcel rises to nearly 4 km AGL by 0712:00. Clearly, as the parcel leaves the ground to reach ~360 m, it is the buoyancy force that supports the continued rise of the parcel within the tornado, allowing it to enter the mesocyclone and the strong updraft above.

During the entire period, the parcel gains its positive vertical vorticity ζ mostly before 0704:00, when ζ increases from 0.1 to 0.35 s^{-1} (Fig. 17a), corresponding to the rapid rise of the parcel from near the surface to ~700 m AGL. The increase in ζ is most rapid between 0703:00 and 0703:30 (Fig. 17a), when the total dynamic forcing is large and positive, and the parcel rises from ~175 m to ~475 m AGL (Fig. 17c), corresponding to rapid stretching of the air column above ground and therefore vortex intensification. After 0704:00, the ζ of the air parcel ceases to increase persistently, oscillating between 0.2 to 0.35 s^{-1}. This suggests that the vertical acceleration and the corresponding stretching are much reduced after the parcel goes through the rapid acceleration phase very close to the ground, which is consistent with the similar magnitudes of the positive EB and negative DVPPGF terms. In fact, w goes through cycles of acceleration and deceleration as the parcel spirals upward, while maintaining positive values at almost all times (Fig. 17b).

To summarize, during a couple of minutes when air parcel A approaches the center of the developing tornado, it rises slowly, experiencing a small positive upward dynamic PGF, and an even smaller negative buoyancy. As the parcel gets closer to the tornado vortex center, the dynamic PGF increases, and the dynamic forcing is associated with the spin term in the presence of a low-level tornado cyclone. The larger dynamic PGF causes the air parcel to rise more rapidly, and the corresponding stretching rapidly intensifies the vertical vorticity mostly rapidly within about 30 seconds. As this happens, tornadogenesis occurs (at around 0703:20), the dynamic PGF due to the spin term reverses sign and becomes negative (when the parcel is below 400 m AGL), because the maximum vertical vorticity is now at the ground. Shortly before this, the dynamic PGF due to the splat term at the location of the parcel turns positive and becomes large, maintaining a positive total dynamic PGF as the parcel goes through its last phase of tornadogenesis. Afterwards, when the parcel rises above 350 m, the total dynamic PGF turns negative, and the buoyancy term takes over to become the primary driving force to the rising parcel and updraft, overcoming the negative dynamic PGF. Therefore, the dynamic PGF due to the spin term, the dynamic PGF due to the splat term, and then buoyancy take turns to provide the primary positive upward forcing for vertical acceleration and the associated crucial vorticity stretching.

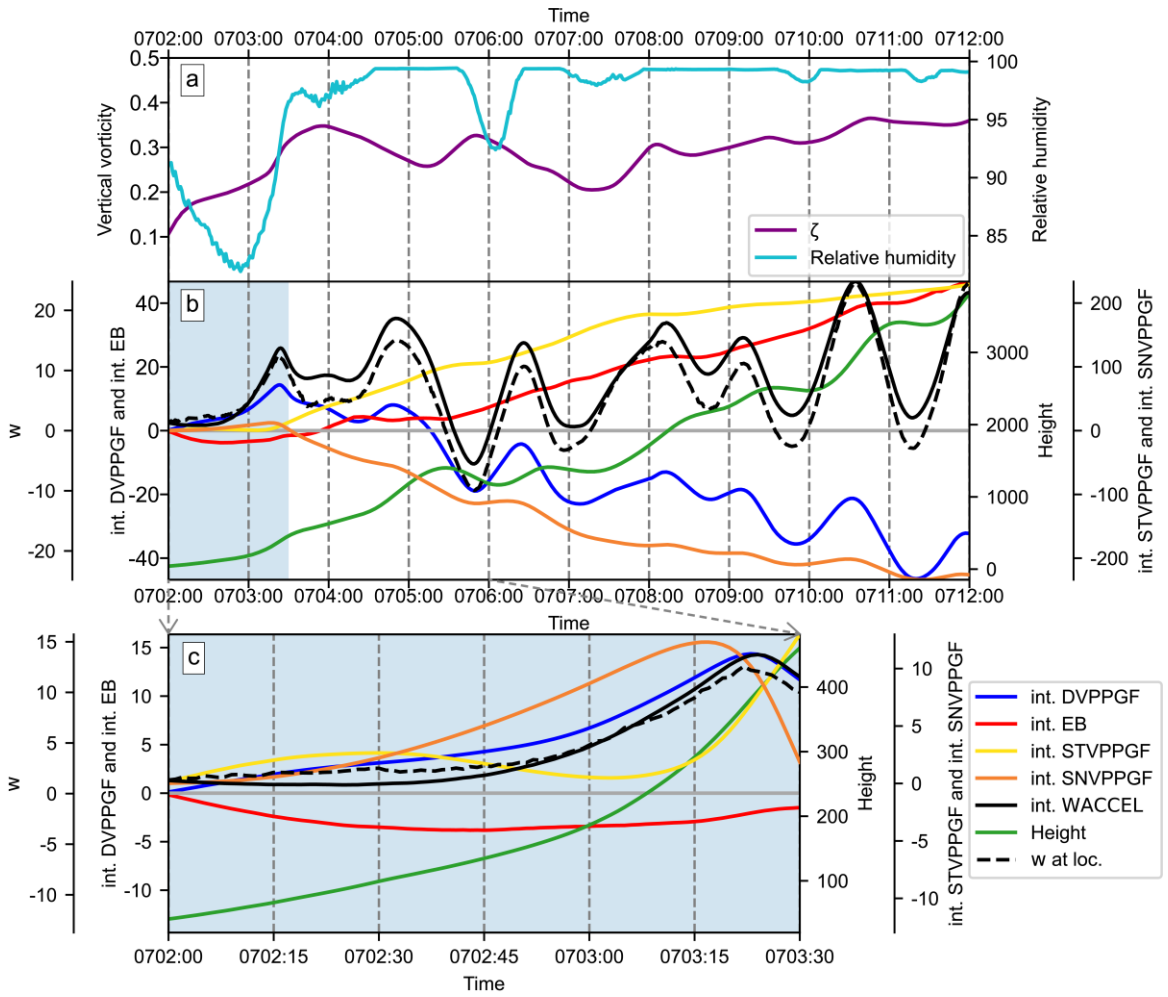

Fig. 17. Vertical velocity budgets along the trajectory of parcel A initiated at 0702:00 and tracked forward to 0712:00 (panel b). The solid black curve is the vertical velocity *w* obtained by integrating the RHS terms of the vertical momentum equation along the trajectory using the leftmost vertical axis. The integrated changes in *w* due to individual forcing terms are also drawn, including that due to the DVPPGF term (blue curve) and EB term (red curve) using the second vertical axis from the left. The integrated *w* changes due to splat term STVPPGF (yellow curve) and spin term SNVPPGF (orange curve) use the rightmost vertical axis. The dashed black curve represents the *w* interpolated from the model grid to the parcel locations. The green curve is the parcel height (m AGL) using the second vertical axis from the right. The bottom panel (c) is a zoomed-in plot from 0702:00 to 0703:30. Vertical vorticity ζ (purple curve) and relative humidity (cyan curve) along the trajectory are shown in panel (a).

Now we examine the trajectory of parcel B, shown in the right panels of Fig. 16. Parcel B is one of those initiated at 0703:00. Parcel A approaches the developing tornado center before tornadogenesis actually occurs (at 0703:20 when the largest vertical vorticity develops near the surface), and the rapid vertical acceleration of parcel A and the rapid increase in its vertical vorticity roughly coincide with the time of tornadogenesis. A key

975 difference of parcel B from parcel A is that it enters the tornado after tornadogenesis has
976 occurred.

977 Specifically, parcel B takes some time to be drawn into the tornado. From 0703:00 to
978 0704:30, the parcel spirals around the south side of the tornado (see right panels of Fig. 16).
979 In the vertical direction, it rises very slowly and is at ~60 m AGL at 0704:30 (green curve
980 in Fig. 18c). The vertical vorticity also increases only very slightly during the period (Fig.
981 18a). Between 0704:30 and 0706:00, the parcel rises more rapidly to ~200 m AGL (Fig.
982 18c), and the vertical vorticity increases from ~0.025 to 0.13 s^{-1} (Fig. 18a). During the
983 period, the dynamic forcing due to the spin term (SNVPPGF), is generally negative (slope
984 of orange curve in Fig. 18c), while the dynamic forcing due to the splat term (STVPPGF),
985 is generally positive (slope of yellow curve in Fig. 18c). The sum of SNVPPGF and
986 STVPPGF, approximately equal to the total dynamic forcing (DVPPGF), is mostly positive
987 (slope of blue curve in Fig. 18c). The positive DVPPGF, together with the effective
988 buoyancy (EB) term that turns positive at ~0705:15 (slope of red curve in Fig. 18c), both
989 support positive *w*. The persistent positive *w* produces enough vertical stretching near the
990 ground which leads to the significant increase in vertical vorticity noted above. During the
991 period when parcel B approaches the tornado center, the signs of SNVPPGF and SNVPPGF
992 are opposite to those of parcel A when parcel A is similarly approaching the tornado center
993 close to the ground (see Fig. 17c). This is because at this time, tornadogenesis has already
994 occurred. Strong negative dynamic PGF associated with strong near-surface rotation forms
995 near the tornado center.

996 Parcel B enters the tornado at around 0705:45. After 0706:00, the positive slope of the
997 integrated STVPPGF becomes steeper especially after 0706:10 (yellow curve in Fig. 18c),
998 while the slope of integrated SNVPPGF briefly becomes slightly positive before turning
999 steeply negative after 0706:15 (orange curve in Fig. 18c). Between 0706:00 and 0706:20,
1000 the sum of integrated STVPPGF and SNVPPGF, or the integrated DVPPGF, gains a large
1001 positive slope (blue curve in Fig. 18c). Meanwhile, the positive effective buoyancy (EB)
1002 also becomes larger (red curve in Fig. 18c). Subject to positive DVPPGF and EB, *w*
1003 increases rapidly (black curve in Fig. 18c), and the parcel rises from ~200 m to close to 600
1004 m by 0706:30 (green curve in Fig. 18c). After 0706:30, the parcel follows spiraling
1005 trajectories, with its height going up and down (see right panels of Fig. 16), with the total
1006 dynamic forcing oscillating between positive and negative values (blue curve in Fig. 18b).
1007 Similar to the case of parcel A, the oscillations in the dynamic forcing components are

clearly related to the axis-asymmetry of tornado. In fact, by 0711:00, the near-surface vertical vorticity has developed an asymmetric vortex ring pattern, which organizes into a more circular ring by 0713:00 (Fig. 16e). The tornado has evolved from a one-cell structure with maximum vertical vorticity located at its center, to a two-cell structure with a vortex ring. Later on, multiple subvortices develop along the vortex ring due to barotropic instability, as investigated by Huang and Xue (2023).

The contribution of buoyancy forcing EB is weakly positive or negative from 0703 to 0705:15 (red curve of Fig. 18c). EB becomes more positive at 0705:15 and increases significantly after 0705:10, especially as parcel B reaches its LCL at about 0706:20 (cyan curve in Fig. 18a). The sign of EB remains steadily positive and large through 0713:00, offsetting most of the negative effect of dynamic PGF during the period. Still, the oscillations in the dynamic forcing, characterized with an up-and-down trajectory path, causes a much slower rise of the parcel after it enters the tornado, and a slower increase in its vertical vorticity than the case of parcel A. By 0712:00, the parcel is still at about 1 km AGL and its vertical vorticity is at about 0.3 s^{-1} (Fig. 18).

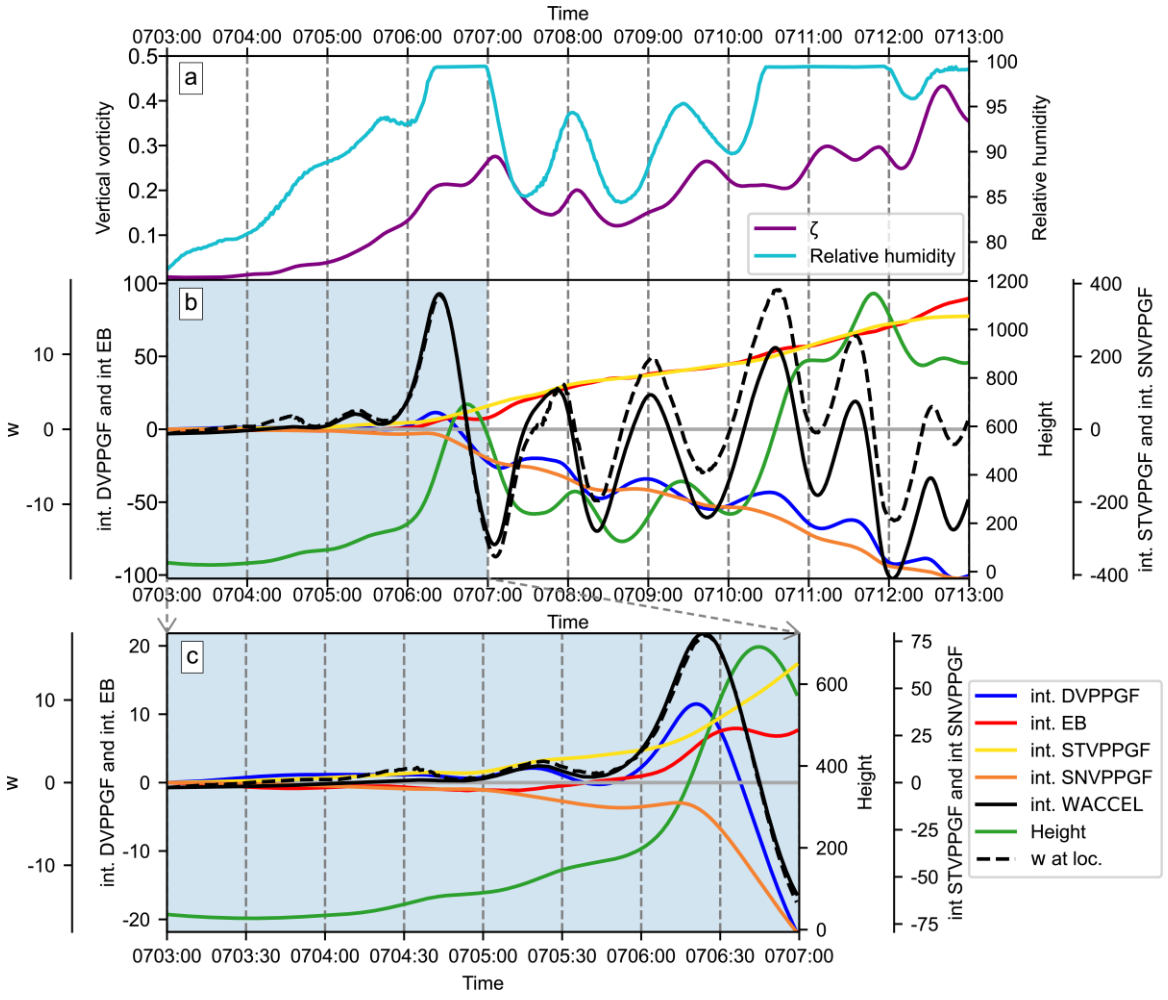

Fig. 18. Same as Fig. 17, but for a representative trajectory initialized at 0703:00 that is tracked forward to 0713:00.

In summary, the similarity between parcels A and B lies in that positive dynamic vertical PGF is the dominant forcing for low-level near-ground upward lifting that takes the air parcels off the ground. Strong upward acceleration near the ground and the resulting vertical stretching cause the intensification of vertical vorticity that either leads to tornadogenesis or maintains the established tornado. Shortly before reaching their LCL, positive buoyancy becomes the primary and essential driving force for accelerating the air parcels to higher altitudes. The switching over of the dominant term from dynamic to buoyancy forcing is also noted in Yokota et al. (2018).

The main difference between the two air parcels lies in the contributions of the spin and splat terms to the total vertical dynamic PGF before and after the parcel enters the tornado vortex and the developed tornado near ground. Parcel A enters the vortex near ground almost exactly when tornadogenesis occurs. Before tornadogenesis, the DVPPGF due to the spin term is still positive and upward. Once tornadogenesis occurs, the dynamic vertical PGF due to the spin term becomes significantly negative within and near the vortex. Therefore, positive total vertical dynamic PGF has to count on a large positive contribution from the splat term. For these reasons, parcel A first experiences strong upward DVPPGF due to the spin term and small downward DVPPGF due to the splat term on its way towards the vortex center. It is clear that the spin term is responsible for rapid lifting the air parcel off the ground, which enhances low-level convergence as additional parcels are drawn into the developing tornado. The strong convergence with the associated vertical stretching near the surface facilitates tornadogenesis. Right after the tornadogenesis occurs, the two forces change sign so that the force due to the splat term becomes the positive driving force. While for parcel B, since the largest vorticity is already located at the ground when it enters the tornado, the DVPPGF due to the spin term is mostly negative, whereas that due to the splat term is always positive. This highlights the importance of the splat term and the associated deformation flows in keeping strong horizontal convergence and vertical updrafts (or the corner flow jet) during the mature stage of the tornado. The important role of the splat term has not been well recognized in previous studies.

In addition to the representative trajectories, we also calculate the averages and associated diagnostics of the trajectories initialized at 0702 and 0703 and integrated through

0712 and 0713, respectively (Fig. 19 and Fig. 20). Similar to the representative trajectories (cf. Fig. 17c and Fig. 18c), the dominant term for low-level vertical acceleration (black curves in Fig. 19c and Fig. 20c) and consequently the increase in vertical vorticity (purple curves in Fig. 19a and Fig. 20a), is the dynamic forcing (blue curves in Fig. 19c and Fig. 20c). The dominant term in dynamic forcing in the average trajectories is also similar. For the average trajectory initialized at 0702, in which parcels enter the tornado vortex before tornadogenesis, the parcels first experience upward DVPPGF due to the spin term prior to 0702:35 (orange curve in Fig. 19c). For the average trajectory initialized at 0703:00, in which most parcels enter the tornado core after tornadogenesis, the DVPPGF due to the spin term is mostly negative (orange curve in Fig. 20c), whereas that due to the splat term is always positive (yellow curve in Fig. 20c). As the parcels reach their respective LCLs, with relative humidity approaching 100% (cyan lines in Fig. 19a and Fig. 20a), the buoyancy forcing becomes persistently positive and contributes significantly to continued ascent (red curves in Fig. 19c and Fig. 20c).

Due to the asymmetry of the surface tornado vortex and the associated spin term (cf. Fig. 6n and o), the timing of the transition of the spin term from negative to positive differs somewhat among the trajectories. For the average trajectory initialized at 0702, the transition occurs at approximately 0702:40 (orange curve in Fig. 19c), which is earlier than the tornadogenesis time of 0703:20. The slightly positive value of the splat term in the average trajectory before 0702:40 (yellow curve in Fig. 19c), in contrast to the negative value in the representative trajectory (yellow curve in Fig. 17c) for parcels initialized at 0702, may also be explained by differences among individual trajectories. For parcels initially located on the east side of tornado, the splat term is already positive by 0703 (cf. Fig. 6u).

Due to the smoothing effect of the averaging, the magnitudes of the forcing terms are much smaller in the average trajectories (Fig. 19c and Fig. 20c) than in the representative trajectories (Fig. 17c and Fig. 18c). In addition to the smoothing effect, the smaller spin term in the average trajectory initialized at 0702:00 (orange curve in Fig. 19c) compared to the representative trajectory (orange curve in Fig. 17c) may also be partly due to discrepancies between the interpolated and integrated vertical velocities (dashed vs. solid black curves in Fig. 19c). This explanation is supported by the similar magnitudes of the splat term between two average trajectories (yellow curves in Fig. 19 and Fig. 20c). Although using the criterion proposed by Peters et al. (2019) can limit the discrepancies

between the interpolated and integrated vertical velocities, it primarily constrains the maximum *w* along the trajectory to within 10%, and is less effective at controlling errors during the early stages of integration. This limitation is particularly significant near the surface, where the vertical vorticity field is complex, with six small vortices rotating around the tornado vortex (cf. Fig. 1).

In summary, despite some differences between the representative and average trajectories, the key findings are consistent. The dynamic forcing is primarily responsible for rapidly lifting parcels off the ground and enhancing low-level convergence to intensify the tornado vortex and maintain the tornado. The spin term contributes positively to dynamic forcing before tornadogenesis and negatively afterward. The splat term becomes the dominant positive contribution to dynamic forcing after tornadogenesis. As the parcels rise to heights near their LCLs, buoyancy forcing becomes the main driver for continued ascent to upper levels, while the dynamic forcing turns negative.

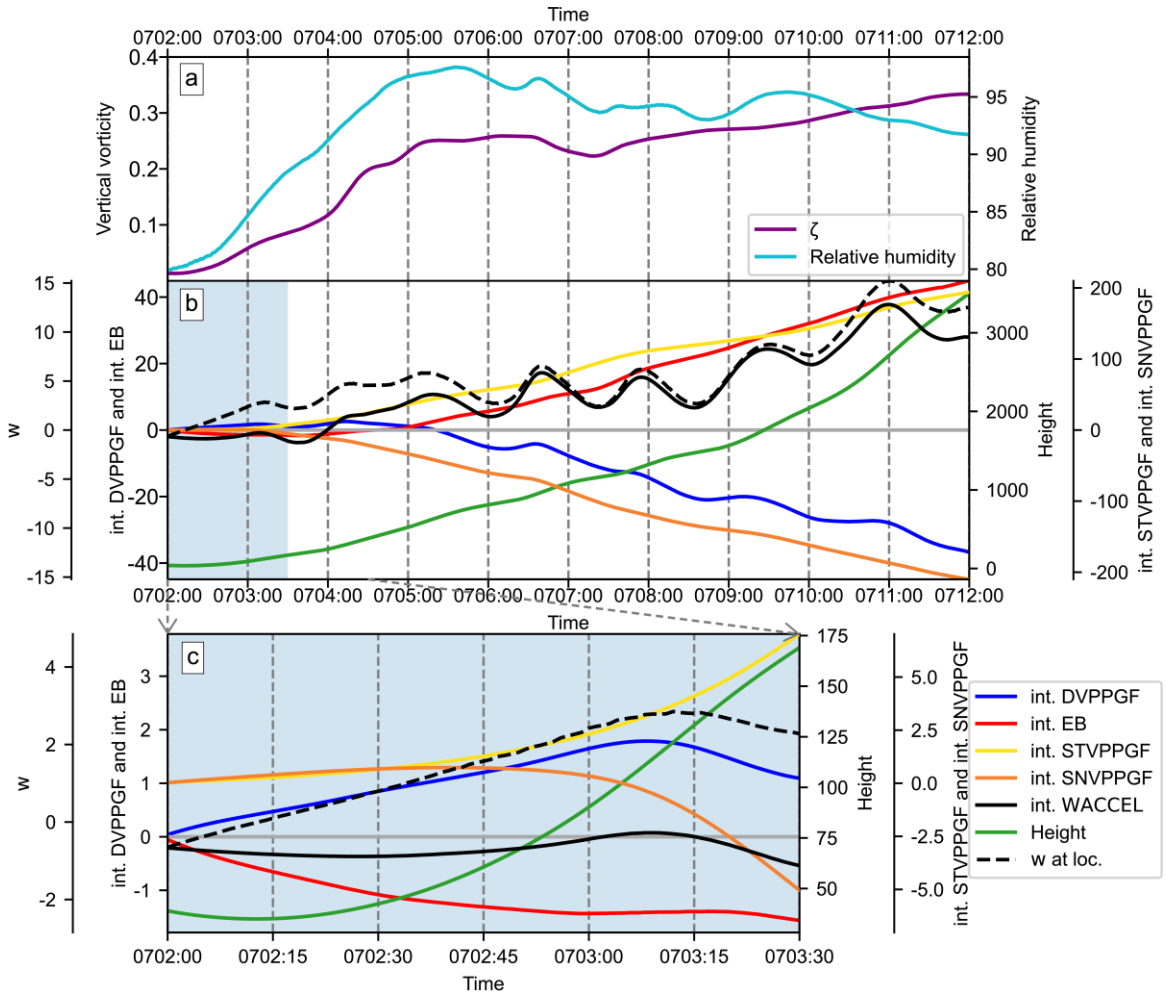

Fig. 19 Same as Fig. 17, but for the average trajectory initialized at 0702:00 that is tracked forward to 0712:00.

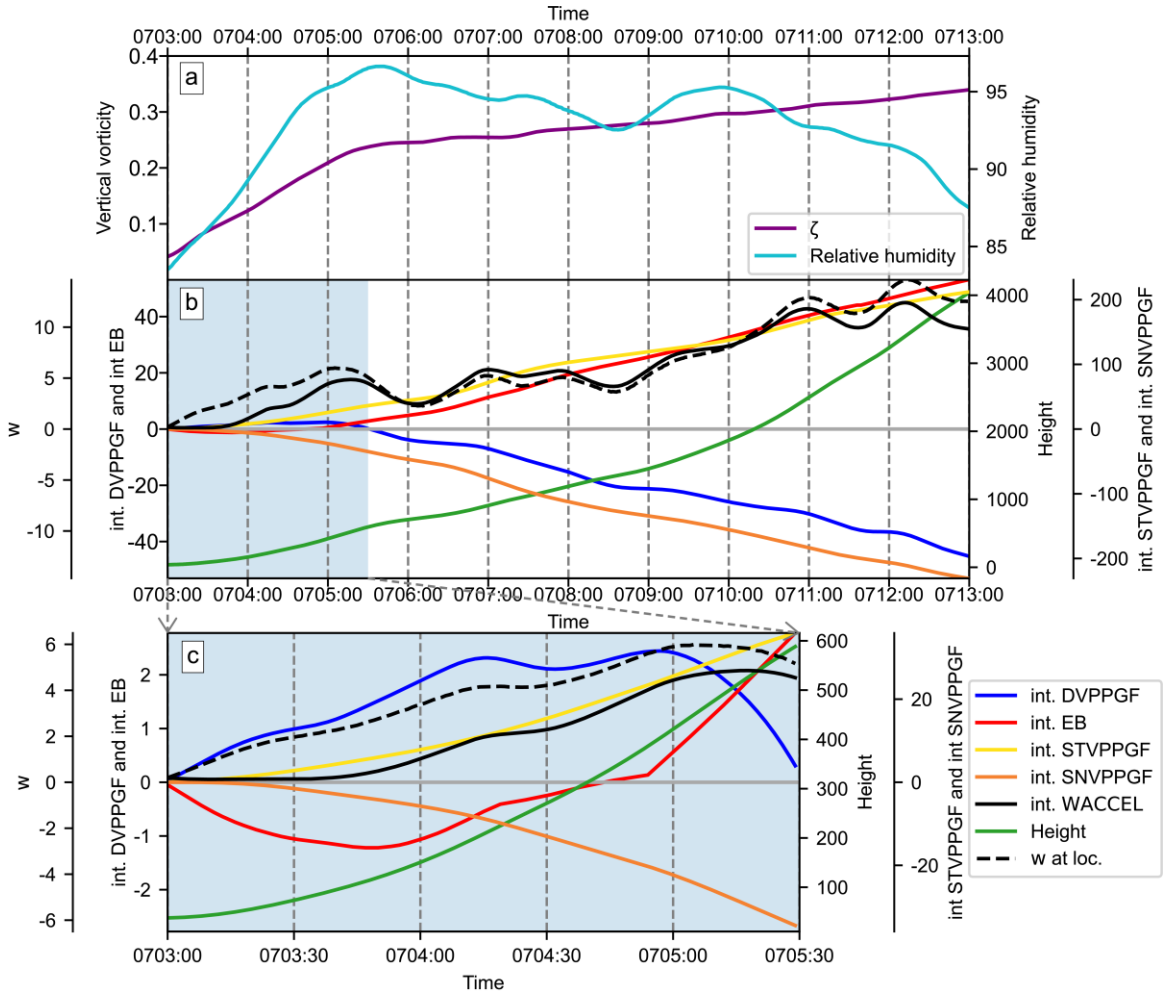

Fig. 20 Same as Fig. 17, but for the average trajectory initialized at 0703:00 that is tracked forward to 0713:00.

7. Summary and discussions

A successful numerical simulation of an EF4 supercell tornado of Funing, China, on 23 June 2016 is analyzed to understand the forcing mechanisms for the vertical acceleration that leads to tornado vortex intensification and tornado maintenance. Within the simulation, the tornado vortex intensifies dramatically from 0700 to 0704 UTC to form a tornado. In the initial stage of tornado vortex intensification, the maximum vertical vorticity ζ associated with the tornado cyclone embedded within the mesocyclone is located at about 2.25 km AGL. With time, the height of the tornado cyclone lowers, and the surface vortex intensifies and extends upward. As the tornado cyclone and surface vortex connect, a coherent tornado column forms, signifying tornadogenesis. Shortly before the tornado vortex intensification, six small vortices develop along the occluded gust front on the north

side of the vortex, and are drawn into the vortex by spiraling convergent flow. In terms of time series, an increase in near-surface maximum vertical acceleration leads to an increase in maximum ζ there, indicating the direct role of vertical acceleration and associated stretching in tornado vortex intensification at the ground. The important role of low-level vertical acceleration in tornadogenesis has also been pointed out by previous studies (e.g., Coffer and Parker 2017).

Examining the forcing terms within the vertical momentum equation in an Eulerian framework first, we found that the dynamic forcing is the dominant term for vertical acceleration near the ground. We decompose further the dynamic forcing on the right-hand side of the diagnostic perturbation pressure equation into the spin and splat terms, which are primarily associated with vertical vorticity and horizontal flow deformation, respectively (with contributions from other vorticity and deformation components being much smaller). Before the tornado forms, the maximum vorticity is associated with the tornado cyclone, which is located a couple of kilometers AGL (see conceptual model in Fig. 21). The tornado cyclone and the corresponding negative perturbation pressure create upward dynamic PGF underneath it that is associated with the spin term. Positive perturbation pressure associated with the splat term is weak and off ground at this stage, resulting in a weakly negative total dynamic PGF at this time. Afterwards, increased upward dynamic PGF associated with the further lowering of the tornado cyclone accelerates the updraft and stretches near-surface vertical vorticity to reach tornado intensity. Once a tornado forms, the maximum vorticity is located very near the ground (Fig. 21b). The enhanced surface vorticity, associated with the spin term in the diagnostic pressure equation, corresponds to stronger negative pressure perturbations at the surface compared to aloft. This results in a downward dynamic PGF that would weaken vertical stretching. To maintain strong stretching and prevent tornado dissipation, additional upward forcing is needed. This upward dynamic forcing is provided by the splat term, which is associated with near-surface deformation flow.

The deformation near the tornado vortex becomes larger as the tornado vortex intensifies and more air rapidly converges into the tornado center in response to the enhanced updrafts and decreased pressure. Subject to mass continuity and increased centrifugal force, the radial flow converging towards the tornado vortex center has to stop at a certain radius and then flow upward, since the radial wind must vanish before reaching the vortex center. This results in strong deformation near the edge of the vortex, in the form

of strong horizontal convergence/divergence and flow shearing. The increased deformation associated with the splat term sets up a large positive perturbation pressure near the surface (off the vortex center) and therefore upward dynamic PGF that overcomes the negative dynamic PGF associated with the spin term (Fig. 21b). Net positive dynamic PGF therefore develops near ground to promote continued updraft acceleration and stretching. The contribution of effective buoyancy is much smaller than the dynamic forcing near the ground, below the LCL at least. The results of contributions of temperature, perturbation pressure, and hydrometeor loading to the effective buoyancy, show that the first two terms are found to be the main contributors, although the results are not shown.

Trajectory-based Lagrangian analyses provide an additional perspective on the vertical momentum forcing for air parcels entering the tornado vortex or tornado. Parcel trajectories are initialized in the vicinity of the developing tornado at the lowest model level. The dynamic upward PGF is the main driving force for the vertical acceleration of the parcels entering the tornado vortex, while buoyancy becomes the dominant contributor after the air parcels are lifted off the ground.

The dominant component in the dynamic PGF depends on the time at which the parcel enters the tornado vortex and the entering time relative to tornadogenesis. Positive upward dynamic PGF near the low-level tornado vortex is mainly attributed to the spin term if the parcel enters the tornado vortex before tornadogenesis; it is, however, attributed to the splat term if the parcel enters the tornado after tornadogenesis. This transition in the dominant term in dynamic forcing matches the results of Eulerian analyses summarized above. It is important to note that, although the spin term becomes negative after tornadogenesis, the role of the mesocyclone is still important. The mesocyclone now acts as a background structure in which the tornado is embedded, promoting a broader region of strong updraft and correspondingly strong low-level convergence. The mesocyclone supports the overall convergence and merging of smaller vortices or horizontal vorticity within the airstream into the main vortex center.

The relationship between spin and splat terms can be considered a “tug-of-war”. For the primary air parcels feeding the near-surface updraft within the tornado, once the downward acceleration induced by the spin term surpasses the upward acceleration induced by the splat term, and the positive buoyancy is not enough to overcome the negative total dynamic forcing, the tornado tends to decay. Tornado maintenance needs the positive splat term to offset the negative spin term. In other words, a balance between the spin and splat

terms may be essential for the longevity of a tornado. Understanding why this balance can persist for some tornadoes but fails for others represents a promising area for future research. It should be noted here that because the maximum upward dynamic PGF due to the splat term often does not exactly overlap the minimum downward dynamic PGF due to spin, the magnitude of the former only needs to exceed that of the latter for the rising air parcels, not necessarily right at the center of the vortex where the spin term has the largest effect. When the tornado has a one-cell structure, the strongest near-surface updraft is usually near the tornado center (Rotunno 2013), but when the tornado has a two-cell structure, the downdraft is found at the center of vortex that may or may not reach the ground surface while updraft is usually found near the radius of maximum vorticity or vorticity ring, somewhat like the eye wall of tropical cyclones (Huang and Xue 2023).

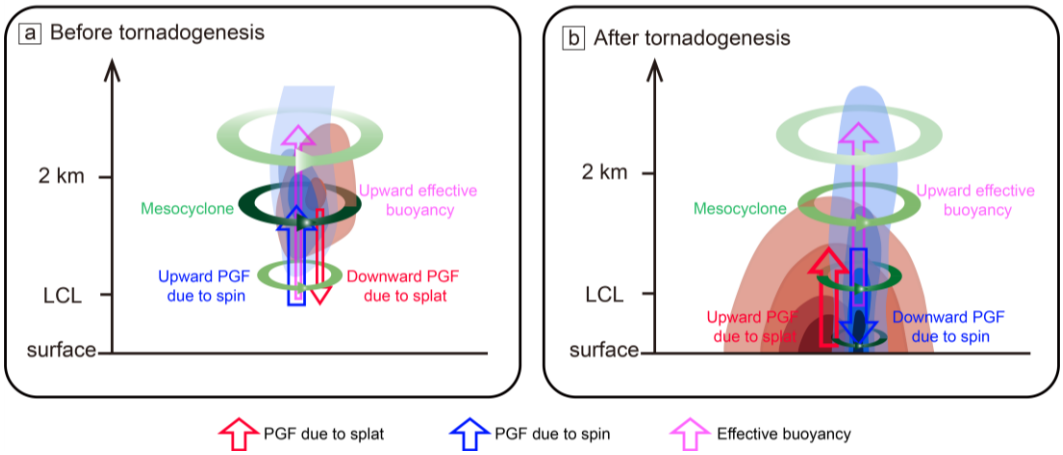

Fig. 21. A conceptual model illustrating the evolution of dynamic and buoyancy forces supporting strong low-level updrafts shortly before and after tornadogenesis within a supercell storm. In the figure, green annuli indicate the counterclockwise circulation and associated vertical vorticity, with the color gradient from light to dark representing circulation strength from weak to strong. Blue and red isosurfaces represent respectively, the negative/positive perturbation pressure from the spin/splat terms in the pressure diagnostic equation. The pressure gradient force (PGF) induced by spin, splat, and the effective buoyancy are denoted by blue, red, and magenta vertical arrows, respectively, and the width of the arrows indicate the strength of the forces. (a) Shortly before tornadogenesis, the vorticity associated with the mesocyclone is larger in magnitude than that at the surface, the dynamic PGF due to rotation or spin term is dominant and points upward, promoting strong low-level upward parcel acceleration and vorticity stretching that can lead to tornadogenesis. The dynamic PGF associated with flow deformation or the splat term is small and downward at this stage, while the buoyancy force is weak and often negative below the parcel LCL, but becomes large and dominant above the air parcels are lifted off the ground to reach LCL. (b) After tornadogenesis, the largest vertical vorticity shifts to the low levels near the ground, so that the spin-induced PGF reverses direction and points downward inside the tornado. At this

time, strong positive upward dynamic PGF is provided by the splat term associated with flow deformation, which is strongest slightly off the tornado center, at a radius where strong convergent horizontal inflow towards the tornado center is deflected by the increasing centrifugal force to the tangential direction. Such strong deformation creates large positive pressure perturbations that set up upward vertical accelerations. The spin and splat terms play a "tug-of-war" game; when the upward PGF due to the splat term wind overcomes the negative PGF associated with spin at the low levels, the tornado can sustain or even intensify, but when the splat term loses to the spin term and the positive buoyancy is not enough to offset the net downward dynamic PGF, downdraft would become dominant in and near the tornado and the tornado will collapse. The buoyancy force at the higher levels is also critical for supporting strong storm updrafts that are instrumental in producing and maintaining the broader low-level convergence into the tornado region. Such convergence ingests essential horizontal and/or vertical vorticity into the tornado vortex region, that is to be (tilted first in the case of horizontal vorticity) stretched into tornado intensity.

The exact role of the splat term in tornado dynamics has not been investigated in detail in the published literature. Most existing studies treat the spin and splat terms as a whole or only provide simplistic explanations or hypotheses on the nature and origin of the dynamic forcing, and often suggest the spin term due to vortex rotation to be the primary factor driving the intensification and maintenance of updrafts (Markowski and Richardson 2014; Peters et al. 2019; Muehr et al. 2024).

The buoyancy forcing is weakly negative during low-level lifting in the current case. However, buoyancy becomes the dominant positive term once parcels shortly before reaching their LCLs, facilitating further acceleration and rising of the parcels to higher altitudes, joining the storm updrafts. At this stage, dynamic forcing often becomes negative. The persistent positive buoyancy acting on the rising parcels allows for substantial accumulated vertical momentum and for typical supercell storms, thermal buoyancy is still the primary driving force for the storm updraft. Without it, a strong mesocyclone cannot form. In a real-case simulation, Yokota et al. (2018) also found that non-linear dynamic forcing is important at lower levels, then buoyancy forcing becomes critical before reaching LCL. Wade and Parker (2021) similarly identified a change in the dominant term from dynamic forcing to buoyancy forcing, but they found the occurrence of this transition at the level of mid-level mesocyclone rather than earlier at the LCL. This difference may arise from their simulations being conducted in a high-shear, low-CAPE environment, while our case has significant CAPE.

According to Bluestein et al. (2014), a vertical resolution of approximately 1–1.5 meters in the corner region of a tornado is likely sufficient to resolve vertical variations in the wind. In our study, ~ 50 m horizontal and vertical grid spacings near ground cannot fully resolve the full structure of the corner flow region, which may quantitatively affect the results of the diagnosed p'_{st} distribution and the corresponding flow patterns. However, given that the simulation does capture convergent low-level flows that abruptly turn upward to form strong updraft cores around central downdraft at the two-cell stage of the tornado (see Fig.8 in Sun 2019), we believe our results are at least qualitatively correct or reasonable.

The findings and conclusions of this study are based on a simulation of a single tornado case. More analyses on tornadoes in additional cases and environments should be carried out to test the robustness of the conclusions. Also, the initial development of the tornado analyzed in this paper involves the merger of a number of smaller vortices, making the tornadogenesis process and the understanding of the dynamic forcing more complex. The tornado also only maintains a one-cell structure for a very short time (Fig. 15). Tornadoes that form through the intensification of a single vortex and maintain a one-cell structure for longer are also worth detailed analyses also. Such would be areas for future studies.

Acknowledgments.

This work was primarily supported by NSFC grant 41730965. Zhenqi Sun is acknowledged for making available his simulation configuration and data.

Data Availability Statement.

The data used in this paper can be found at Harvard Dataverse at https://dataverse.harvard.edu/dataset.xhtml?persistentId=doi%3A10.7910%2FDVN%2FCS1VAN&version=DRAFT.

1283 REFERENCES

1284 Adams, J. C., 1989: mudpack: Multigrid portable fortran software for the efficient solution
1285 of linear elliptic partial differential equations. *Applied Mathematics and*
1286 *Computation*, **34**, 113–146, https://doi.org/10.1016/0096-3003(89)90010-6.

1287 Adrian, R. J., 1982: Comment on '"A note on Poisson's equation for pressure in a turbulent
1288 flow"'. *Phys. Fluids*, **25**, 577, https://doi.org/10.1063/1.863774.

1289 Bluestein, H. B., 2013: *Severe Convective Storms and Tornadoes*. Springer Berlin
1290 Heidelberg, https://doi.org/10.1007/978-3-642-05381-8.

1291 Bluestein, H. B., J. B. Houser, M. M. French, J. C. Snyder, G. D. Emmitt, I. Popstefanija,
1292 C. Baldi, and R. T. Bluth, 2014: Observations of the Boundary Layer near
1293 Tornadoes and in Supercells Using a Mobile, Collocated, Pulsed Doppler Lidar and
1294 Radar. *JOURNAL OF ATMOSPHERIC AND OCEANIC TECHNOLOGY*, **31**.

1295 Bluestein, H. B., K. J. Thiem, J. C. Snyder, and J. B. Houser, 2018: The Multiple-Vortex
1296 Structure of the El Reno, Oklahoma, Tornado on 31 May 2013. *Monthly Weather*
1297 *Review*, **146**, 2483–2502, https://doi.org/10.1175/MWR-D-18-0073.1.

1298 ——, ——, ——, and ——, 2019: Tornadogenesis and Early Tornado Evolution in the El
1299 Reno, Oklahoma, Supercell on 31 May 2013. *Monthly Weather Review*, **147**, 2045–
1300 2066, https://doi.org/10.1175/MWR-D-18-0338.1.

1301 Bradshaw, P., and Y. M. Koh, 1981: A note on Poisson's equation for pressure in a
1302 turbulent flow. *Phys. Fluids*, **24**, 777, https://doi.org/10.1063/1.863442.

1303 Brooks, E. M., 1949: The Tornado Cyclone. *Weatherwise*, **2**, 32–33,
1304 https://doi.org/10.1080/00431672.1949.9930047.

1305 Brown, R. A., and V. T. Wood, 1991: On the Interpretation of Single-Doppler Velocity
1306 Patterns within Severe Thunderstorms.

1307 Coffer, B. E., and M. D. Parker, 2015: Impacts of Increasing Low-Level Shear on
1308 Supercells during the Early Evening Transition. *Monthly Weather Review*, **143**,
1309 1945–1969, https://doi.org/10.1175/MWR-D-14-00328.1.

1310 ——, and ——, 2017: Simulated Supercells in Nontornadic and Tornadic VORTEX2
1311 Environments. *Monthly Weather Review*, **145**, 149–180,
1312 https://doi.org/10.1175/MWR-D-16-0226.1.

1313 ——, and ——, 2018: Is There a "Tipping Point" between Simulated Nontornadic and
1314 Tornadic Supercells in VORTEX2 Environments? *Monthly Weather Review*, **146**,
1315 2667–2693, https://doi.org/10.1175/MWR-D-18-0050.1.

1316 ——, ——, J. M. L. Dahl, L. J. Wicker, and A. J. Clark, 2017: Volatility of Tornadogenesis:
1317 An Ensemble of Simulated Nontornadic and Tornadic Supercells in VORTEX2
1318 Environments. *Mon. Wea. Rev.*, **145**, 4605–4625, https://doi.org/10.1175/MWR-D-
1319 17-0152.1.

——, ——, J. M. Peters, and A. R. Wade, 2023: Supercell Low-Level Mesocyclones: Origins of Inflow and Vorticity. *Monthly Weather Review*, **151**, 2205–2232, https://doi.org/10.1175/MWR-D-22-0269.1.

Dahl, J. M. L., 2024: The Development of Rotation in Simulated Dust-Devil-Like Vortices. *Journal of the Atmospheric Sciences*, https://doi.org/10.1175/JAS-D-23-0228.1.

Davenport, C. E., and M. D. Parker, 2015: Impact of Environmental Heterogeneity on the Dynamics of a Dissipating Supercell Thunderstorm. *Monthly Weather Review*, **143**, 4244–4277, https://doi.org/10.1175/MWR-D-15-0072.1.

Davies-Jones, R., 1984: Streamwise Vorticity: The Origin of Updraft Rotation in Supercell Storms. *Journal of the Atmospheric Sciences*, **41**, 2991–3006, https://doi.org/10.1175/1520-0469(1984)041<2991:SVTOOU>2.0.CO;2.

——, 1986: *Tornado dynamics. In Thunderstorms: A Social and Technological Documentary*. Second edition revised and enlarged. University of Oklahoma Press 197–236pp.

——, 2002: Linear and Nonlinear Propagation of Supercell Storms. *J. Atmos. Sci.*, **59**, 3178–3205, https://doi.org/10.1175/1520-0469(2003)059<3178:LANPOS>2.0.CO;2.

——, 2003: An Expression for Effective Buoyancy in Surroundings with Horizontal Density Gradients. *Journal of the Atmospheric Sciences*, **60**, 2922–2925, https://doi.org/10.1175/1520-0469(2003)060<2922:AEFEBI>2.0.CO;2.

——, 2015: A review of supercell and tornado dynamics. *Atmospheric Research*, **158–159**, 274–291, https://doi.org/10.1016/j.atmosres.2014.04.007.

——, R. J. Trapp, and H. B. Bluestein, 2001: Tornadoes and Tornadic Storms. *Meteorological Monographs*, **50**, 167–222, https://doi.org/10.1175/0065-9401-28.50.167.

Dawson, D. T., M. Xue, A. Shapiro, J. A. Milbrandt, and A. D. Schenkman, 2016: Sensitivity of Real-Data Simulations of the 3 May 1999 Oklahoma City Tornadic Supercell and Associated Tornadoes to Multimoment Microphysics. Part II: Analysis of Buoyancy and Dynamic Pressure Forces in Simulated Tornado-Like Vortices. *Journal of the Atmospheric Sciences*, **73**, 1039–1061, https://doi.org/10.1175/JAS-D-15-0114.1.

Deardorff, J. W., 1974: Three-dimensional numerical study of turbulence in an entraining mixed layer. *Boundary-Layer Meteorol*, **7**, 199–226, https://doi.org/10.1007/BF00227913.

Djurić, D., 1994: *Weather analysis*. Prentice Hall 304pp.

Doswell, C. A., and P. M. Markowski, 2004: Is Buoyancy a Relative Quantity? *Mon. Wea. Rev.*, **132**, 853–863, https://doi.org/10.1175/1520-0493(2004)132<0853:IBARQ>2.0.CO;2.

Flournoy, M. D., M. C. Coniglio, E. N. Rasmussen, J. C. Furtado, and B. E. Coffer, 2020: Modes of Storm-Scale Variability and Tornado Potential in VORTEX2 Near- and Far-Field Tornadic Environments. *Monthly Weather Review*, **148**, 4185–4207, https://doi.org/10.1175/MWR-D-20-0147.1.

French, M. M., H. B. Bluestein, I. PopStefanija, C. A. Baldi, and R. T. Bluth, 2013: Reexamining the Vertical Development of Tornadic Vortex Signatures in Supercells, https://doi.org/10.1175/MWR-D-12-00315.1.

Fujita, T., 1958: MESOANALYSIS OF THE ILLINOIS TORNADOES OF 9 APRIL 1953. *Journal of Atmospheric Sciences*, **15**, 288–296.

Goldacker, N. A., and M. D. Parker, 2021: Low-Level Updraft Intensification in Response to Environmental Wind Profiles. *Journal of the Atmospheric Sciences*, **78**, 2763–2781, https://doi.org/10.1175/JAS-D-20-0354.1.

Hastings, R., and Y. Richardson, 2016: Long-Term Morphological Changes in Simulated Supercells Following Mergers with Nascent Supercells in Directionally Varying Shear, https://doi.org/10.1175/MWR-D-15-0193.1.

Houser, J. L., H. B. Bluestein, and J. C. Snyder, 2015: Rapid-Scan, Polarimetric, Doppler Radar Observations of Tornadogenesis and Tornado Dissipation in a Tornadic Supercell: The "El Reno, Oklahoma" Storm of 24 May 2011, https://doi.org/10.1175/MWR-D-14-00253.1.

Houze, R. A., 2014: Basic Cumulus Dynamics. *International Geophysics*, Vol. 104 of, Elsevier, 165–185, https://doi.org/10.1016/B978-0-12-374266-7.00007-X.

Huang, W., and M. Xue, 2023: Sub-vortices Within a Numerically Simulated Tornado: The Role of Unstable Vortex Rossby Waves. *Journal of the Atmospheric Sciences*, **1**, https://doi.org/10.1175/JAS-D-22-0237.1.

Jeevanjee, N., and D. M. Romps, 2016: Effective buoyancy at the surface and aloft. *Quarterly Journal of the Royal Meteorological Society*, **142**, 811–820, https://doi.org/10.1002/qj.2683.

Klemp, J. B., and R. Rotunno, 1983: A Study of the Tornadic Region within a Supercell Thunderstorm. *Journal of the Atmospheric Sciences*, **40**, 359–377, https://doi.org/10.1175/1520-0469(1983)040<0359:ASOTTR>2.0.CO;2.

Lilly, D. K., 1982: The Development and Maintenance of Rotation in Convective Storms. *Intense Atmospheric Vortices. Topics in Atmospheric and Oceanographic Sciences.*, L. Bengtsson and J. Lighthill, Eds., Springer Berlin Heidelberg, 149–160, https://doi.org/10.1007/978-3-642-81866-0_12.

Markowski, P., and Y. Richardson, 2010: *Mesoscale Meteorology in Midlatitudes*. John Wiley & Sons, Ltd, https://doi.org/10.1002/9780470682104.

Markowski, P. M., 2024: A New Pathway for Tornadogenesis Exposed by Numerical Simulations of Supercells in Turbulent Environments. *Journal of the Atmospheric Sciences*, **81**, 481–518, https://doi.org/10.1175/JAS-D-23-0161.1.

——, and Y. P. Richardson, 2014: The Influence of Environmental Low-Level Shear and Cold Pools on Tornadogenesis: Insights from Idealized Simulations. *Journal of the Atmospheric Sciences*, **71**, 243–275, https://doi.org/10.1175/JAS-D-13-0159.1.

McCaul, E. W., and M. L. Weisman, 1996: Simulations of Shallow Supercell Storms in Landfalling Hurricane Environments. *Monthly Weather Review*, **124**, 408–429, https://doi.org/10.1175/1520-0493(1996)124<0408:SOSSSI>2.0.CO;2.

——, and ——, 2001: The Sensitivity of Simulated Supercell Structure and Intensity to Variations in the Shapes of Environmental Buoyancy and Shear Profiles. *Mon. Wea. Rev.*, **129**, 664–687, https://doi.org/10.1175/1520-0493(2001)129<0664:TSOSSS>2.0.CO;2.

Meng, Z., and Coauthors, 2018: The Deadliest Tornado (EF4) in the Past 40 Years in China. *Weather and Forecasting*, **33**, 693–713, https://doi.org/10.1175/WAF-D-17-0085.1.

Morrison, H., and W. W. Grabowski, 2008: Modeling Supersaturation and Subgrid-Scale Mixing with Two-Moment Bulk Warm Microphysics. *Journal of the Atmospheric Sciences*, **65**, 792–812, https://doi.org/10.1175/2007JAS2374.1.

——, and J. M. Peters, 2018: Theoretical Expressions for the Ascent Rate of Moist Deep Convective Thermals. *Journal of the Atmospheric Sciences*, **75**, 1699–1719, https://doi.org/10.1175/JAS-D-17-0295.1.

Muehr, A. J., J. H. Ruppert, M. D. Flournoy, and J. M. Peters, 2024: The Influence of Midlevel Shear and Horizontal Rotors on Supercell Updraft Dynamics, https://doi.org/10.1175/JAS-D-23-0082.1.

Parker, M. D., 2023: How well must surface vorticity be organized for tornadogenesis? *Journal of the Atmospheric Sciences*, https://doi.org/10.1175/JAS-D-22-0195.1.

Peters, J. M., 2016: The Impact of Effective Buoyancy and Dynamic Pressure Forcing on Vertical Velocities within Two-Dimensional Updrafts. *Journal of the Atmospheric Sciences*, **73**, 4531–4551, https://doi.org/10.1175/JAS-D-16-0016.1.

——, C. J. Nowotarski, and H. Morrison, 2019: The Role of Vertical Wind Shear in Modulating Maximum Supercell Updraft Velocities. *Journal of the Atmospheric Sciences*, **76**, 3169–3189, https://doi.org/10.1175/JAS-D-19-0096.1.

Pleim, J. E., 2006: A Simple, Efficient Solution of Flux–Profile Relationships in the Atmospheric Surface Layer. *Journal of Applied Meteorology and Climatology*, **45**, 341–347, https://doi.org/10.1175/JAM2339.1.

——, 2007: A Combined Local and Nonlocal Closure Model for the Atmospheric Boundary Layer. Part I: Model Description and Testing. *Journal of Applied Meteorology and Climatology*, **46**, 1383–1395, https://doi.org/10.1175/JAM2539.1.

Roberts, B., and M. Xue, 2017: The Role of Surface Drag in Mesocyclone Intensification Leading to Tornadogenesis within an Idealized Supercell Simulation. *Journal of the Atmospheric Sciences*, **74**, 3055–3077, https://doi.org/10.1175/JAS-D-16-0364.1.

——, ——, A. D. Schenkman, and D. T. Dawson, 2016: The Role of Surface Drag in Tornadogenesis within an Idealized Supercell Simulation. *Journal of the Atmospheric Sciences*, **73**, 3371–3395, https://doi.org/10.1175/JAS-D-15-0332.1.

——, ——, and D. T. Dawson, 2020: The Effect of Surface Drag Strength on Mesocyclone Intensification and Tornadogenesis in Idealized Supercell Simulations. *Journal of the Atmospheric Sciences*, **77**, 1699–1721, https://doi.org/10.1175/JAS-D-19-0109.1.

Robertson, S. D., 2017: Intensification of the Low-Level Updraft in Supercells Preceding Tornadogenesis. Texas Tech University, 82pp.

Rotunno, R., 2013: The Fluid Dynamics of Tornadoes. *Annu. Rev. Fluid Mech.*, **45**, 59–84, https://doi.org/10.1146/annurev-fluid-011212-140639.

——, and J. B. Klemp, 1982: The Influence of the Shear-Induced Pressure Gradient on Thunderstorm Motion. *Monthly Weather Review*, **110**, 136–151, https://doi.org/10.1175/1520-0493(1982)110<0136:TIOTSI>2.0.CO;2.

——, and J. Klemp, 1985: On the Rotation and Propagation of Simulated Supercell Thunderstorms. *Journal of the Atmospheric Sciences*, **42**, 271–292, https://doi.org/10.1175/1520-0469(1985)042<0271:OTRAPO>2.0.CO;2.

Rowland, H. A., 1880: On the Motion of a Perfect Incompressible Fluid When no Solid Bodies are Present. *American Journal of Mathematics*, **3**, 226–268, https://doi.org/10.2307/2369424.

Schenkman, A. D., M. Xue, and M. Hu, 2014: Tornadogenesis in a High-Resolution Simulation of the 8 May 2003 Oklahoma City Supercell. *Journal of the Atmospheric Sciences*, **71**, 130–154, https://doi.org/10.1175/JAS-D-13-073.1.

——, ——, and D. T. Dawson II, 2016: The Cause of Internal Outflow Surges in a High-Resolution Simulation of the 8 May 2003 Oklahoma City Tornadic Supercell. *Journal of the Atmospheric Sciences*, **73**, 353–370, https://doi.org/10.1175/JAS-D-15-0112.1.

Sherburn, K. D., and M. D. Parker, 2019: The Development of Severe Vortices within Simulated High-Shear, Low-CAPE Convection. *Monthly Weather Review*, **147**, 2189–2216, https://doi.org/10.1175/MWR-D-18-0246.1.

Skamarock, W. C., and Coauthors,: A Description of the Advanced Research WRF Version 3. 125.

Skinner, P. S., C. C. Weiss, M. M. French, H. B. Bluestein, P. M. Markowski, and Y. P. Richardson, 2014: VORTEX2 Observations of a Low-Level Mesocyclone with Multiple Internal Rear-Flank Downdraft Momentum Surges in the 18 May 2010

Dumas, Texas, Supercell. *Monthly Weather Review*, **142**, 2935–2960, https://doi.org/10.1175/MWR-D-13-00240.1.

Smagorinsky, J., 1963: GENERAL CIRCULATION EXPERIMENTS WITH THE PRIMITIVE EQUATIONS: I. THE BASIC EXPERIMENT. *Monthly Weather Review*, **91**, 99–164, https://doi.org/10.1175/1520-0493(1963)091<0099:GCEWTP>2.3.CO;2.

Sun, Z., M. Xue, K. Zhu, and B. Zhou, 2019: Prediction of an EF4 supercell tornado in Funing, China: Resolution dependency of simulated tornadoes and their structures. *Atmospheric Research*, **229**, 175–189, https://doi.org/10.1016/j.atmosres.2019.06.019.

Wade, A. R., and M. D. Parker, 2021: Dynamics of Simulated High-Shear, Low-CAPE Supercells. *Journal of the Atmospheric Sciences*, **78**, 1389–1410, https://doi.org/10.1175/JAS-D-20-0117.1.

Wakimoto, R. M., and H. Cai, 2000: Analysis of a Nontornadic Storm during VORTEX 95.

Weisman, M. L., and J. B. Klemp, 1984: The Structure and Classification of Numerically Simulated Convective Stormsin Directionally Varying Wind Shears. *Monthly Weather Review*, **112**, 2479–2498, https://doi.org/10.1175/1520-0493(1984)112<2479:TSACON>2.0.CO;2.

——, and R. Rotunno, 2000: The Use of Vertical Wind Shear versus Helicity in Interpreting Supercell Dynamics. *J. Atmos. Sci.*, **57**, 1452–1472, https://doi.org/10.1175/1520-0469(2000)057<1452:TUOVWS>2.0.CO;2.

Xue, M., and Coauthors, 2001: The Advanced Regional Prediction System (ARPS) – A multi-scale nonhydrostatic atmospheric simulation and prediction tool. Part II: Model physics and applications. *Meteorol Atmos Phys*, **76**, 143–165, https://doi.org/10.1007/s007030170027.

Yokota, S., H. Niino, H. Seko, M. Kunii, and H. Yamauchi, 2018: Important Factors for Tornadogenesis as Revealed by High-Resolution Ensemble Forecasts of the Tsukuba Supercell Tornado of 6 May 2012 in Japan. *Mon. Wea. Rev.*, **146**, 1109–1132, https://doi.org/10.1175/MWR-D-17-0254.1.

Ziegler, C. L., E. N. Rasmussen, T. R. Shepherd, A. I. Watson, and J. M. Straka, 2001: The Evolution of Low-Level Rotation in the 29 May 1994 Newcastle–Graham, Texas, Storm Complex during VORTEX.

Fig.1

Click here to access/download;Rendered Figure;UV_reVor_panel_lon_changetime.png

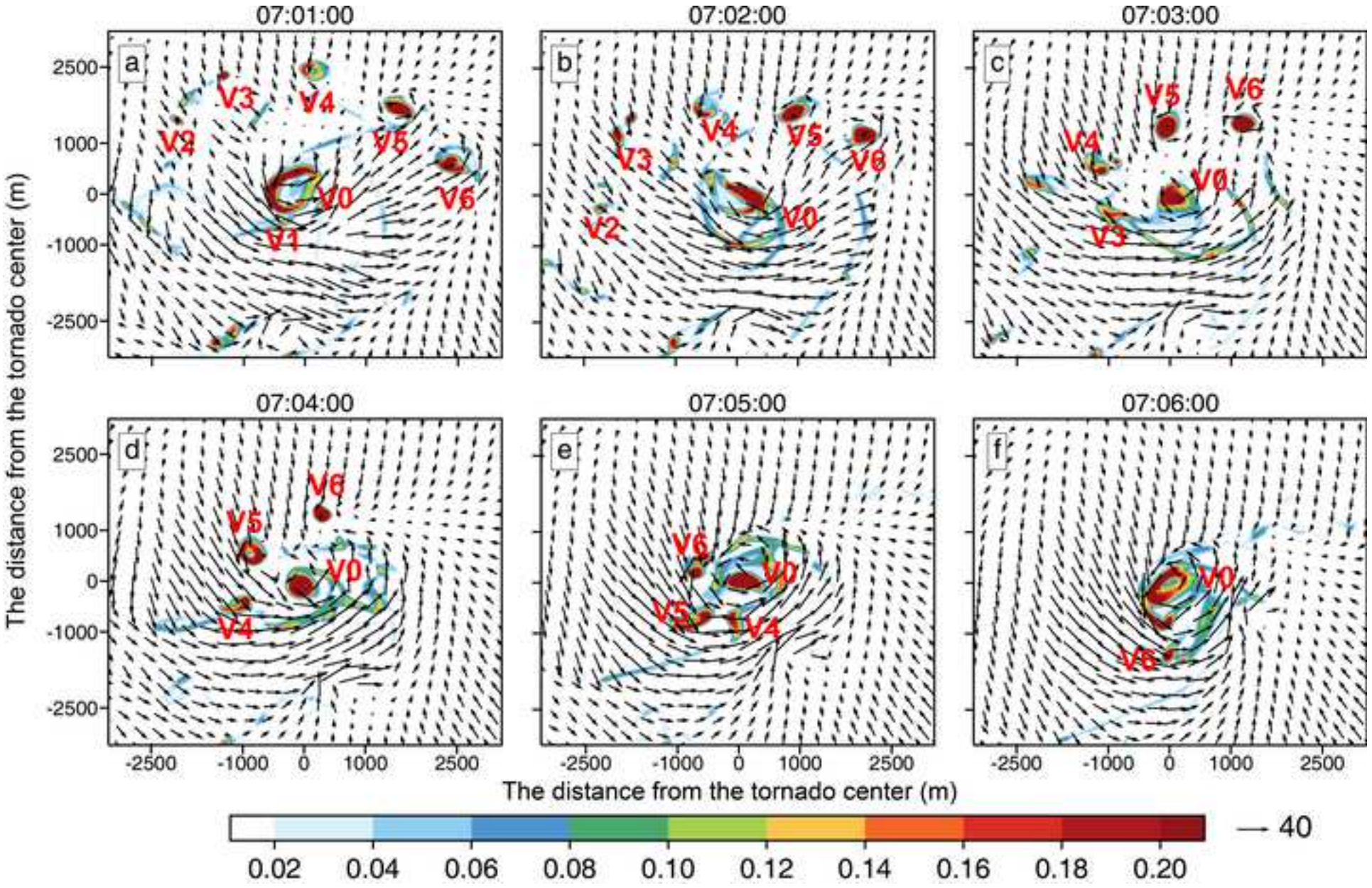

Fig.2

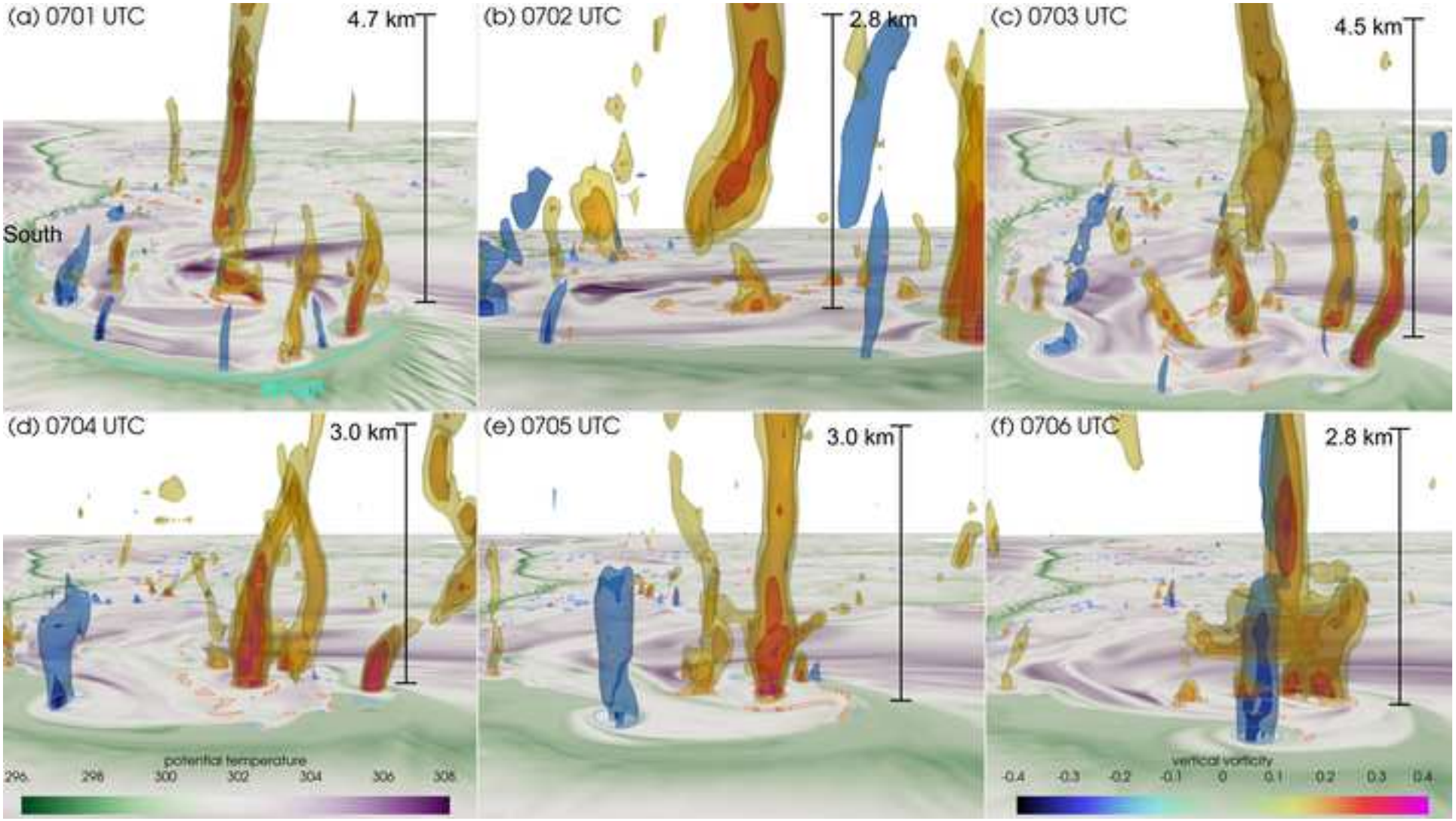

Fig.3

Click here to access/download;Rendered Figure;panel_lowestvorand7thwaccel.png

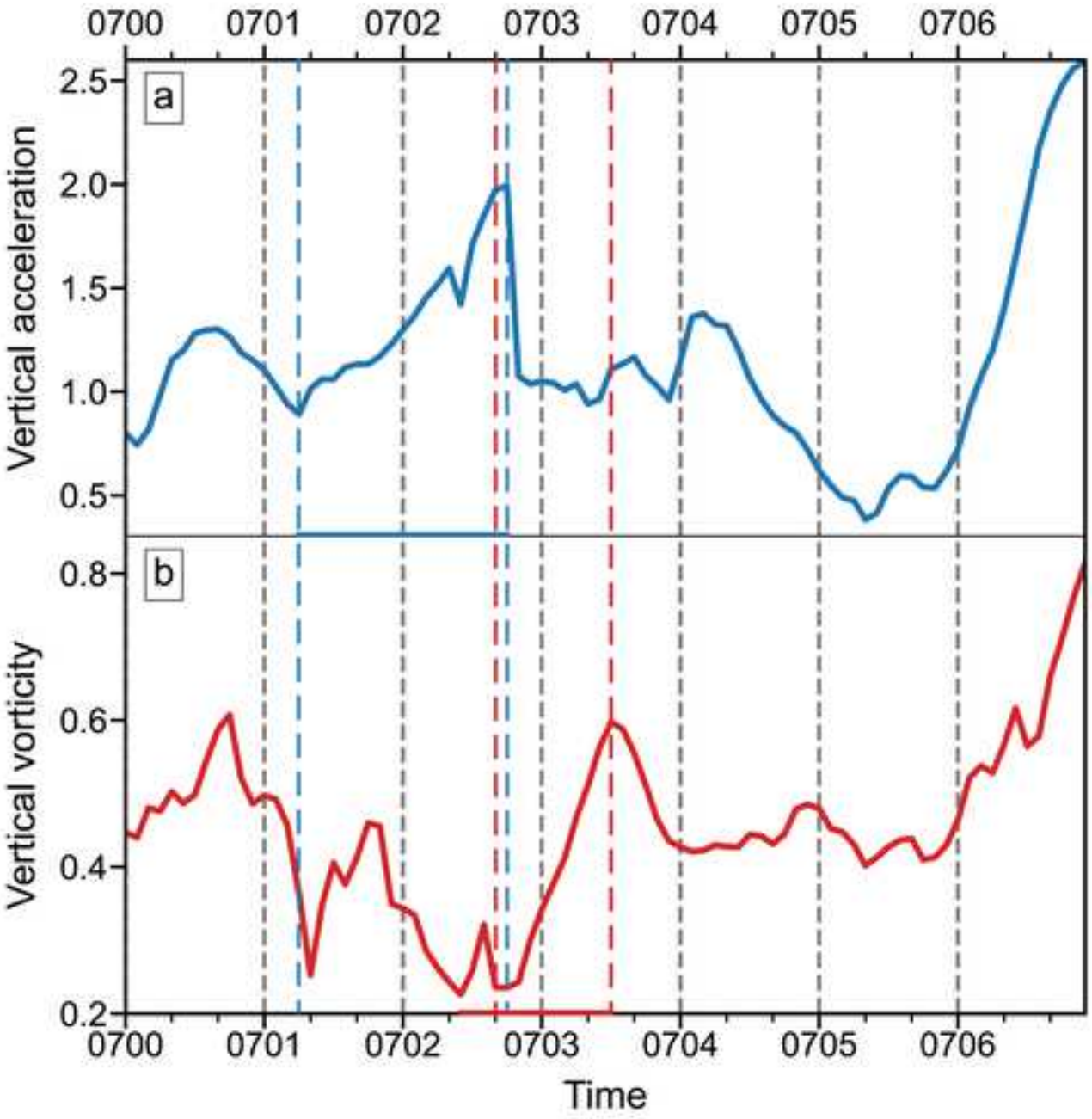

Fig.4

Click here to access/download;Rendered Figure;panel_waccel_d_b_6_voratlowest.png

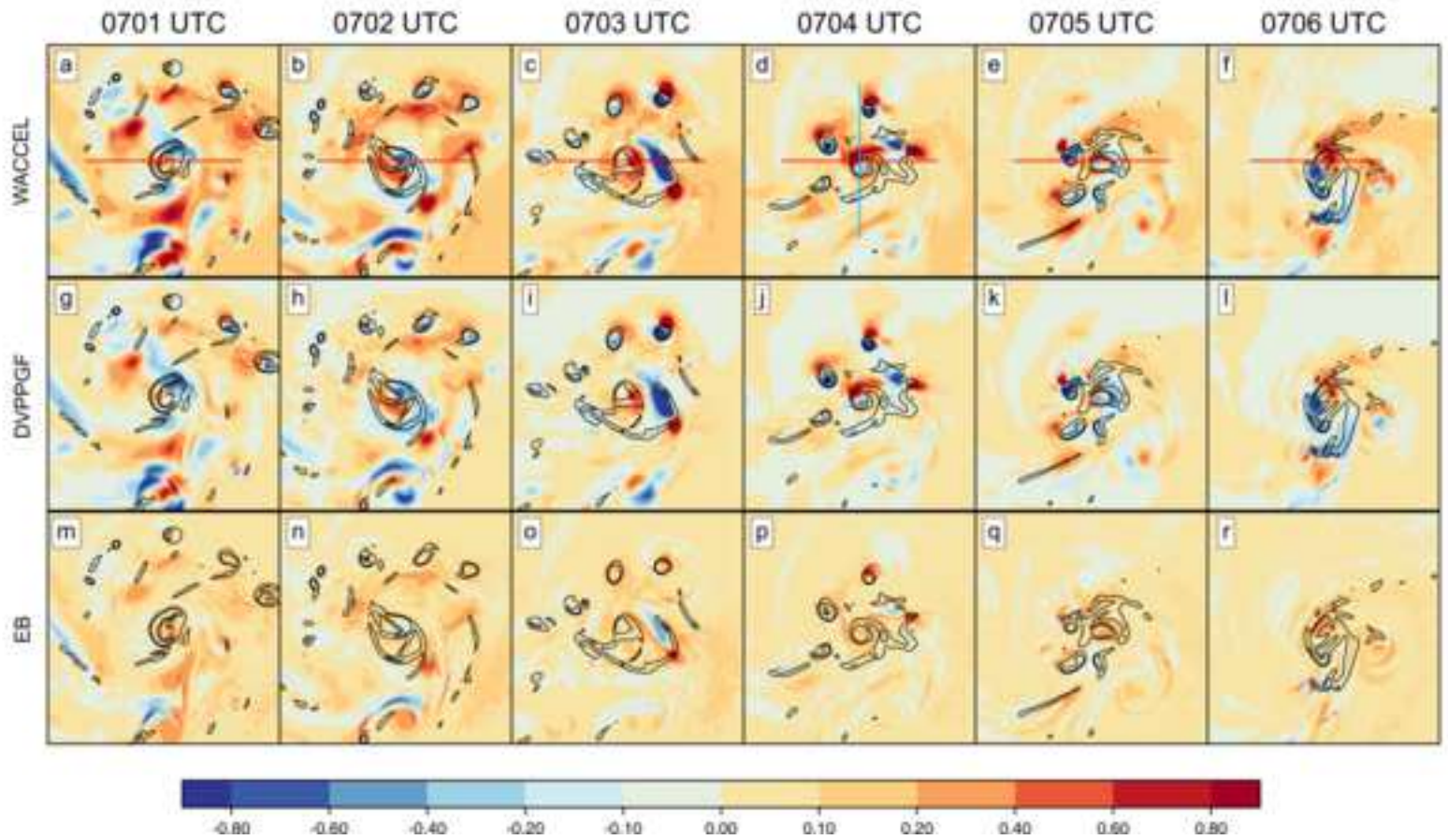

Fig.5

Click here to access/download;Rendered Figure;vertical_cross_waccel_d_b_6_withupdraft.png

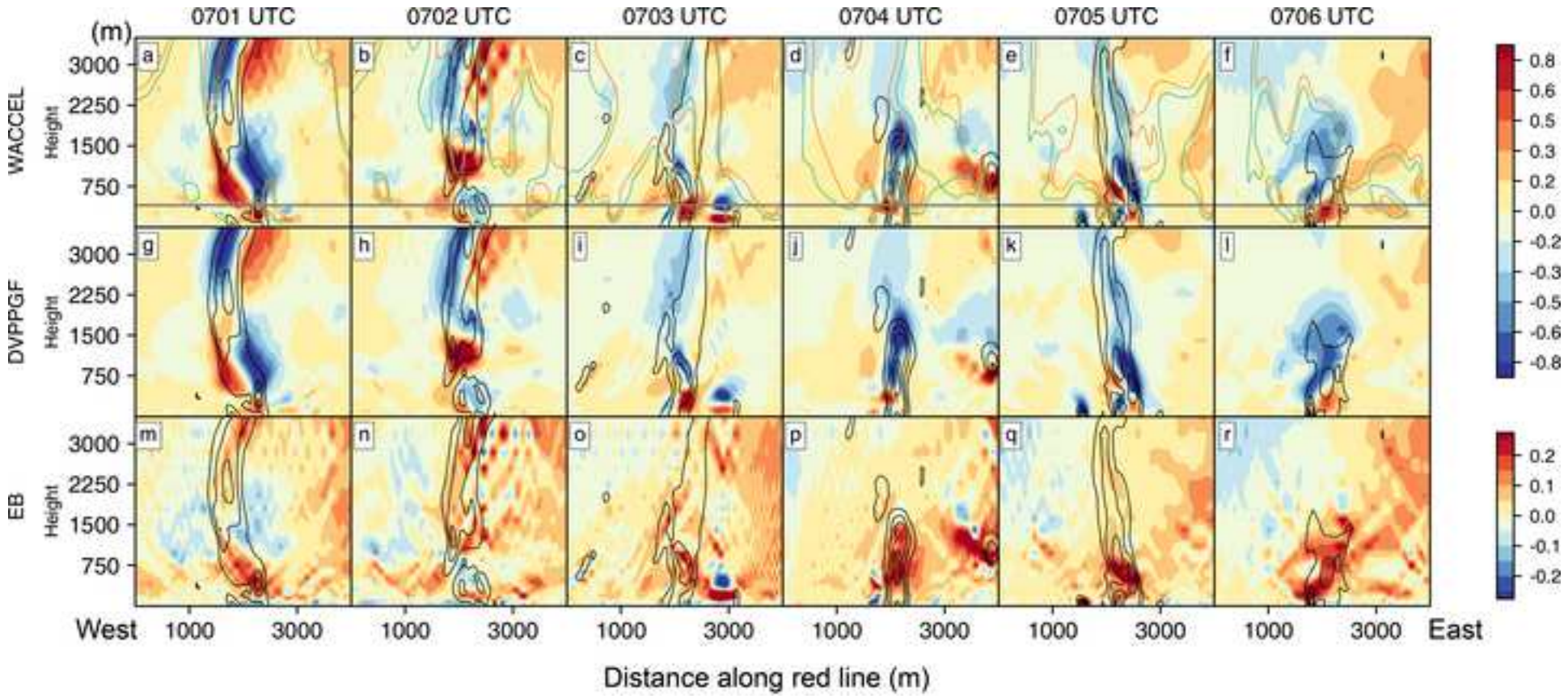

Fig.6

Click here to access/download;Rendered Figure;panel_waccel_d_6_voratlowest.png

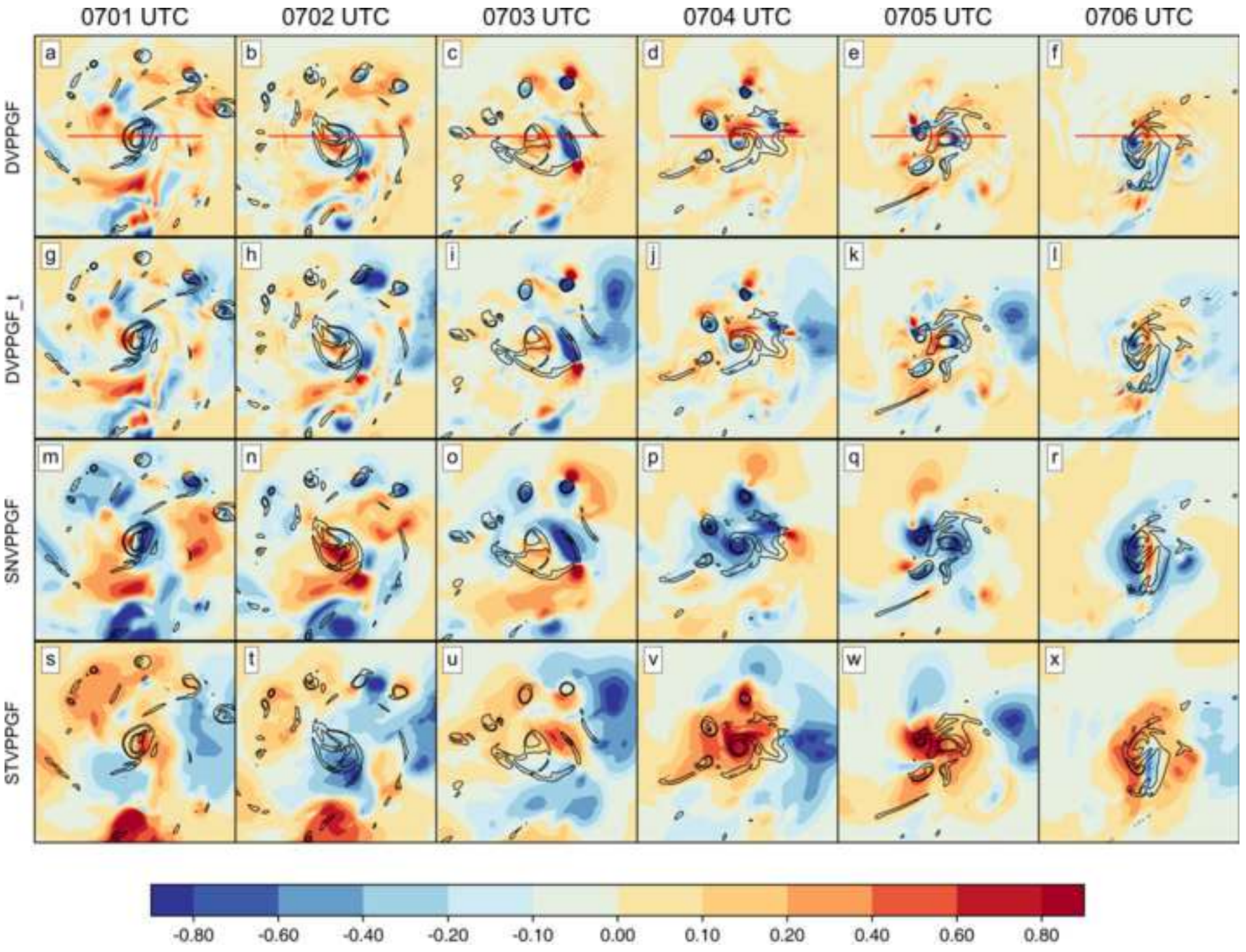

Fig.7

Click here to access/download;Rendered Figure;panel_waccel_d_continue_6_voratlowest.png

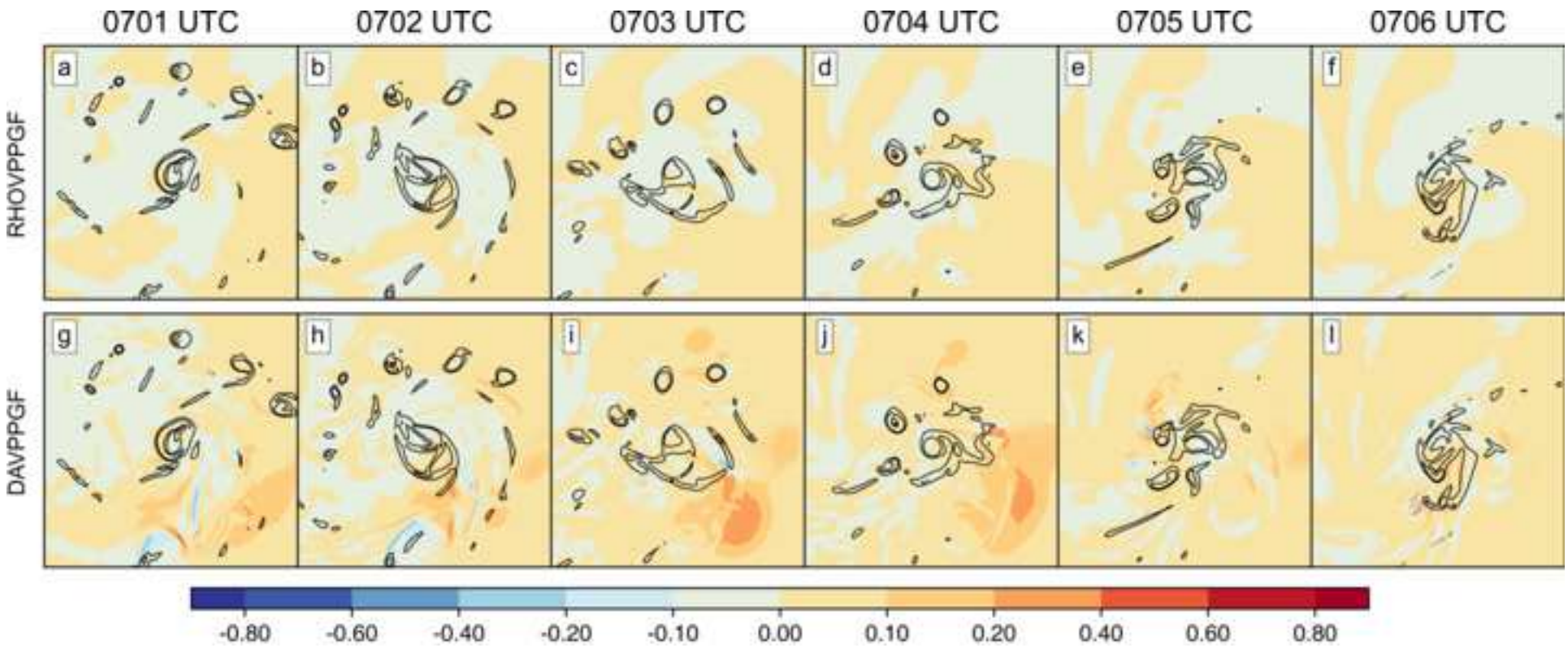

Fig.8

Click here to access/download;Rendered Figure;vertical_cross_d_6_withupdraft.png

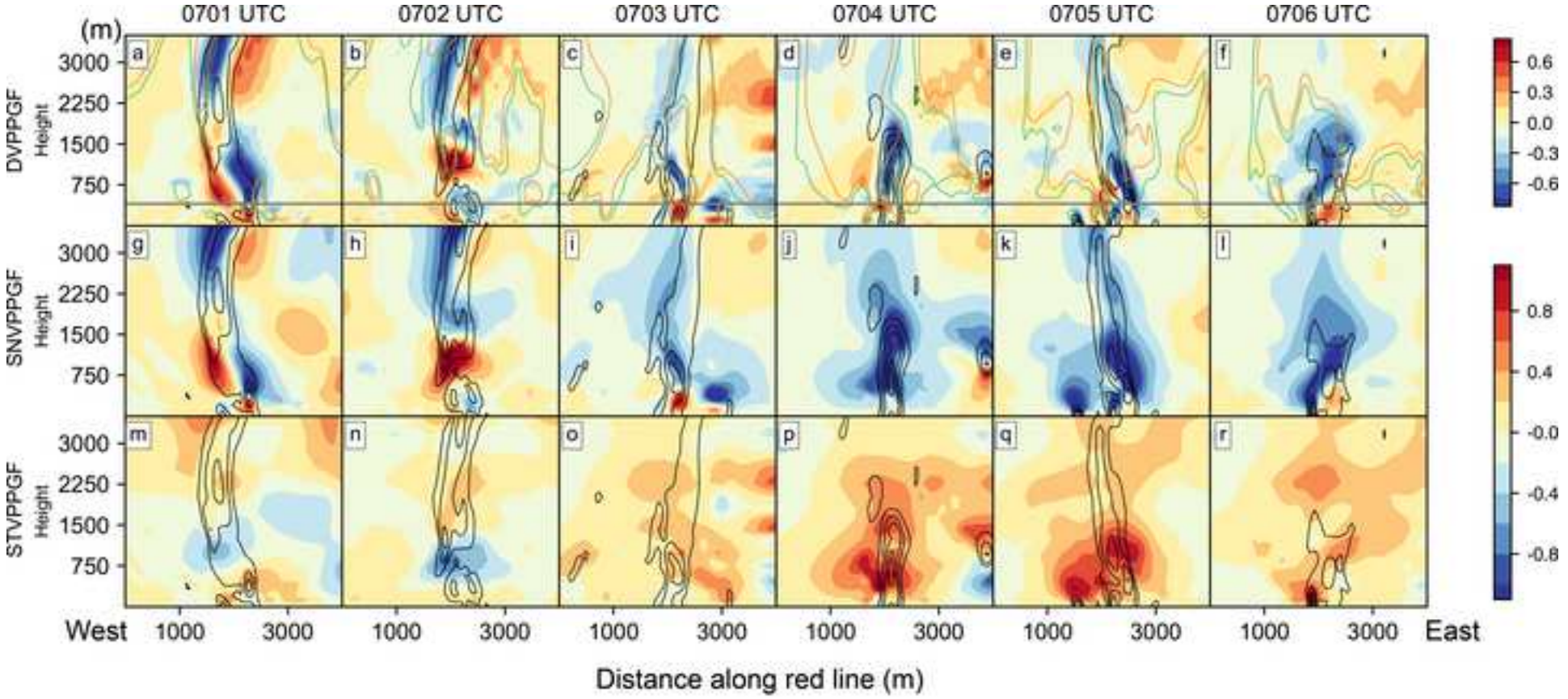

Fig.9

Click here to access/download;Rendered Figure;dynamic_label.png

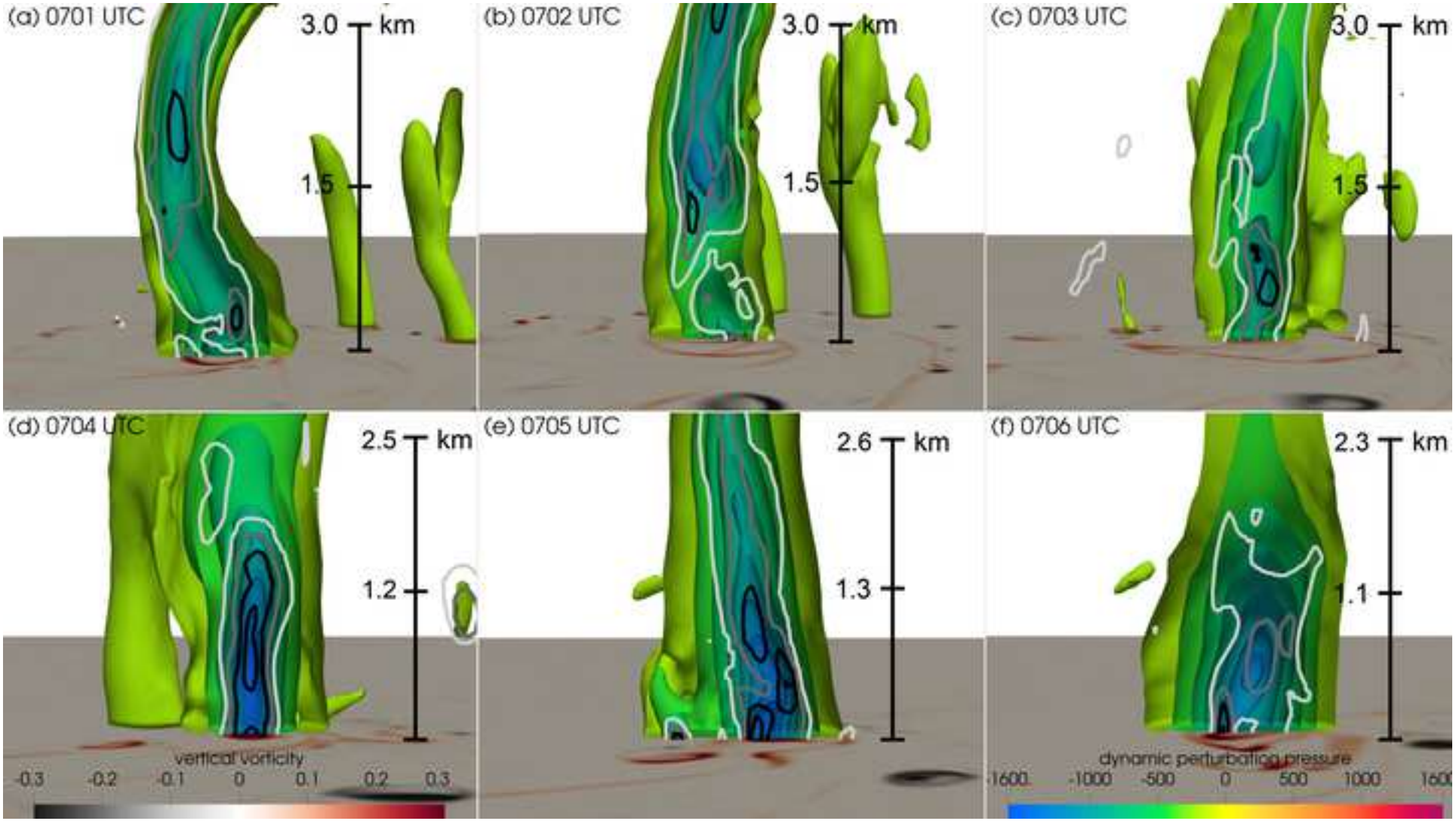

Fig.10

Click here to access/download;Rendered Figure;spin_label.png

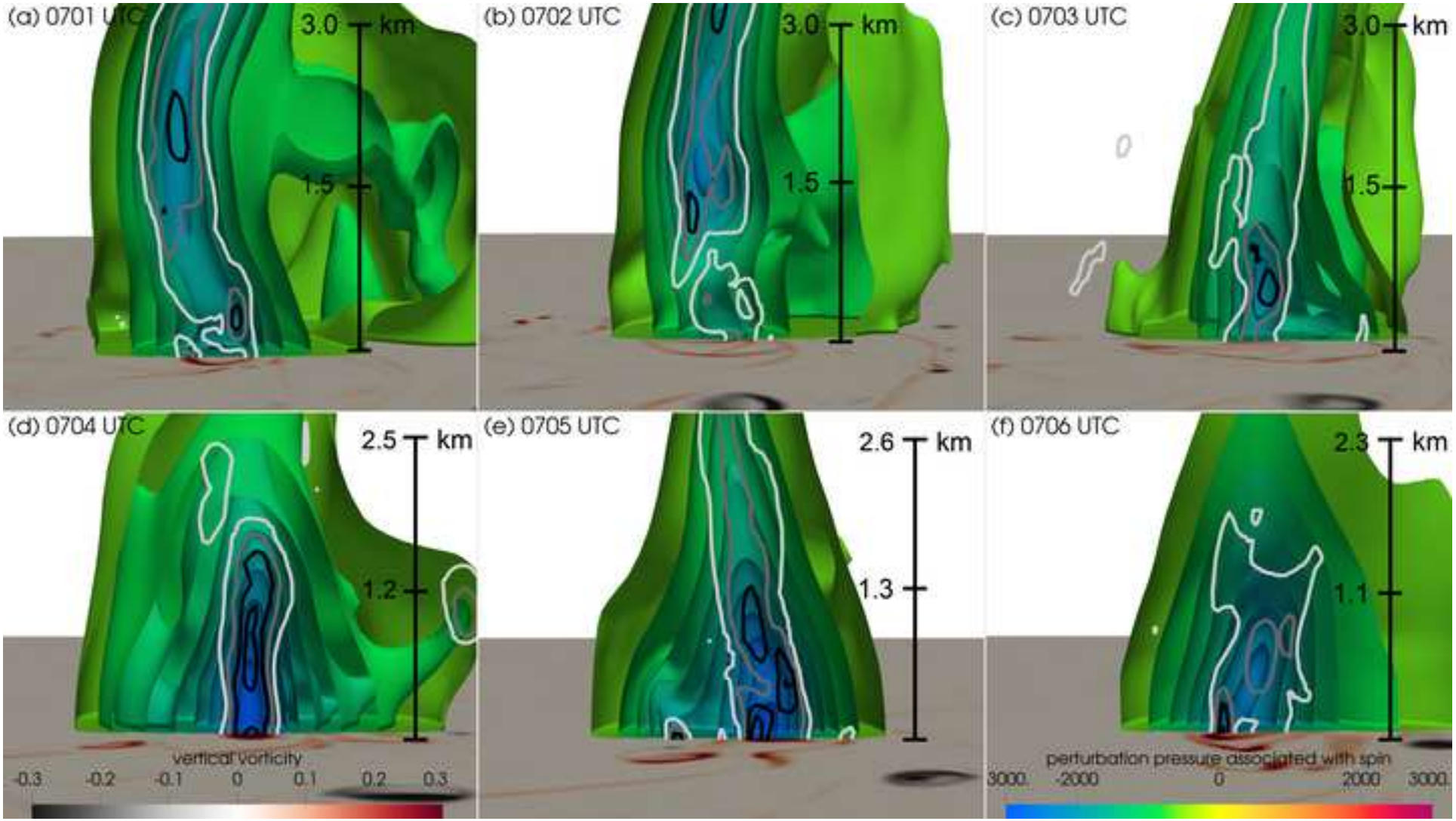

Fig.11

Click here to access/download;Rendered Figure;splat_label.png

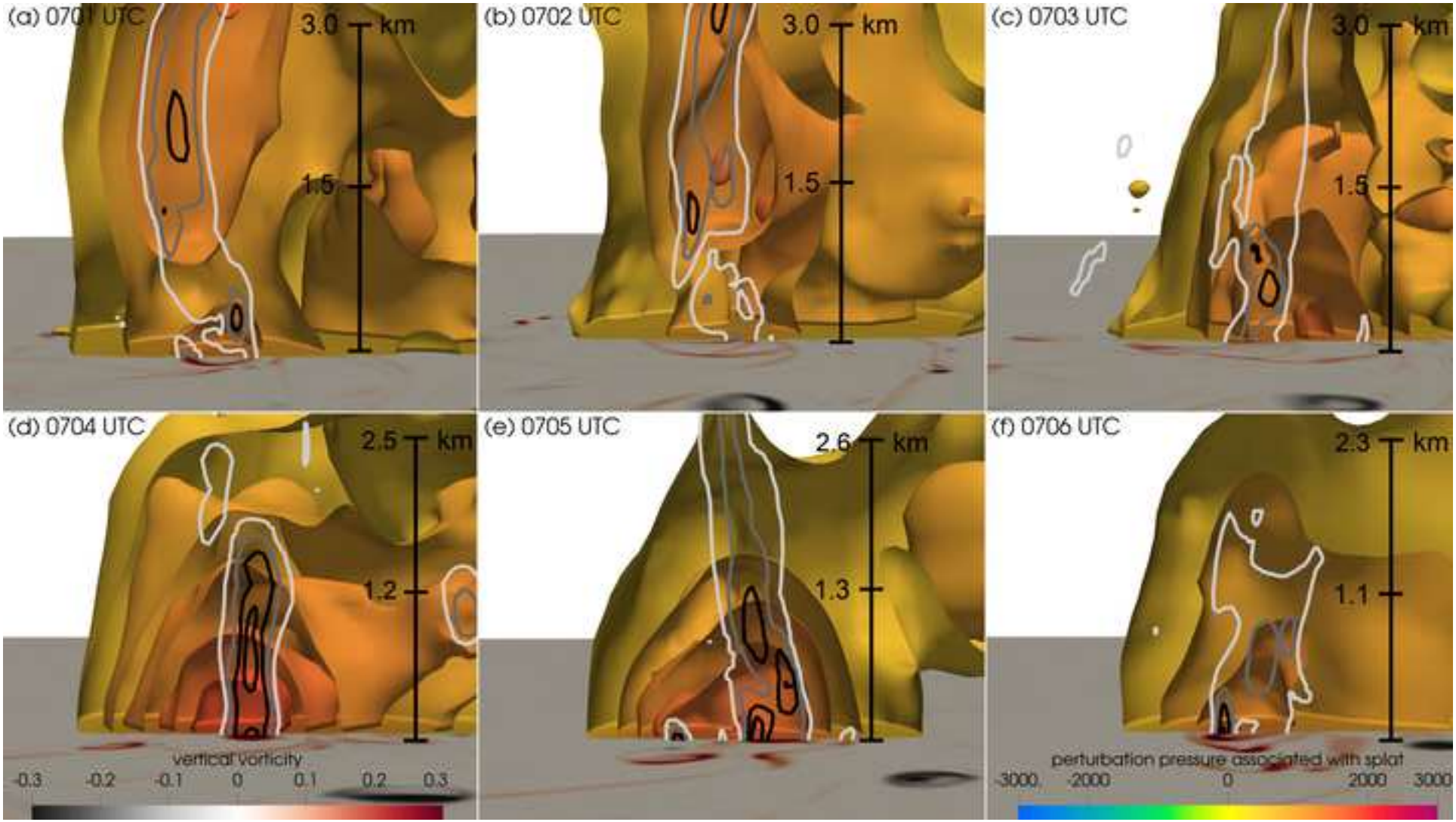

Fig.12

Click here to access/download;Rendered Figure;spin_0701_0704.png

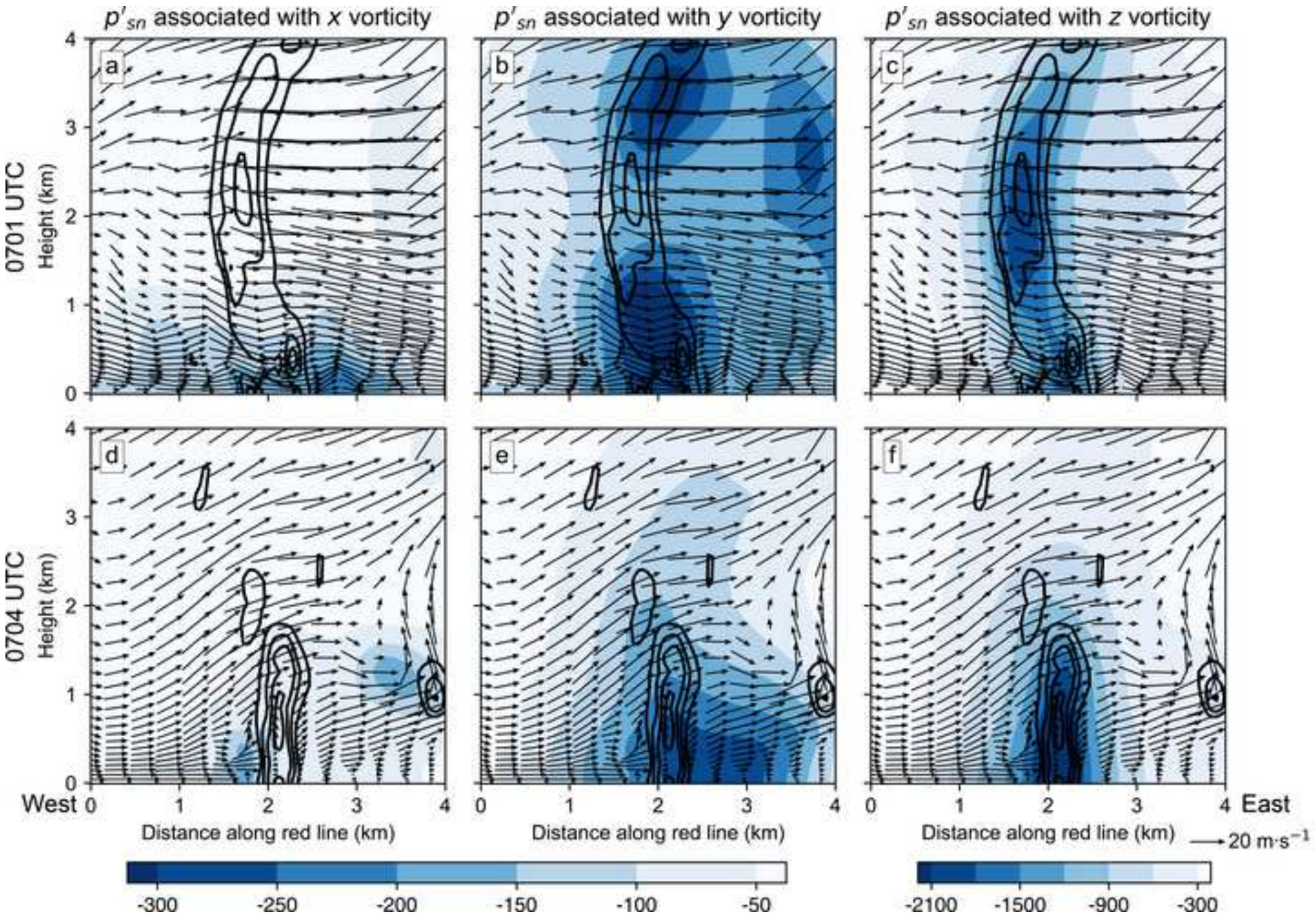

Fig.13

Click here to access/download;Rendered Figure;normal_240.png

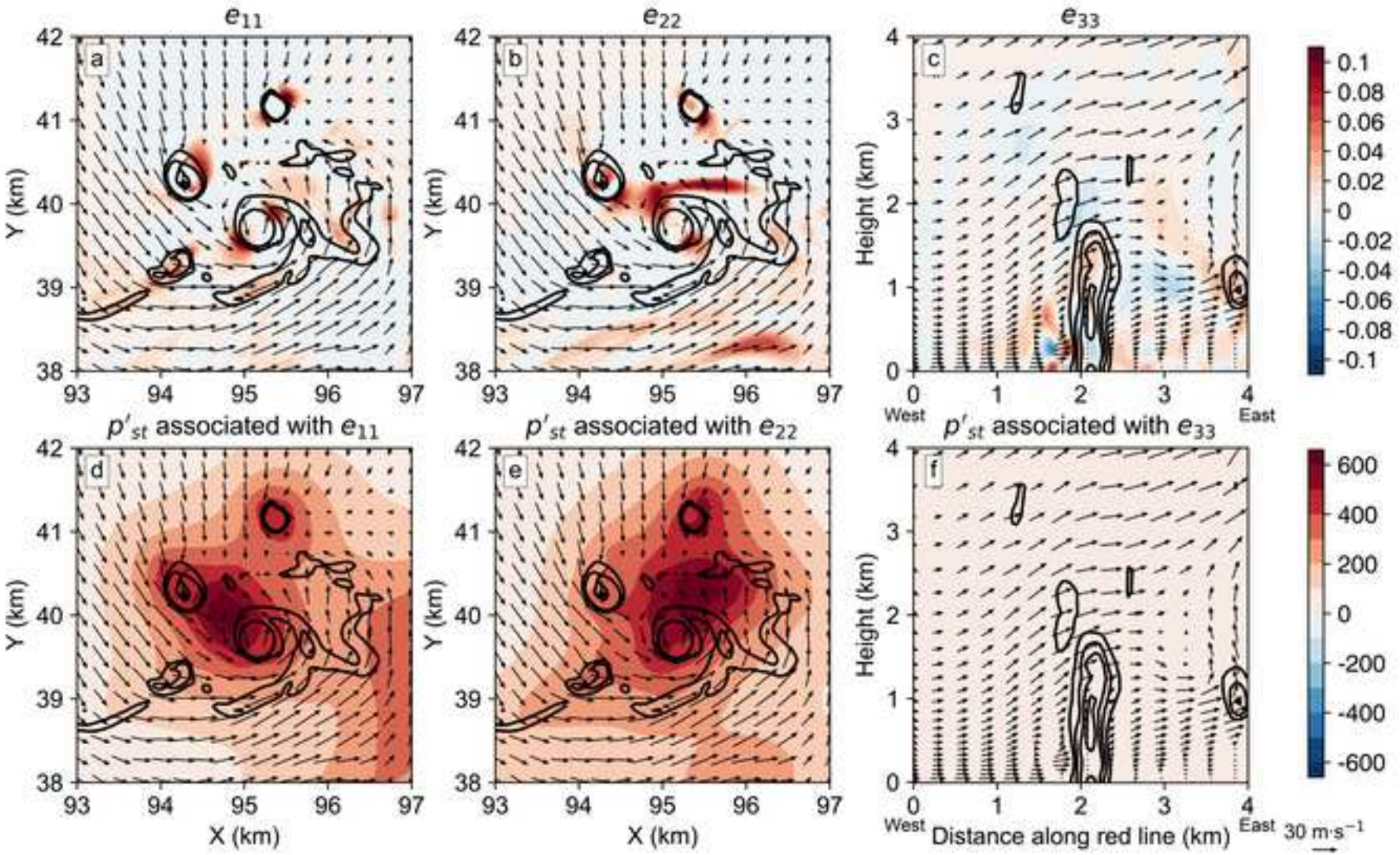

Fig.14

Click here to access/download;Rendered Figure;shear_240.png

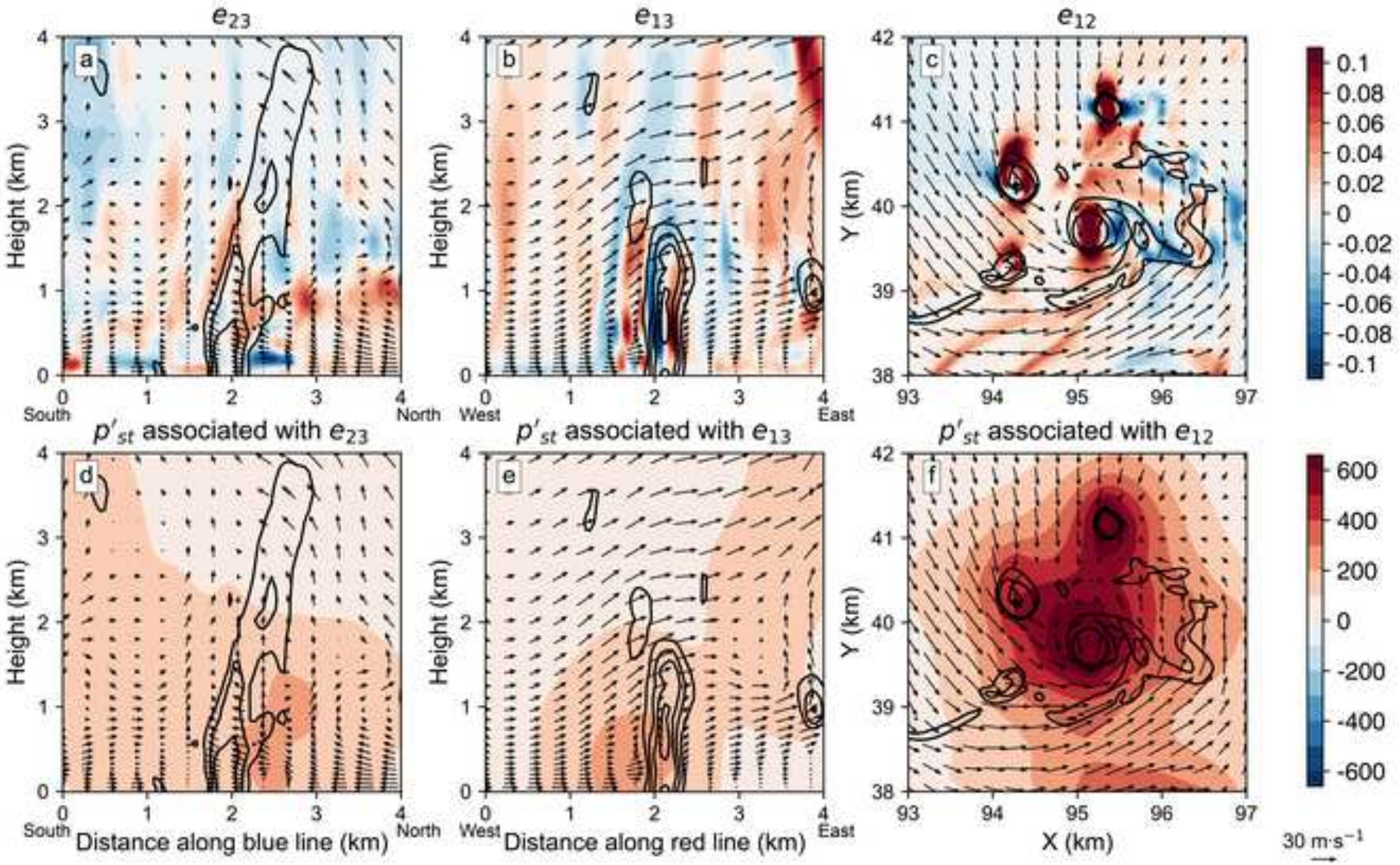

Fig.15

Click here to access/download;Rendered Figure;panel.png

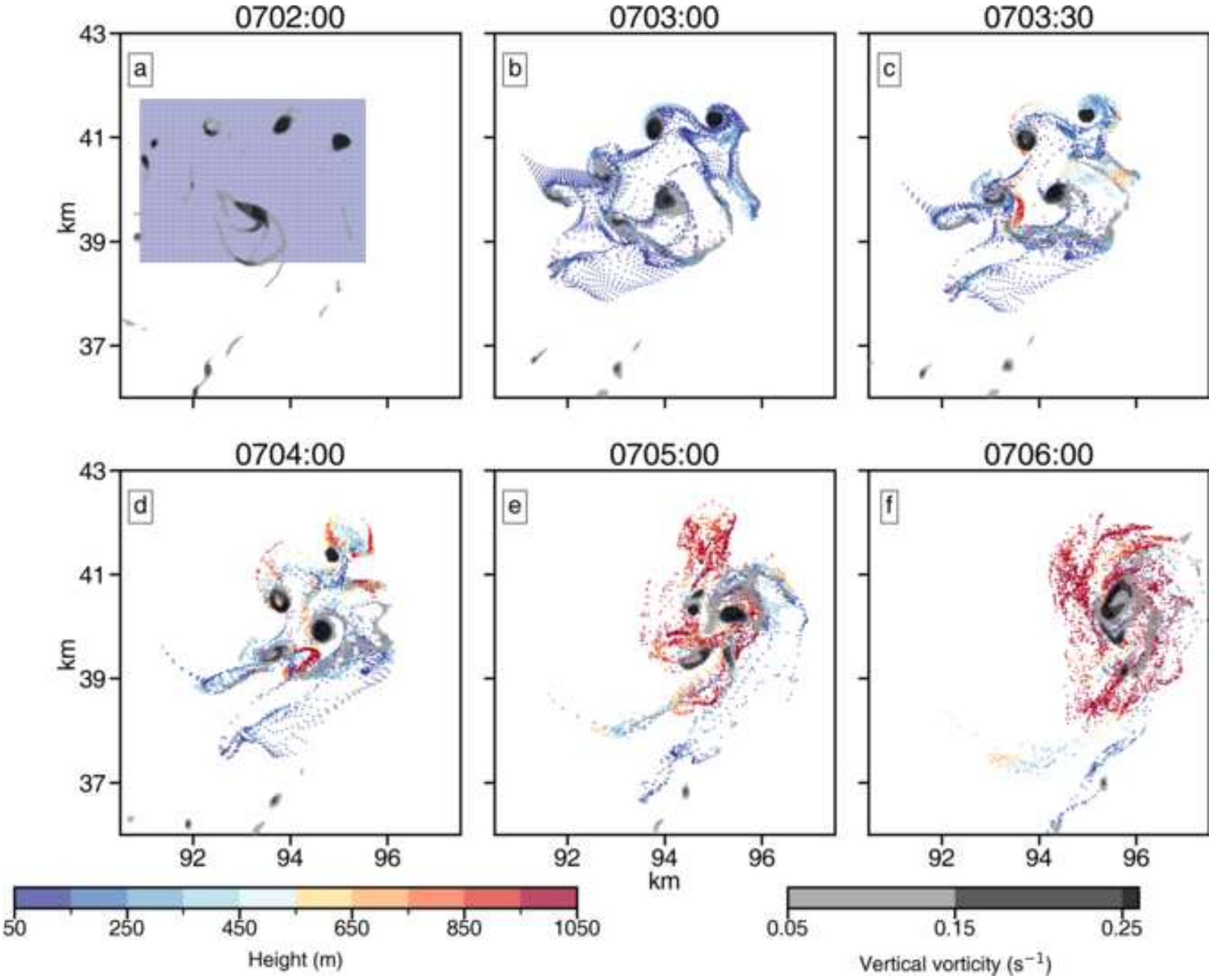

Fig.16

Click here to access/download;Rendered Figure;77_0702_and_240_0703_2Dpanel_seperate.png

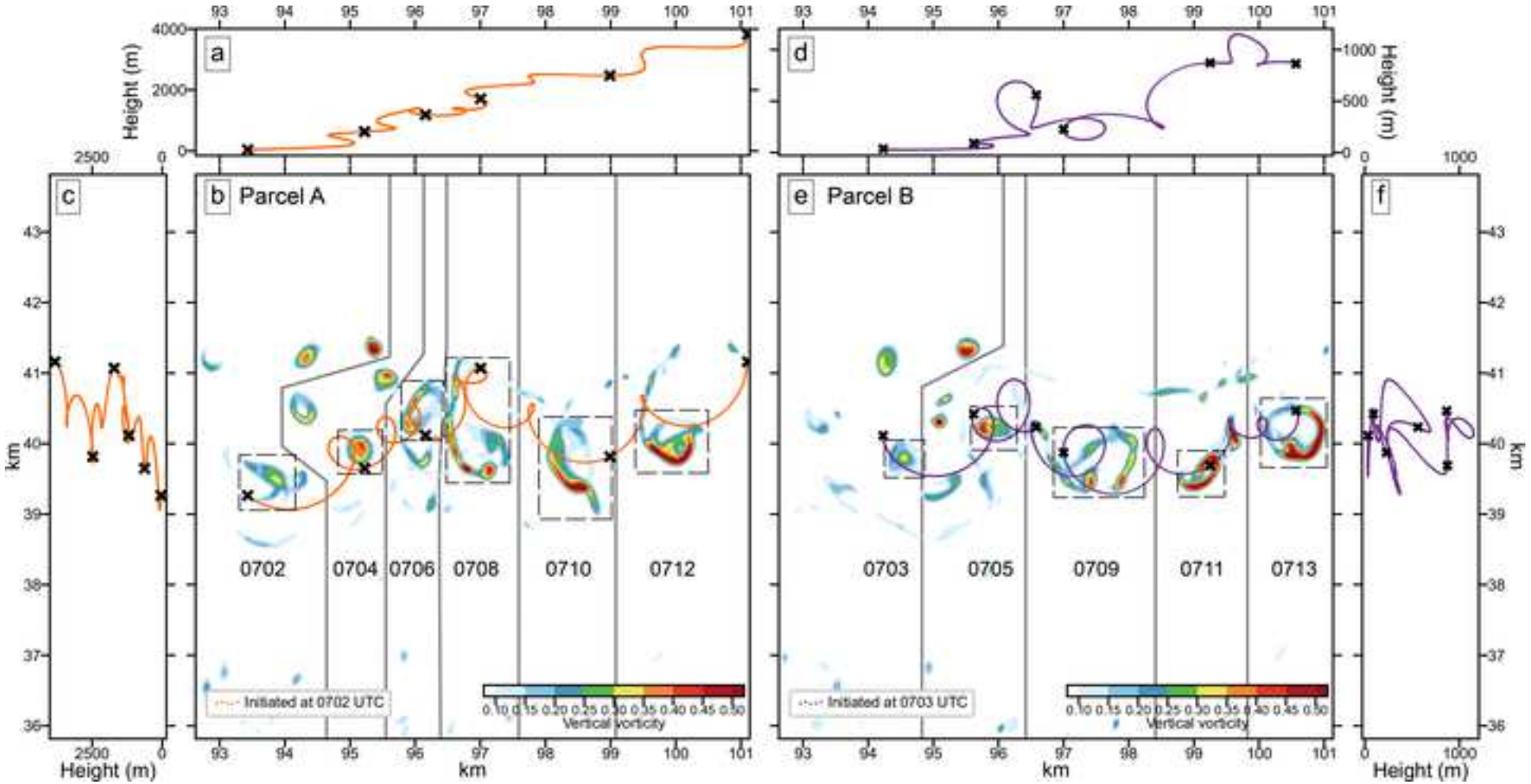

Fig.17

Click here to access/download;Rendered Figure;77_waccel_withvor_and_rh_0702.png

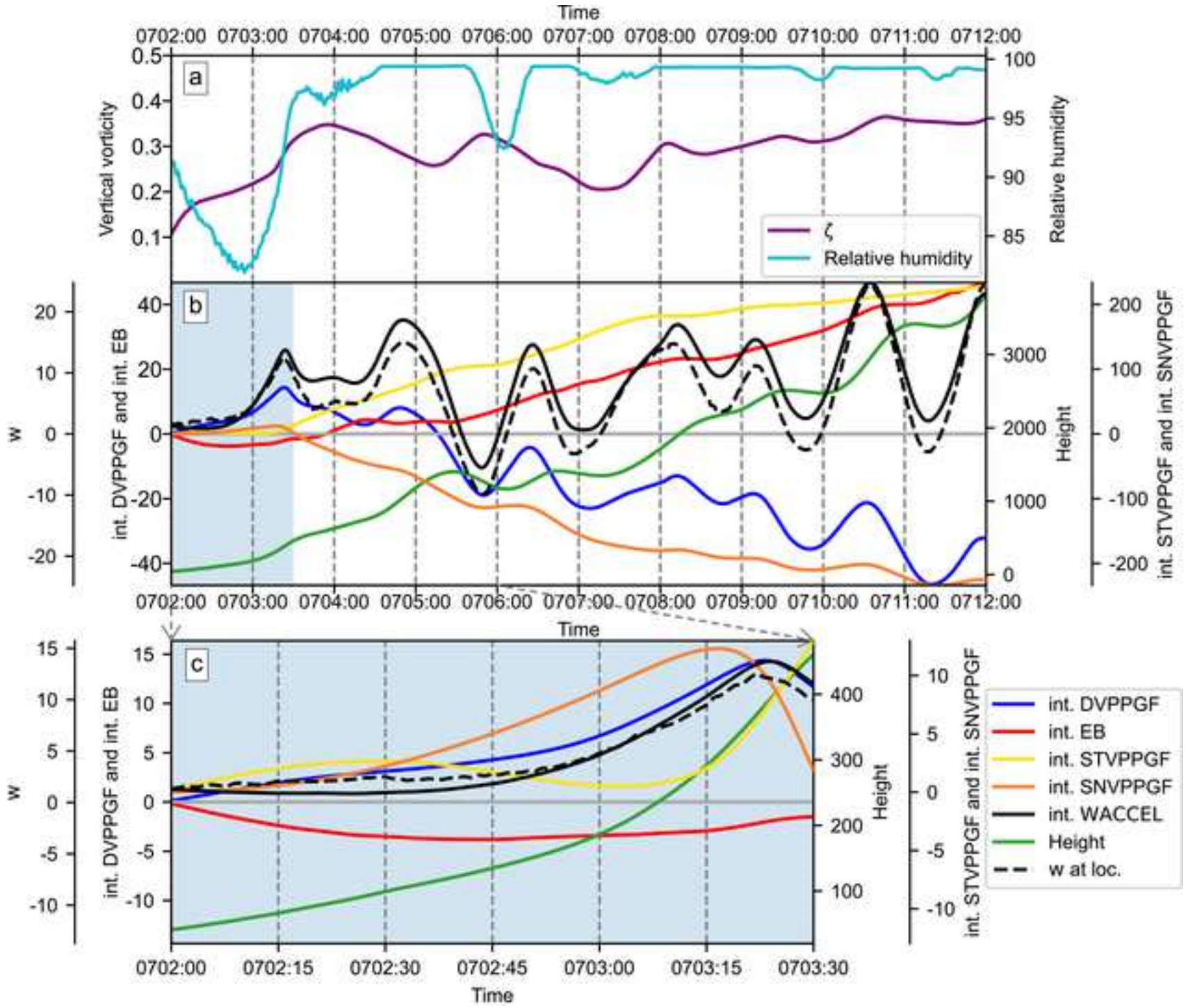

Fig.18

Click here to access/download;Rendered Figure;240_waccel_withvor_and_rh_0703.png

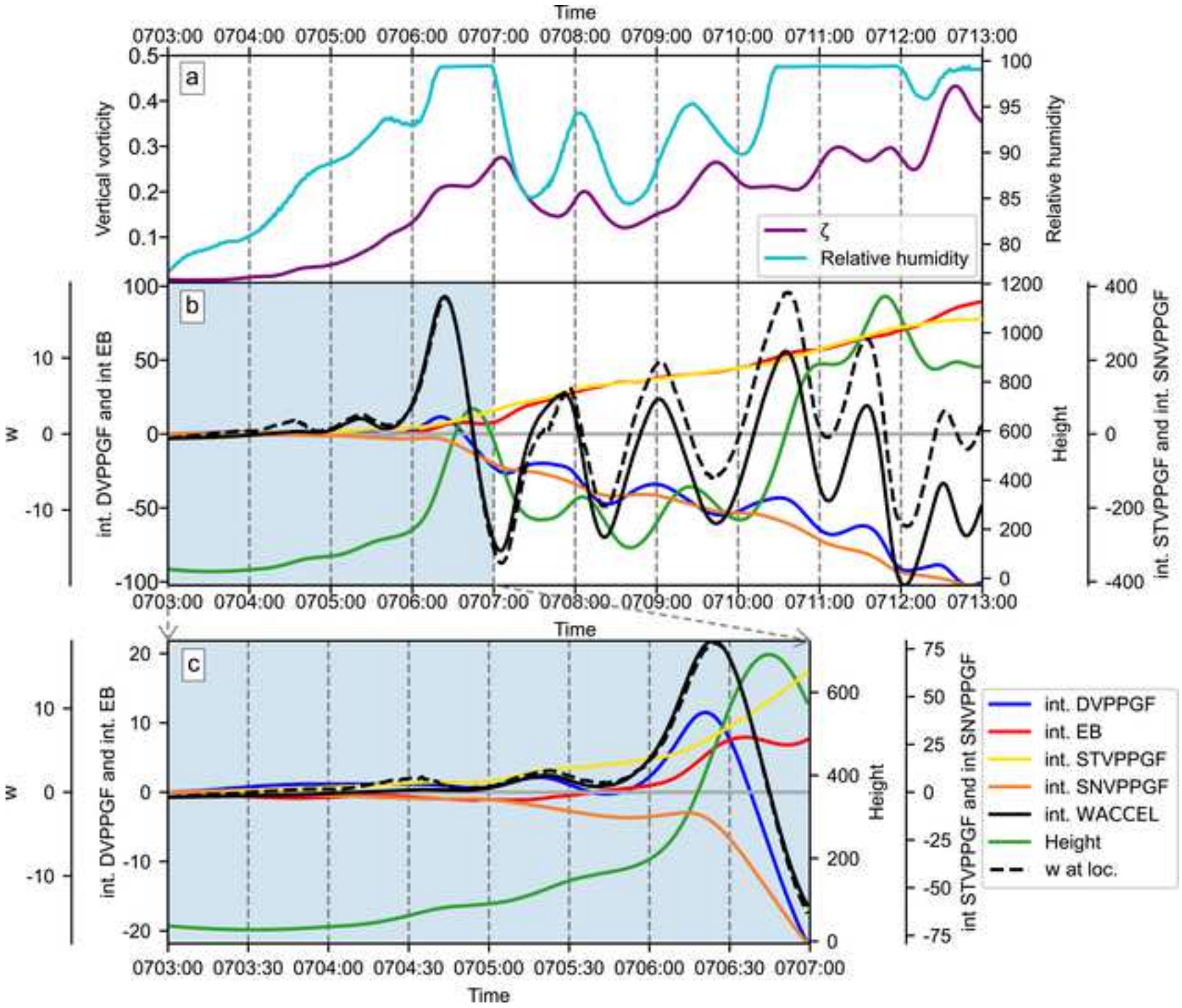

Fig.19

Click here to access/download;Rendered Figure;waccel_withvor_and_rh_average_0702.png

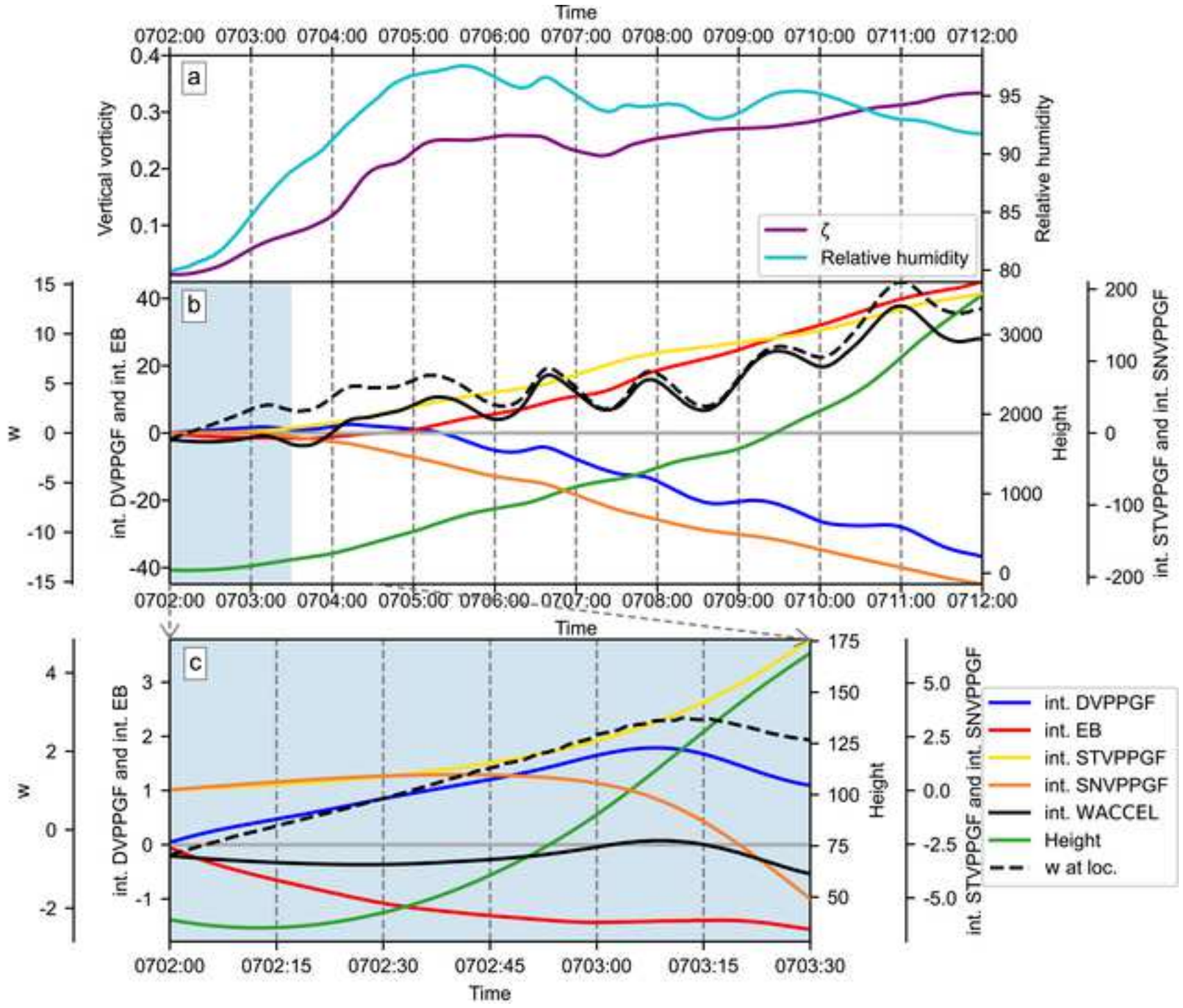

Fig.20

Click here to access/download;Rendered Figure;waccel_withvor_and_rh_average_0703.png

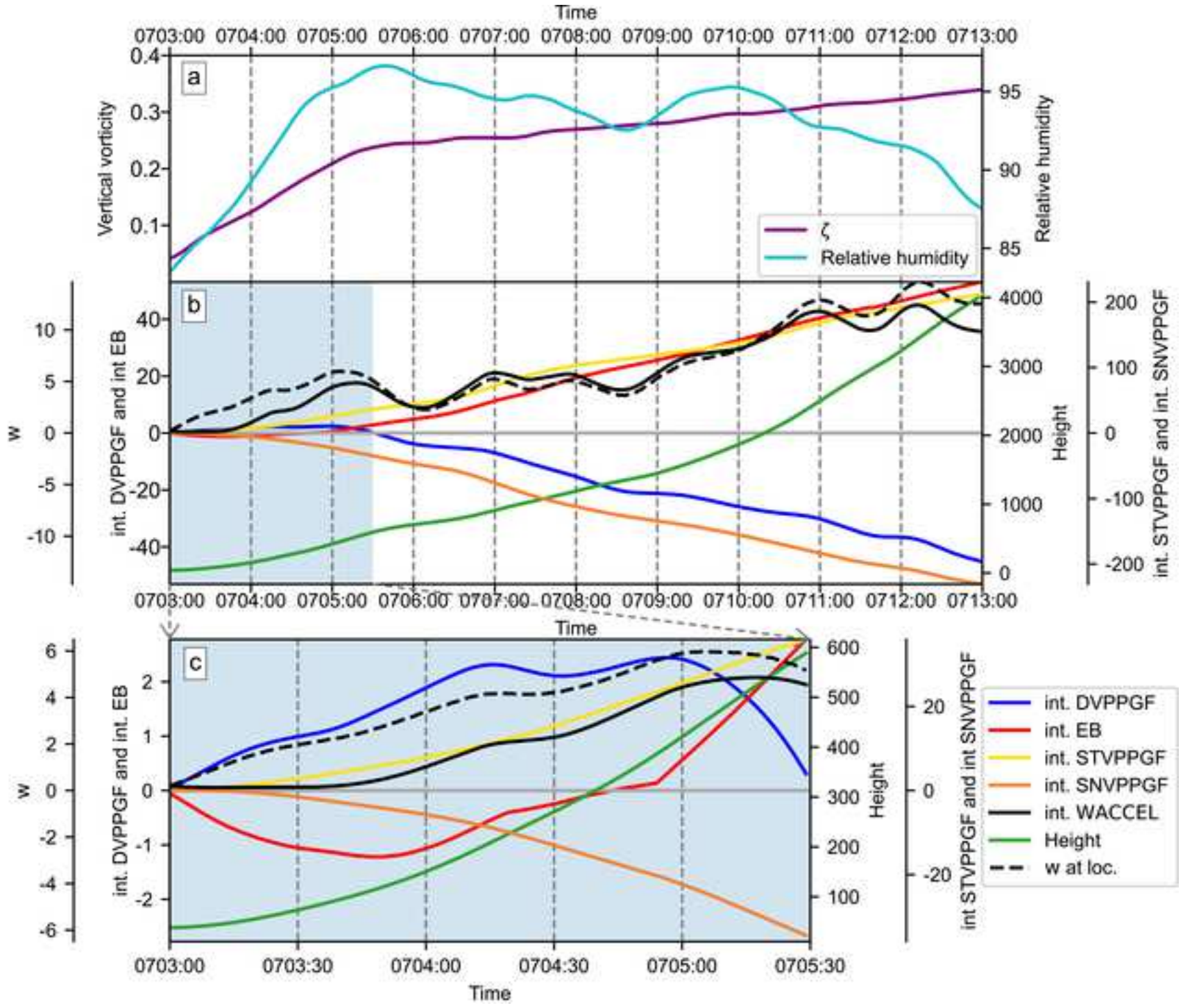

Fig.21